9-12-2016

The Bichromatic Force in Multi-Level Systems

Leland Aldridge
University of Connecticut - Storrs, leland.aldridge@uconn.edu

The Bichromatic Force in Multi-Level Systems

Leland Aldridge, Ph.D.

University of Connecticut, 2016

This dissertation describes calculations and simulations which extend the optical bichromatic force (BCF), which has previously been examined primarily in the context of two-level systems, to more complex polychromatic fields and to multi-level systems. Through detailed examination of various simple multilevel systems, I develop prescriptions for the application of the BCF to general multilevel systems. I apply these prescriptions to simulations of the molecular systems CaF and SrOH and provide BCF parameters for each that will guide future experiments. The design of an experiment to measure BCF deflection of a molecular beam of CaF is discussed. I close with discussion of prospects for extending this work to a molecular decelerator which can be used as the first stage of a molecular trap.

The Bichromatic Force in Multi-Level Systems

Leland Aldridge

B.S., University of Rochester, 2006

M.S., University of Connecticut, 2010

A Dissertation

Submitted in Partial Fullfilment of the

Requirements for the Degree of

Doctor of Philosophy

at the

University of Connecticut

2016

APPROVAL PAGE

Doctor of Philosophy Dissertation

The Bichromatic Force in Multi-Level Systems

Presented by

Leland Aldridge, B.S., M.S.

Major Advisor

Edward E. Eyler

Associate Advisor

Phillip Gould

Associate Advisor

Susanne Yelin

University of Connecticut

2016

To my family

ACKNOWLEDGEMENTS

Over the nine years that I have been at UConn, many people have contributed to getting me to this point. It truly does take a village to raise a PhD, and in that spirit I would like to thank:

The University of Connecticut and the National Science Foundation, for providing funding that made this work possible.

My family, and especially my parents, who got me started and who have been a constant source of support.

All of my friends and colleagues amongst the graduate students at UConn, including Alex Baldenko, Jennifer Carini, Ryan Carollo, Niraj Ghimire, Doug Goodman, Jon Kwolek, Nick Lewkow, Vincent Tagliamonti, James Wells, and many, many others. Being part of a strong community of graduate students kept me sane and motivated, and my friends often served as sounding boards for ideas about my work.

The office staff of the physics department, including Dawn Rawlinson, Micki Bellamy, Alessandra Introvigne, Andrea Sylvester, Jeannette Jamieson, and especially Kim Giard. These women kept the departmental ship afloat and were always willing to help me navigate the sometimes rocky waters of University bureaucracy.

The technical staff of the physics deparment, including Carol Artacho Guerra, Tom Dodge, Mike Rapposch, Michael Rozman, Heather Osborne, Alan Chasse and Dave Perry. Heather Osborne, as Manager of Laboratory Services for most of my time at UConn, gave me invaluable guidance on teaching and managing a classroom. Alan Chasse, the department's machinist, fabricated many elements of our apparatus, without which we would not have gotten very far.

The faculty of the physics department, including all those I took classes from to both expand and refine my knowledge of physics, and Phil Gould and Susanne Yelin for serving as my associate advisors and giving careful attention to this dissertation before its submission.

My predecessors and colleagues on the BCF project, Drew Chieda, Scott Galica and Donal Sheets. Drew laid much of the groundwork from which I continued, and Scott has very deftly picked up the experimental slack from my pivot to a computational focus. Donal was with us briefly but provided vital assistance with development of the experimental apparatus.

Finally and most significantly, my advisor Ed Eyler. Ed has been my advisor since my arrival at UConn, and has never turned away from me, despite crises of confidence and multiple changes in direction on my part, and significant medical issues on his. Through all of this, he has remained committed to advising and mentoring me to get me to where I am as a physicist today. I could not have made it through without him.

TABLE OF CONTENTS

Chapter 1

Introduction

The slowing and cooling of atoms using laser fields has grown to a mature and robust field since the first proposals over forty years ago [1–3] to use the radiative force, which is described in Sec. 1.1, to slow and cool. The magneto-optical trap (MOT) [4], which combines the radiative force with a magnetic field to create a spatially localized trap, has become a workhorse tool for cooling and trapping atoms for further interrogation and study. More recently, considerable attention has turned to applying these same methods to molecules.

In an atomic system, generally only the electronic degrees of freedom are relevant. Especially in alkali atoms with only one valence electron, this leads to a relatively simple energy level structure. In even the simplest molecular systems, vibration and rotation of the multiple nuclei add additional energy structure [5], which will complicate any attempts to interact with the molecule using laser fields.

Molecules such as YO [6], CaF [7,8] and SrF [9,10] have been successfully slowed and cooled using the radiative force despite these complications. The additional molecular structure has meant that these successful applications have

required multiple separate lasers for use during the slowing process. Molecular MOT techniques are being developed, with transverse cooling of a molecular beam of YO accomplished with a 2D molecular MOT [11]. With the use of pre-cooled buffer gas sources [12], the achieved radiative slowing has been sufficient to load a full 3D molecular MOT, which has been realized for the first time very recently using SrF [13,14].

Given the success of applying the radiative force to small molecules, other optical techniques that in atoms allow for stronger-than-radiative forces may provide improvements in molecular systems as well. This dissertation will emphasize coherent optical forces, which use multiple or time-dependent frequencies to create force via coherent optical cycling, rather than relying on decoherence-causing spontaneous decays.

1.1 The Radiative Force

The radiative force is most cleanly explained with reference to a two-level system, consisting of a ground state and an excited state that are coupled by an optical field. If a resonant monochromatic plane wave is incident on the atom, the atom can absorb energy from the light field and transition to its excited state. This transfer of energy is concomitant with a transfer of momentum such that the atom feels an impulse $\Delta\vec{p} = \hbar k$, where $\vec{k}$ is the wavevector of the light, pointing in the direction of propagation and having magnitude $2\pi/\lambda$ for light of wavelength λ.

At this point, the excited two-level system cannot absorb any further energy from the light field.

There are two ways for the system to return to the ground state: either through spontaneous or stimulated emission. Spontaneous emission is random in time and phase, totally dephasing the system when it occurs. Stimulated emission is coherent with the surrounding light field. In the case of a monochromatic plane wave light field, any stimulated emission would produce a photon traveling in the same direction as the photon that was absorbed, leading to zero net impulse over one cycle. Spontaneous emission, being random and symmetric, will also average to produce zero net impulse over many events, but this still leaves the impulses due to the absorptions (Fig. 1.1).

Thus for the radiative force, the photon scattering rate for spontaneous emission γ_{sc} is directly related to the net force on the system. Every photon that is scattered through spontaneous emission is necessarily paired with an absorption event that provides an impulse along the wavevector of the light field. The magnitude of the force is thus

$$F = \hbar k \gamma_{\mathrm{sc}} \tag{1.1}$$

Spontaneous emission occurs at a fixed probability per unit time whenever the system is in its excited state. This probability is determined by the coupling of the two states through the vacuum, and results in a natural decay rate Γ. On

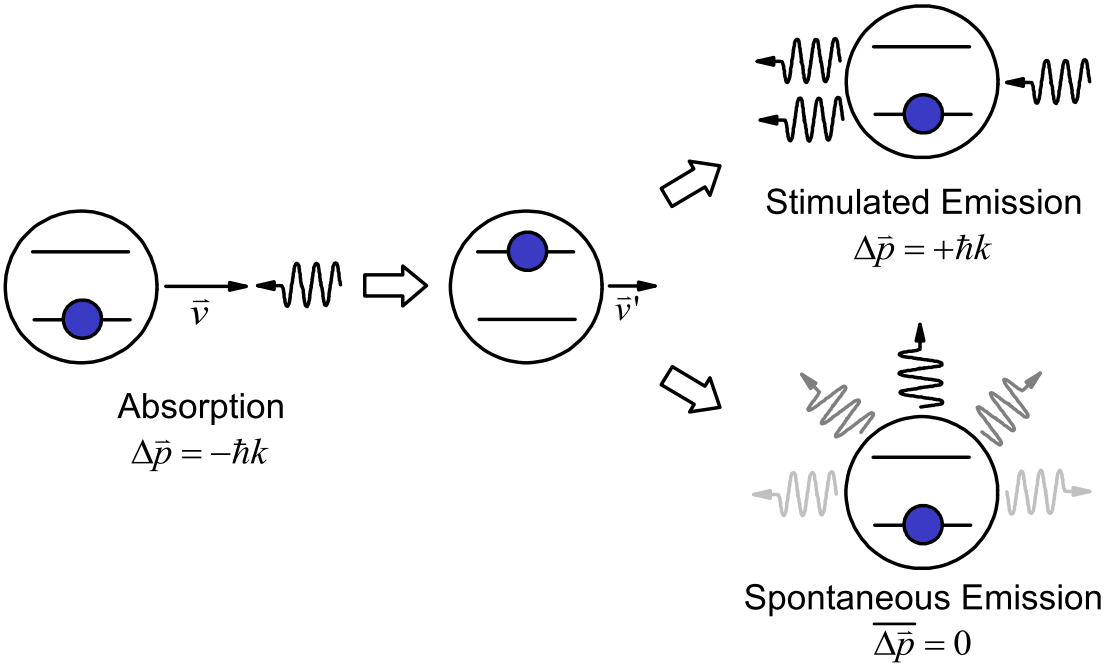

Fig. 1.1: The radiative force operates by transferring momentum from a directed light field to a target through absorption. This excites the target, which must then relax back to the ground state before it can absorb again. If this occurs through stimulated emission that is coherent with the driving field, there is an opposite impulse as from the absorption and no net impulse. If the relaxation is through spontaneous emission, the impulse direction is random and averages to zero over many events, leaving a net impulse from absorption. This figure is based on Fig. 1.1 of Ref. [15].

the other hand, absorption and stimulated emission both occur with a probability per unit time depending on the light field irradiance, and these probabilities are identical in a two-level system. This leads, absent spontaneous decay, to sinusoidal Rabi oscillation of the quantum state of the system. The frequency of this oscillation increases for higher irradiance. Combining these two effects, the average excited-state fraction saturates at 1/2 for constant high irradiance.

The maximum photon scattering rate for the radiative force is therefore half the excited-state spontaneous decay rate, $\gamma_{sc} = \Gamma/2$, and the ideal radiative force in a two-level system is

$$F_{rad} = \frac{\hbar k \Gamma}{2}. \tag{1.2}$$

Increasing the irradiance of the driving field causes the force to approach this limiting value, but never to exceed it.

In general, the photon scattering rate for a two-level system moving at velocity $\vec{v}$ in a monochromatic field detuned from the two-level resonance by δ is [16]

$$\gamma_{\mathrm{sc}} = \frac{s\Gamma}{2(1 + s + (2(\delta - \vec{k} \cdot \vec{v})/\Gamma)^2)}, \tag{1.3}$$

where s is the dimensionless saturation parameter

$$s = I \frac{3\lambda^3}{\pi h c \Gamma} \tag{1.4}$$

for light of irradiance I.

The photon scattering rate can be seen from Eq. 1.3 to be approximately Lorentzian in $\vec{k} \cdot \vec{v}$, converging to a Lorentzian with width $\sqrt{s}\,\Gamma$ when $s \gg 1$. When the velocity is aligned with the wavevector of the light, the FWHM of the force as a function of velocity is therefore $\sqrt{s}\,\Gamma/k$. As they follow the Lorentzian, the photon scattering rate and the radiative force begin falling off immediately if the system decelerates and its velocity moves away from δ/k.

Due to the limited magnitude of the force and its relatively narrow Lorentzian velocity profile, to achieve significant slowing using the radiative force it is necessary to adjust δ as v changes, to keep $\delta - \vec{k} \cdot \vec{v}$ near zero. This has been accomplished by various methods:

1. Sweeping or "chirping" the frequency of the driving laser, such that the velocity for which $\delta - \vec{k} \cdot \vec{v}$ is time-dependent [17–19]. For a constant force, a linear chirp will keep the Doppler-shifted light resonant in the target frame as the atom slows. This method is best suited for pulsed sources, as only atoms with a particular velocity at a particular time will follow the chirp.

2. Broadening the laser spectrum, such as by use of electro-optic modulators (EOMs), so that there is spectral density at the resonant $\vec{k}$ for all velocities during the slowing [8]. This method requires a large amount of power, as it must be distributed across a broad range of frequencies.

2. Creating a static electric field along the length of the slowing region, with a spatially-dependent magnitude. The dc Stark shift of the atomic energy levels,

dependent on the electric field magnitude, can be engineered so that it offsets the Doppler shift of the slowing atoms as they pass through the slowing region [20].

3. Creating a static magnetic field along the length of the slowing region, with a spatially-dependent magnitude. This is similar to the Stark decelerator, but uses the magnetic Zeeman shift to keep the atoms on resonance with the laser field [21].

The key features of the radiative force, in comparison to coherent forces, are a reliance on photon scattering, which occurs at a rate that is not tunable, and that the force is maximized at a single exact velocity. Radiative force decelerators therefore require extended slowing regions and finely-tuned additional features to account for changing Doppler shifts.

1.2 Adiabatic Rapid Passage Force

One method for exceeding the radiative force limit with a purely optical force is by application of adiabatic rapid passage (ARP) [22], which uses a frequency-chirped pulse to efficiently and adiabatically invert a two-level system from the ground to the excited state or vice-versa. The intensity and detuning from resonance both affect the dressing of the levels by the field, and by engineering a particular time-dependence of each, the probability of inversion can be maximized.

By timing two counter-propagating pulse trains, a two-level target system can be set up so that it is struck by an exciting ARP pulse from one direction,

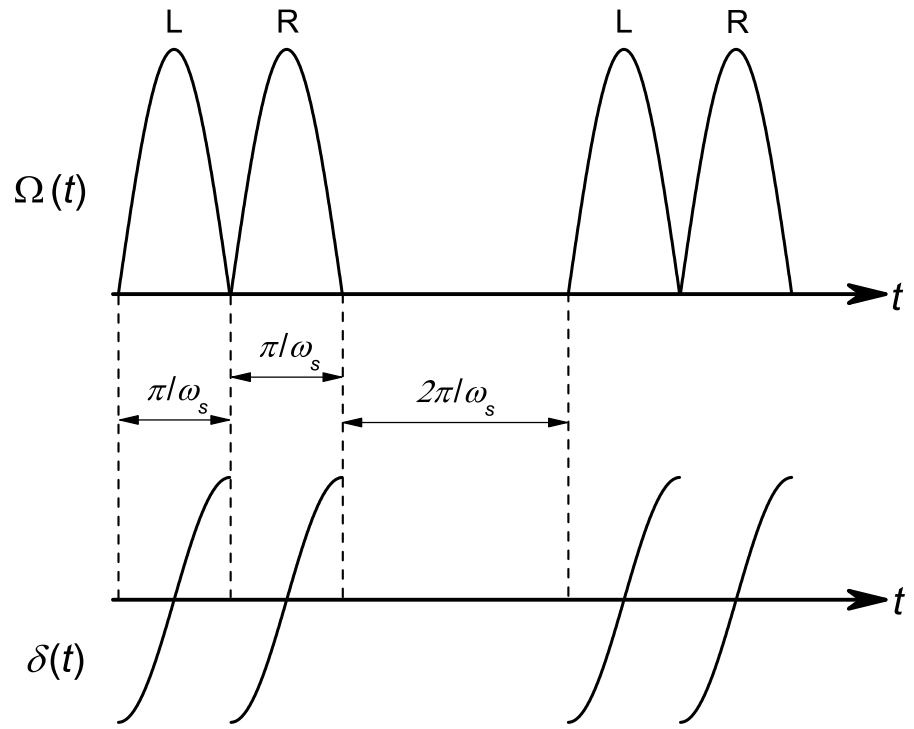

Fig. 1.2: The chirped pulse sequence to create the ARP force, for a pulse repetition frequency ω_s. L and R indicate the propagation direction, left or right, of the pulses. This figure is based on Fig. 1 of Ref. [24].

followed immediately by a de-exciting ARP pulse from the opposite direction (Fig. 1.2). This pulse pair leaves the system in the ground state, having experienced two photon impulses in the same direction with very little time during which to possibly spontaneously decay, assuming sufficiently short pulses. The force created is dependent on the repetition rate of these pulse pairs, rather than on the photon scattering rate.

For a chirp amplitude δ_0, peak Rabi frequency Ω_0, pulse repetition frequency ω_s, and excited state decay rate Γ, the optimal conditions for the ARP force can

be summarized as [23]

$$\delta_0 \sim \Omega_0 \sim \omega_s \gg \Gamma, \tag{1.5}$$

and the force, due to a photon-recoil-induced impulse of $\hbar k$ during each pulse, is expected to have an ideal magnitude [23]

$$F_{ARP} \sim \frac{\hbar k \omega_s}{2\pi} \gg F_{rad}. \tag{1.6}$$

Experimental tests of the ARP force using metastable helium (He^*) have produced forces with magnitude more than 20% that of the ideal force, or about seven times larger than the ideal radiative force [24].

The velocity capture range of the ARP force is calculated to be on a scale of $\sim \delta/k$, which can be much larger than the Γ/k of the radiative force [23].

1.3 Bichromatic Force

The bichromatic force (BCF) technique is an outgrowth of attempts to rectify the dipole force, which arises from intensity gradients in a standing wave and is not inherently limited in magnitude [16]. However, since the dipole force is proportional to the intensity gradient, its sign reverses on the scale of an optical wavelength, and averages to zero over macroscopic distances.

By adding a second standing wave that modulates the effective detuning of the first standing wave, the total force can be caused to be positive over an optical

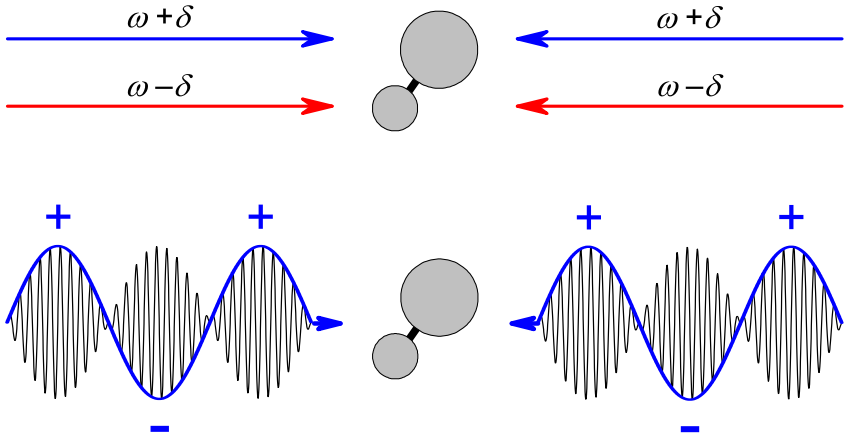

Fig. 1.3: The BCF optical field is created by the superposition of four monochromatic fields, consisting of a pair of counterpropagating two-color fields of frequencies $\omega \pm \delta$ (top). Each two-color field creates an intensity-modulated beat note train (bottom). The sinusoidal field envelope is shown in blue and is further discussed in Sec. 2.4.

wavelength [25–27]. This method generally produces forces a few times stronger than the radiative force, but when each standing wave is detuned above and below resonance by the same amount, and the intensity is properly tuned, the situation is far more favorable. In this configuration, forces many times the radiative force are achieved in what was dubbed the bichromatic force [28]. These symmetrically detuned standing waves can be alternatively interpreted as counter-propagating trains of on-resonant beats (Fig. 1.3).

These beat note trains serve the same coherent excitation-deexcitation role as in the ARP force, but without the need for synchronizing a frequency chirp with each pulse. The two laser colors that produce each train give the technique its name.

Extensions of the BCF to fields of more colors and to systems with multiple levels, especially molecular systems, will be the focus of this dissertation.

Chapter 2

Theory of the Bichromatic Force

To form the counterpropagating beat note trains of the BCF optical field, four monochromatic optical fields are overlapped with all combinations of frequency $\omega \pm \delta$ and propagation direction $\pm\hat{z}$ (Fig. 1.3). Additionally, a phase offset $\pm\chi/2$ is included, advancing the $+z$ fields and delaying the $-z$ fields, to allow for adjustable RF phase between the beat-note trains at the target location, $z = 0$. Assuming that all four waves have identical amplitudes and linear polarizations, the electric field magnitudes can be written as:

$$\begin{aligned} E_{R,+} &= E_0 \cos\left[(\omega+\delta)(z/c-t)+\chi/2\right], \\ E_{R,-} &= E_0 \cos\left[(\omega-\delta)(z/c-t)-\chi/2\right], \\ E_{L,+} &= E_0 \cos\left[(\omega+\delta)(-z/c-t)-\chi/2\right], \\ E_{L,-} &= E_0 \cos\left[(\omega-\delta)(-z/c-t)+\chi/2\right]. \end{aligned} \tag{2.1}$$

If these are interpreted as superpositions of the pairs of waves with the same detuning, the overall field can be viewed as two standing waves. Alternatively, the

fields can be interpreted by pairing beams with the same propagation direction, resulting in the counterpropagating beat note trains mentioned above,

$$E_R = E_{R,+} + E_{R,-} = 2E_0 \cos\left[\omega(z/c - t)\right] \cos\left[\delta(z/c - t) + \chi/2\right],$$
$$E_L = E_{L,+} + E_{L,-} = 2E_0 \cos\left[\omega(-z/c - t)\right] \cos\left[\delta(-z/c - t) - \chi/2\right]. \quad (2.2)$$

2.1 π-Pulse Model

The simplest model of the bichromatic force is constructed by considering the action of these beat note trains on a two-level system, assuming for the moment that each beat note acts separately. In this model, to ensure excitation from one train and stimulated emission from the other, each beat note should be tuned in duration and peak intensity to be a π-pulse that perfectly inverts the system, either from ground to the excited state or vice versa. This is the π-pulse model of BCF [28,29].

The beats within each of the two pulse trains have a repetition rate of π/δ, and each pulse-driven population inversion causes a transfer of one photon worth of momentum, $\hbar k$. From this, the idealized force in the π-pulse model is easily expressed as the rate of momentum transfer,

$$F^{\pi}_{BCF} = \frac{2\hbar k}{\pi/\delta} = \frac{2\hbar k\delta}{\pi}. \quad (2.3)$$

One immediate deficiency of this model is that the beats can not actually be treated separately. In the bichromatic field, the intensity variation is sinusoidal, with no temporal separation between one beat and the next. The counterpropagating beats will necessarily overlap each other in time, and for a full description of the force their simultaneous action on the system must be taken into account.

Another deficiency of the model is the presumption of perfect phasing between excitation and decay cycles. First, recall that each beat is half an oscillation of the sinusoidal intensity envelope, so that beats have a spacing of 180° of phase. If at the target location, there were no relative phase (0°), there would be no preference for which train to absorb from or emit into, as both beats would be totally overlapped, giving zero net force. If the relative phase were 90°, there would be again total symmetry with time inversion, equivalent to a time offset, and when averaged over long periods there would still be zero net force. Given the smooth sinusoidal beating, it may be conjectured that the optimum phasing would be directly between these two conditions, at 45°.

Examining the timing in a little more detail, each time the system spontaneously decays, it completely dephases and the BCF cycling resets. If the beats are taken to be isolated pulses localized at their peaks, and the counterpropagating trains are phased at 45°, 1/4 of the uniformly randomly-timed decays will start the target cycling by first "seeing" and being excited by the pulse meant to de-excite, while 3/4 will enter the "correct" cycle. This leads to an overall

reduction of the average expected force by a factor of two:

$$F_{BCF} = F^{\pi}_{BCF}/2 = \frac{\hbar k \delta}{\pi}. \tag{2.4}$$

These heuristic arguments lead to useful results, correctly predicting the optimal phase and force magnitude as will be seen, but can only be carried so far. A more direct treatment of the reaction of this system to the bichromatic optical field is needed for a full description.

The total electric field is the superposition of the fields of the two beat note trains. In the approximation that $z \ll c/\delta$, meaning that the sample size of the system is restricted to a region near $z = 0$ that is small compared to the length of a single beat, the full electric field magnitude is given by

$$E(z,t) = 4E_0 \left(\cos(\omega t)\cos(kz)\cos(\delta t)\cos(\chi/2) + \sin(\omega t)\sin(kz)\sin(\delta t)\sin(\chi/2)\right), \tag{2.5}$$

where $k = \omega/c$. In a more general case for which the polarizations are still identical but are not restricted to be linear, the full electric field is given by

$$\vec{E}(z,t) = 4E_0 \mathrm{Re}\left[\hat{\epsilon} e^{-i\omega t}\left(\cos(kz)\cos(\delta t)\cos(\chi/2) + i\sin(kz)\sin(\delta t)\sin(\chi/2)\right)\right], \tag{2.6}$$

where $\hat{\epsilon}$ is a complex unit polarization vector.

A system such as an atom or molecule, after taking all of its internal struc-

ture into account, can be described in isolation by an unperturbed Hamiltonian H_0 in terms of the energy eigenstates $|i\rangle$ and eigenenergies $\hbar\omega_i$ of the system as

$$\frac{H_0}{\hbar} = \sum_i \omega_i |i\rangle \langle i| . \tag{2.7}$$

In the presence of an external electromagnetic field, such as the BCF optical field, the states of the system are coupled. For optical radiation, the dominant coupling mechanism is normally electric dipole coupling. The electric dipole coupling strength between two states $|i\rangle$ and $|j\rangle$ can be characterized by a complex Rabi frequency defined by [30]

$$\Omega_{ij}^R(z,t) \equiv \frac{\langle i| \hat{d} \cdot \vec{E}(z,t) |j\rangle}{\hbar}, \tag{2.8}$$

where $\hat{d}$ is the electric dipole operator. Each of these Rabi frequencies Ω_{ij}^R can be separated into two terms with amplitudes Ω_{ij} and Ω_{ij}^* that describe co-rotating and counter-rotating components in the rotating wave approximation:

$$\Omega_{ij}^R(z,t) = \frac{1}{2}(\Omega_{ij} e^{-i\omega t} + \Omega_{ij}^* e^{i\omega t}). \tag{2.9}$$

It will often be convenient in this disseration to refer to the "Rabi frequency

amplitude" of a transition, which is defined here as

$$\Omega_{ij}^{0} \equiv \frac{E_0}{\hbar} \langle i | \, \hat{d} \cdot \hat{\epsilon} \, | j \rangle \, . \tag{2.10}$$

Combining the above, the co-rotating Rabi frequency on a transition under bichromatic illumination is

$$\Omega_{ij} = 4\Omega_{ij}^{0} \left(\cos(kz) \cos(\delta t) \cos(\chi/2) + i \sin(kz) \sin(\delta t) \sin(\chi/2) \right) . \tag{2.11}$$

Adding the electric dipole coupling to the unperturbed Hamiltonian H_0 gives the "full" Hamiltonian,

$$\frac{H}{\hbar} = \frac{H_0}{\hbar} + \sum_{i,j} \left(\Omega_{ij}^{R} \, |i\rangle \langle j| + \text{c.c} \right) , \tag{2.12}$$

which is sufficient to capture the behavior which generates the bichromatic force.

2.2 Floquet Analysis

One way of describing the behavior of a system under BCF illumination is by use of a Floquet Hamiltonian, which replaces the time-dependent oscillations of the Hamiltonian in Eq. 2.12 with an expanded state space that includes the numbers of "effective photons" with frequencies 2δ and $2kv$ [31].

In the limit of small velocities, no $2kv$ effective photons are exchanged, and

the system can be described fully by the number of 2δ effective photons that have been exchanged, which corresponds to the relative net number of red and blue photons absorbed. In the basis of this number of effective photons exchanged, the Hamiltonian is

$$\frac{H_{Floq}}{\hbar} = \begin{pmatrix} \ddots & & & & & \\ & 2\delta & \Omega_+/2 & 0 & 0 & 0 \\ & \Omega_+/2 & \delta & \Omega_-/2 & 0 & 0 \\ & 0 & \Omega_-/2 & 0 & \Omega_+/2 & 0 \\ & 0 & 0 & \Omega_+/2 & -\delta & \Omega_-/2 \\ & 0 & 0 & 0 & \Omega_-/2 & -2\delta \\ & & & & & \ddots \end{pmatrix}, \tag{2.13}$$

where $\Omega_\pm = 2\Omega_0 \cos(kz \pm \chi/2)$, the spatial components of the Rabi frequencies due to the counterpropagating beat trains. The eigenenergy of each of the infinite ladder of states is position dependent. At $z = 0$ the energies are equal simply to $\hbar\delta n$, where n is the number of effective photons exhanged. At low Ω_0, the levels do not interact strongly, but at higher Ω_0, there are both real and avoided crossings, of which diabatic crossings represent an exchange of effective photons between the system and the light field (Fig. 2.1).

At a Rabi frequency amplitude of $\Omega_0 = \sqrt{3/2}\,\delta$, the energy gap between adjacent levels is minimized, and the system can most easily follow a trajectory

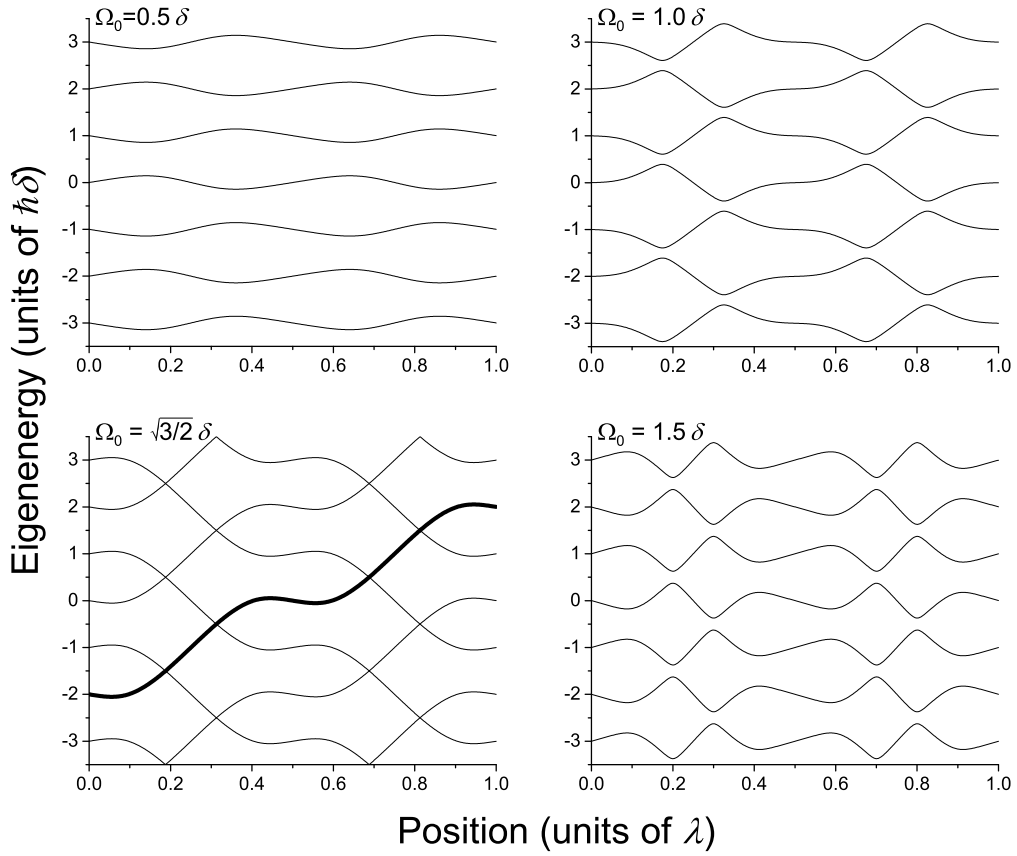

Fig. 2.1: Position-dependent eigenenergies of Floquet states in a BCF optical field with $\chi = 45°$. At a Rabi frequency amplitude of $\Omega_0 = \sqrt{3/2}\,\delta$, the gaps between energy levels are minimized and the system can most easily follow a trajectory of increasing energy in the field (bold line).

of increasing energy in the light field. This corresponds to a repeated removal of kinetic energy from the atom, slowing it. Over the scale of a single optical wavelength, the change in energy as the system follows the optimal trajectory is $4\hbar\delta$. This implies a force of

$$F_{BCF}^{Floq} = \Delta E/\Delta x = \frac{4\hbar\delta}{\lambda} = \frac{2\hbar k\delta}{\pi} \tag{2.14}$$

which is consistent with the force predicted by the pi-pulse model. It can be seen in Fig. 2.1 that accelerating trajectories exist as well as decelerating trajectories. As odd values of n correspond to the system being in the excited state, the accelerating trajectories spend three times as long in the excited state as the decelerating ones, and will therefore spontaneously decay (into decelerating trajectories) in one-third the time. Thus the system will spend 3/4 of its time on accelerating trajectories and 1/4 of its time on decelerating trajectories, leading to the same reduction in force by a factor of two as when spontaneous decay is considered in the pi-pulse model.

Unlike the pi-pulse model, this Floquet analysis can be used to predict the velocity range of the BCF. In the low-velocity approximation, where only effective photons at 2δ are considered, the force will be limited by diabatic level transfers at the more strongly avoided crossings. This will shift the system from a decelerating to an accelerating trajectory. The probability for this can be calculated for an

isolated crossing by the Landau-Zener (LZ) formula [32,33],

$$P_{LZ} = \exp\left(-\frac{\pi U^2}{\hbar v \nabla E}\right) \tag{2.15}$$

where $2U$ is the energy splitting at the avoided crossing, v is the atom velocity, and ∇E is the gradient of the energy on either side of the crossing. At higher speeds, the chance of crossing diabatically increases. In Ref. [31], this has been used to estimate the velocity range for the BCF as $\sim \delta/2k$. Additionally, beyond this velocity, it can no longer be said that $\delta \gg kv$ and the low-velocity limit no longer applies.

2.3 Numerical Solution of Density Matrix Trajectories

Unfortunately, when extending the BCF to fields of more colors or to systems of more states, the analytic Floquet treatment becomes prohibitive. Thus the approach preferred here will be to directly numerically integrate the equations of motion of the density matrix.

The state of the system is described by the $N \times N$ density matrix ρ, where N is the total number of eigenstates of the system. The quantum Liouville equation with dispersion [34] gives the time rate of change of ρ,

$$i\hbar\dot{\rho} = [H, \rho] + i\hbar\frac{\partial \rho}{\partial t}. \tag{2.16}$$

The partial derivative term is necessary to describe spontaneous decay with a classical EM field. This equation produces a system of coupled differential equations for each term of the density matrix, which can be solved to describe its evolution through time given an initial state.

Ehrenfest's theorem gives the force on a system as [35]

$$\vec{F} = -\langle \vec{\nabla} H \rangle = -\mathrm{Tr}\left(\rho \vec{\nabla} H\right). \tag{2.17}$$

This describes the toolbox for evaluating the bichromatic force on an atomic or molecular system. When the energy structure and transition strengths of the system are known, the Liouville equation can be used to calculate the time-evolution of the system under BCF illumination. The time-dependent density matrix can then be used to calculate the force on the system by use of Ehrenfest's theorem.

I will primarily examine systems with a lower-state manifold of M_g levels and an upper-state manifold of M_e levels, for which each of the lower-state levels may be coupled to any of the upper-state levels by the BCF optical fields, depending on selection rules and line strengths. A single distant dark state is at times included as well, where "distant" in this setting means that couplings of this state to any of the others by the primary BCF optical fields are negligible. This general class of systems is illustrated in Fig. 2.2. These systems will be referred to as $M_g + M_e$,

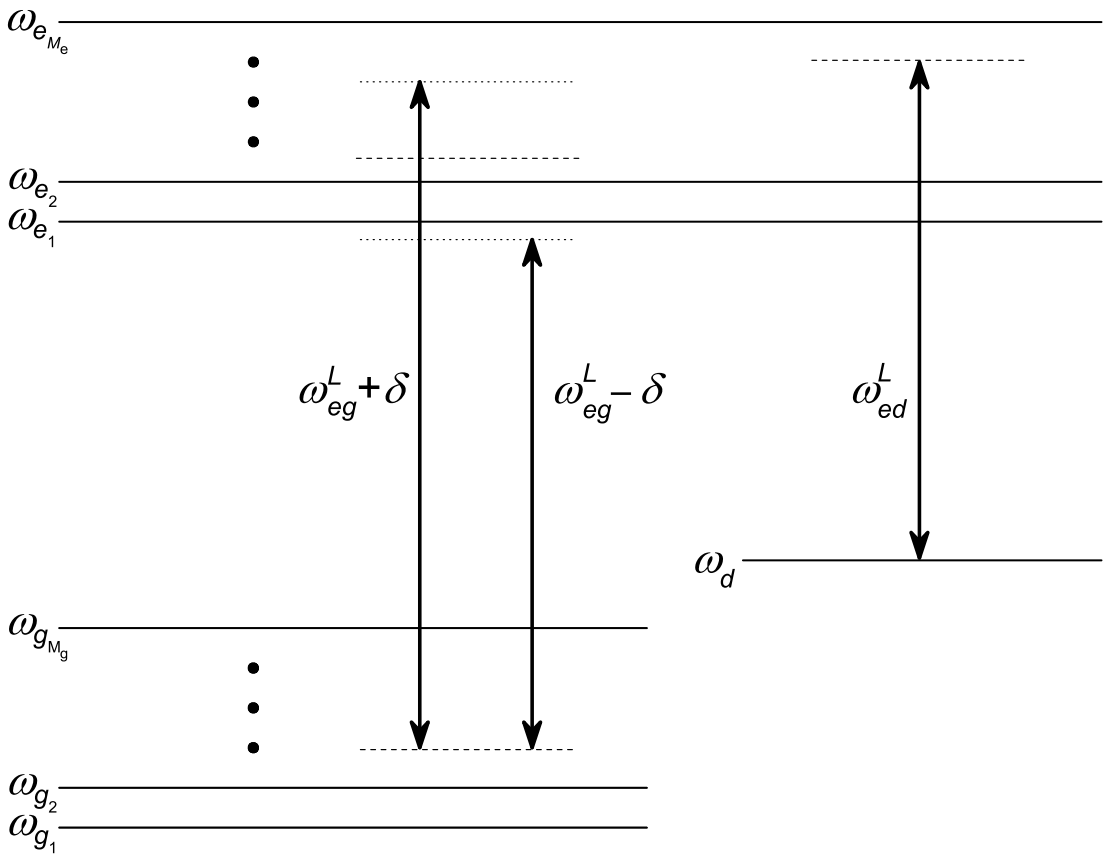

Fig. 2.2: A schematic diagram of the general multilevel system simulated here. Ground (g) and excited (e) levels with multiplicities M_g and M_e are coupled by a bichromatic laser field with frequencies $\omega_{eg}^L \pm \delta$, and excited levels are coupled to a distant (d) level by a laser field with frequency ω_{ed}^L. There is no direct coupling or decay between the d and g states. Levels are labeled by their characteristic frequencies.

with (or without) a distant dark state. Sums over a ground state index (p, q, r) should be understood to run from 1 to M_g, and sums over an excited state index (i, j, k) from 1 to M_e.

The time-dependence of the density matrix is simplified by transforming into a rotating frame and applying the rotating wave approximation. The rotating

frame is defined by the rotating coherence terms [36,37]

$$\begin{aligned}
\widetilde{\rho}_{e_i g_p} &\equiv \rho_{e_i g_p}\, e^{i\omega_{eg}^L t} \\
\widetilde{\rho}_{e_i d} &\equiv \rho_{e_i d}\, e^{i\omega_{ed}^L t} \\
\widetilde{\rho}_{d g_p} &\equiv \rho_{d g_p}\, e^{i(\omega_{eg}^L - \omega_{ed}^L)t},
\end{aligned} \tag{2.18}$$

where ω_{eg}^L is the carrier frequency of the laser field coupling the excited and ground states and ω_{ed}^L is the carrier frequency of the laser field coupling the excited and distant states. This transformation leaves some terms with a difference in optical frequencies and some terms with a sum of optical frequencies. The rotating wave approximation is applied by neglecting those terms with a sum of optical frequencies, as they change too quickly to have a noticeable effect on the density matrix.

Each excited state population $\rho_{e_i e_i}$ will decay with a total spontaneous decay rate Γ_i, and this decay will populate the ground or distant states with specific channel decay rates γ_{ip}, which sum to the total spontaneous decay rate. The off-diagonal terms of the density matrix will also decay at a rate of half the total decay rate of the two states [34]. Including these spontaneous decay terms, the full set of equations of motion of the density matrix of an $M_g + M_e$ system with a distant state $|d\rangle$ is given by,

$$
\begin{aligned}
\dot{\rho}_{e_i e_i} &= -\sum_q \mathrm{Im}[\Omega^*_{e_i g_q}\,\widetilde{\rho}_{e_i g_q}] - \mathrm{Im}[\Omega^*_{e_i d}\,\widetilde{\rho}_{e_i d}] - \Gamma_i \rho_{e_i e_i} \\
\dot{\rho}_{e_i e_j} &= \frac{i}{2}\left[2(\omega_{e_j}-\omega_{e_i})\rho_{e_i e_j} + \sum_q \left(\Omega^*_{e_j g_q}\,\widetilde{\rho}_{e_i g_q} - \Omega_{e_i g_q}\,\widetilde{\rho}^*_{e_j g_q}\right) + \Omega^*_{e_j d}\,\widetilde{\rho}_{e_i d} - \Omega_{e_i d}\,\widetilde{\rho}^*_{e_j d}\right] \\
&- \frac{\Gamma_i+\Gamma_j}{2}\rho_{e_i e_j} \\
\dot{\widetilde{\rho}}_{e_i d} &= \frac{i}{2}\left[2(\omega^L_{ed}+\omega_d-\omega_{e_i})\widetilde{\rho}_{e_i d} + \Omega_{e_i d}(\rho_{e_i e_i}-\rho_{dd}) - \sum_q \Omega_{e_i g_q}\,\rho^*_{d g_q} + \sum_{k\neq i}\Omega_{e_k d}\,\rho_{e_i e_k}\right] \\
&- \frac{\Gamma_i}{2}\widetilde{\rho}_{e_i d} \\
\dot{\widetilde{\rho}}_{e_i g_p} &= \frac{i}{2}\left[2(\omega^L_{eg}+\omega_{g_p}-\omega_{e_i})\widetilde{\rho}_{e_i g_p} + \Omega_{e_i g_p}(\rho_{e_i e_i}-\rho_{g_p g_p}) - \sum_{q\neq p}\Omega_{e_i g_q}\,\rho_{g_q g_p}\right. \\
&+ \left.\sum_{k\neq i}\Omega_{e_k g_p}\,\rho_{e_i e_k} - \Omega_{e_i d}\,\rho_{d g_p}\right] - \frac{\Gamma_i}{2}\widetilde{\rho}_{e_i g_p} \\
\dot{\rho}_{dd} &= -\sum_k \dot{\rho}_{e_k e_k} - \sum_q \dot{\rho}_{g_q g_q} \\
\dot{\widetilde{\rho}}_{d g_p} &= \frac{i}{2}\left[2(\omega^L_{eg}+\omega_{g_p}-\omega^L_{ed}-\omega_d)\widetilde{\rho}_{d g_p} + \sum_k(\Omega_{e_k g_p}\,\widetilde{\rho}^*_{e_k d} - \Omega^*_{e_k d}\,\widetilde{\rho}_{e_k g_p})\right] \\
\dot{\rho}_{g_p g_p} &= \sum_k(\mathrm{Im}[\Omega^*_{e_k g_p}\,\widetilde{\rho}_{e_k g_p}] + \gamma_{kp}\,\rho_{e_k e_k}) \\
\dot{\rho}_{g_p g_r} &= \frac{i}{2}\left[2(\omega_{g_r}-\omega_{g_p})\rho_{g_p g_r} + \sum_k(\Omega_{e_k g_r}\widetilde{\rho}^*_{e_k g_p} - \Omega^*_{e_k g_p}\,\widetilde{\rho}_{e_k g_r}) + \Omega_{d g_r}\,\widetilde{\rho}^*_{d g_p} - \Omega^*_{d g_p}\,\widetilde{\rho}_{d g_r}\right].
\end{aligned}
\tag{2.19}
$$

Defining $N = M_g + M_e$ and taking into account the Hermiticity and preserved trace of the density matrix, this is a system of equations in N real and $(N^2+N)/2$ complex independent variables, as any one of the $N+1$ diagonal

density matrix elements can be described as a function of only the other N states.

Applying Ehrenfest's theorem in the rotating frame gives an expression for the force on the system,

$$F = -\hbar \left(\sum_{i,p} \mathrm{Re}\left[\widetilde{\rho}_{e_i g_p} \nabla \Omega^*_{e_i g_p} \right] + \sum_i \mathrm{Re}\left[\widetilde{\rho}_{e_i d} \nabla \Omega^*_{e_i d} \right] \right). \tag{2.20}$$

To evaluate the force on the system when it is moving at a particular velocity, the position dependence is mapped to a time-dependence with the replacement $z \to vt$ in the above equations. The velocity is treated as a fixed quantity, which is valid so long as it does not change significantly over a single full BCF cycle.

The BCF fields have been described up to this point as being symmetrically detuned from a resonance, with the counterpropagating beams having the same two frequencies. This will best address a system with zero velocity. Practically, it may be the case that it is preferred to create the strongest force at a non-zero velocity. In this case the optical frequencies can be adjusted to compensate the Doppler shifts by increasing the frequencies of both right-going components by kv_0 and decreasing the frequencies of both left-going components by the same amount. This sets an effective zero velocity of v_0, such that a system moving at v_0 in the lab frame will see Doppler-shifted frequencies which are symmetric about resonance, for $v_0 \ll c$. As this is always possible, it is sufficient to examine only the case where $v_0 = 0$, and the results are generalizable.

In experimental realizations, the relatively broad velocity range ($\sim \delta/k$ in a two-level system) makes it straightforward to stay sufficiently close to this symmetric configuration.

The system of coupled differential equations that describe the time evolution of the density matrix are generally amenable to numerical solutions, presenting no difficulty when evaluated using the ExplicitRungeKutta method of the NDSolve function of Mathematica (Appendix A).

When started with an incoherent system in the ground state, the density matrix undergoes transient behavior which damps out to a periodic quasiequilibrium. It is the behavior during this quasiequilibrium which is best used to calculate the typical force, so the system must be simulated out past the transient region. The initial RF phase of the BCF fields affects the transients' initial amplitude and decay time, as seen in Fig. 2.3. With an initial phase of 0°, the BCF cycling begins with a cycle-averaged force in the unintended direction. This inverts after a few spontaneous decay periods before settling to its quasiequilibrium. With an initial phase of 45°, the cycling starts in the intended mode and more quickly settles to the same quasiequilibrium. To increase the efficiency of calculations, the initial RF phase was always set to 45°.

The time-averaged force at a given velocity is computed by sampling the instantaneous force for at least 440 time points. At low non-zero velocities, there are oscillations in the instantaneous force at vastly different time scales, as can be

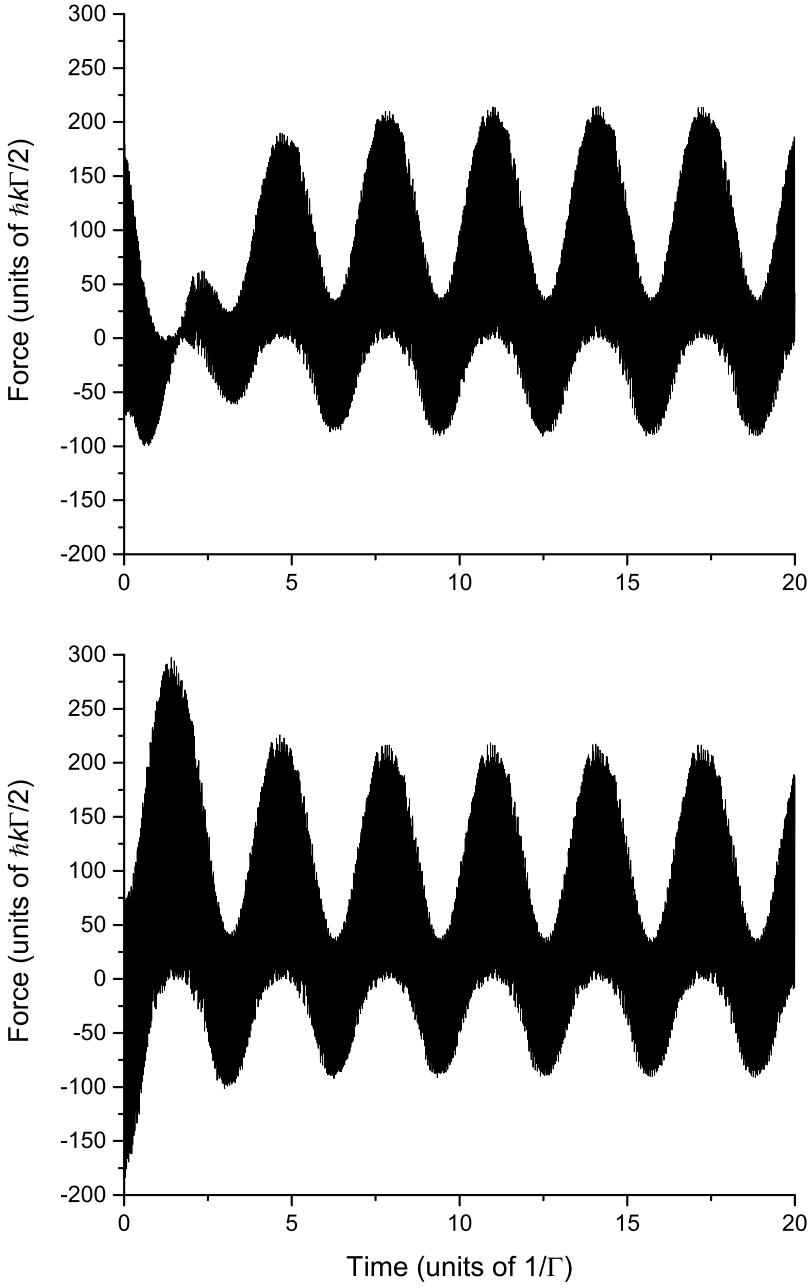

Fig. 2.3: The initial phase of the BCF fields effects the settling time beyond which the instantaneous force is nearly periodic. A two-level system was simulated at $\delta = 100\,\Gamma$ and $v = 1\,\Gamma/k$ with initial phases of $0°$ (top) and $45°$ (above). The instantaneous force versus time of each are shown.

seen in Fig. 2.3, and direct numerical integration across a full repetition period is computationally prohibitive. At these low velocities, the number of sampled time points is increased to better capture the data. Details of the sampling are provided in Appendix A.

In a 1+1 system without a distant dark state, that is to say a closed two-level system, the equations of motion and the force equation reduce to

$$\begin{aligned}
\dot{\rho}_{ee} &= -\mathrm{Im}\left[\Omega_{eg}^{*}\widetilde{\rho}_{eg}\right] - \gamma\rho_{ee} \\
\dot{\widetilde{\rho}}_{eg} &= \frac{i}{2}\left[2\Delta_{eg}\widetilde{\rho}_{eg} + \Omega_{eg}\left(\rho_{ee} - \rho_{gg}\right)\right] - \frac{\Gamma}{2}\widetilde{\rho}_{eg} \\
\dot{\rho}_{gg} &= \mathrm{Im}\left[\Omega_{eg}^{*}\widetilde{\rho}_{eg}\right] + \gamma\rho_{ee}
\end{aligned} \tag{2.21}$$

$$F = -\hbar\mathrm{Re}\left[\widetilde{\rho}_{eg}\nabla\Omega_{eg}^{*}\right] \tag{2.22}$$

where Δ_{eg} is the detuning of the central bichromatic frequency from the two-level resonant transition frequency. These equations are often re-written in the form of optical Bloch equations (OBEs) [16]:

$$\dot{u} = -\frac{\Gamma}{2}u - \Delta_{eg}v - \mathrm{Im}\left[\Omega_{eg}\right]w, \tag{2.23}$$

$$\dot{v} = \Delta_{eg}u - \frac{\Gamma}{2}v + \mathrm{Re}\left[\Omega_{eg}\right]w, \tag{2.24}$$

$$\dot{w} = \mathrm{Im}\left[\Omega_{eg}\right]u - \mathrm{Re}\left[\Omega_{eg}\right]v - \Gamma\left(1 + w\right), \tag{2.25}$$

where the Bloch vector (u, v, w) has components defined as

$$u \equiv 2\,\mathrm{Re}\left[\widetilde{\rho}_{eg}\right], \tag{2.26}$$

$$v \equiv 2\,\mathrm{Im}\left[\widetilde{\rho}_{eg}\right], \tag{2.27}$$

$$w \equiv \rho_{ee} - \rho_{gg}. \tag{2.28}$$

Numerically solving these equations of motion and computing the force (Fig. 2.4) shows that the optimum Rabi frequency of the two-level 1+1 system is given by

$$\Omega_{eg}^{0} = \sqrt{3/2}\,\delta, \tag{2.29}$$

the same result as obtained through Floquet analysis. This is significantly larger than the Rabi frequency that would make each individual beat a pi-pulse, which is $\pi\delta/4$ [28]. The peak force is as predicted by Eq. 2.4, and the force has an almost top-hat shaped profile against target velocity (Fig. 2.5), apart from some sharp spiking due to multiple-photon resonances that is not experimentally observable. The width is of order δ/k, though typically a bit smaller. This compares favorably to the radiative force, which does not have a region of constant force.

These predictions for the magnitude and velocity range of the BCF have been experimentally verified in a number of atomic systems which closely approximate closed two-level systems, including sodium [29], cesium [28], rubidium [38–40] and metastable helium [41–45]. The two-level BCF exceeds the two-level

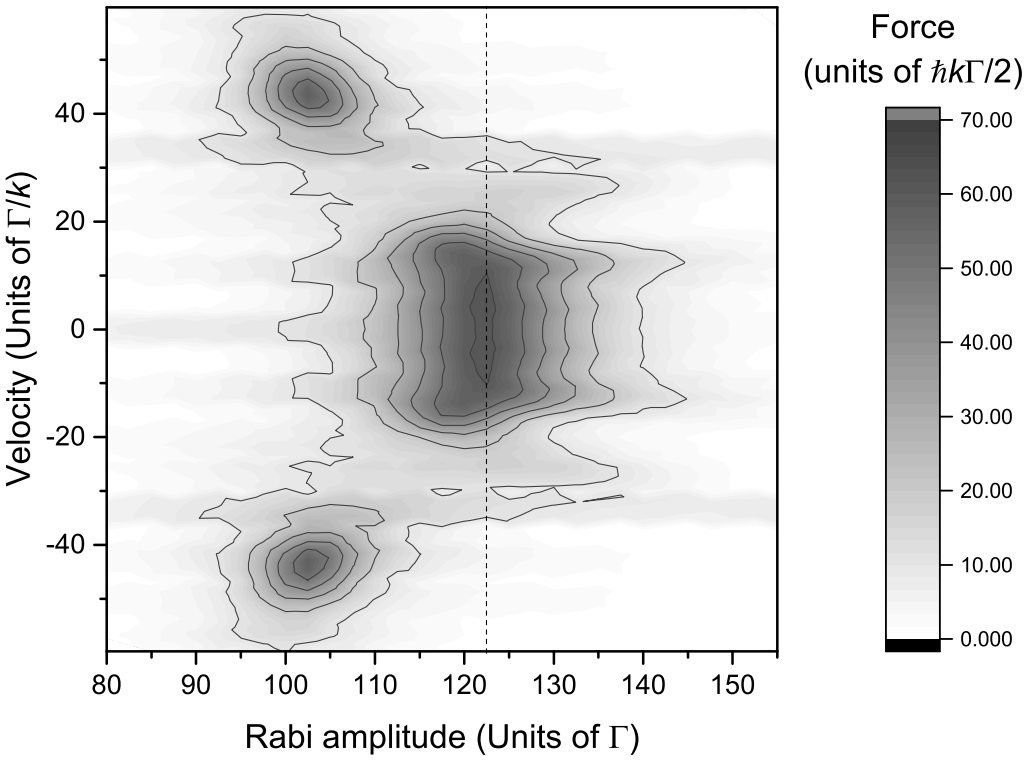

Fig. 2.4: Simulations of a two-level system under BCF illumination with parameters $\delta = 100\,\Gamma$ and $\chi = 45°$ across a range of Rabi amplitudes and velocities shows an optimal Rabi amplitude of $\sqrt{3/2}\,\delta$ (dashed line). The contour plot data is smoothed across 4.8 Γ/k of velocity range for clarity.

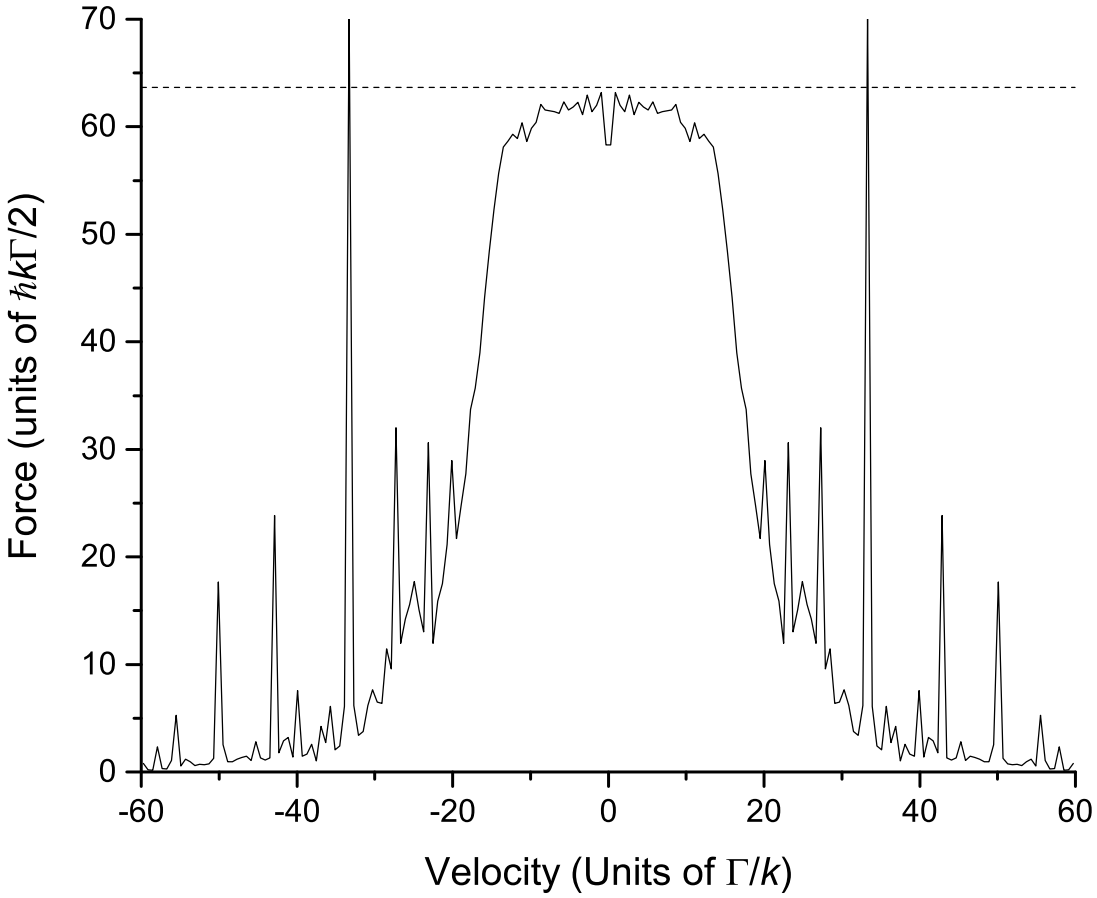

Fig. 2.5: Simulation of a two-level system under BCF illumination with parameters $\delta = 100\,\Gamma$ and $\chi = 45°$ at the optimal Rabi frequency $\sqrt{3/2}\,\delta$ shows the magnitude and velocity dependence of the BCF. The force near zero velocity is near the $(2/\pi)(\delta/\Gamma)$ (dashed line) predicted by simple arguments.

saturated radiative force by a factor of $(2/\pi)(\delta/\Gamma)$ and can be multiple orders of magnitude stronger for experimentally realizable optical fields.

2.4 Origin of BCF Robustness

From the first introduction of the bichromatic force, its robustness against deviations in laser field parameters was recognized, and by 1997 the Grimm group showed experimentally with Cs atoms that it is "insensitive against deviations from the ideal parameters by $\pm 10^\circ$ in the beat phase ... and $\pm 20\%$ in the total power and power balance [28]." Given that the BCF relies on coherent cycling, this aspect of the force is somewhat surprising. A non-ideal beat phase or power balance between the exciting and de-exciting beat trains would result in an excitation-deexcitation pair taking a ground state atom to a mixed final state, or in terms of the Bloch vector, the phase shift $\Delta \cos^{-1}(w) \neq 0$ over a pair of beats. If this phase shift were to accumulate over multiple beat pairs, the Bloch vector would continue to precess until it switched from deceleration to acceleration, or vice-versa. This would cause a force whose sign reverses periodically, giving a long-interaction-time average of zero force, rather than the consistent slowing force that has been observed.

A partial explanation for the observed robustness is the dephasing action of spontaneous decay [44], which resets the system to its ground state and erases any accumulated phase. If this were the only consideration, it would require a

spontaneous decay before the accumulated phase could reach π, which is the point at which the force would reverse sign. This places easily-estimated limits on the accuracy with which the light field parameters must be matched for the BCF beam pairs, which becomes more stringent as δ increases. This has also been posited as a reason for observed limits on high-detuning BCF [44].

However, as was noted in Ref. [44], the limits on deviations from optimal parameters that were obtained by appeal to dephasing events were stricter than the results of numerical simulation and the similar results of actual experiments. Clearly, some part of the coherent action of the BCF also plays a role in its robustness.

A clear insight into this mechanism can be gained by examining the behavior of a simplified system over a limited time interval. At zero velocity and at $z = 0$, Ω_{eg} remains real at all times, so that $u = 0$ identically when $\Delta_{eg} = 0$. This fact led Scott Galica to create "Bloch cylinder" plots which show v and w as a function of time, capturing the full behavior of a two-level resonantly-driven system at zero velocity [46]. A Bloch cylinder plot of ideal two-level BCF without spontaneous decay (Fig. 2.6) shows that direction of rotation of the Bloch vector reverses every π/δ, giving a total repetition period of $2\pi/\delta$, rather than just π/δ. This period includes two excitation-deexcitation beat pairs.

I linked this behavior to the sinusoidal envelope of each beat train, which reverses in sign every other beat (Fig. 1.3). As a consequence, the sign of the Rabi

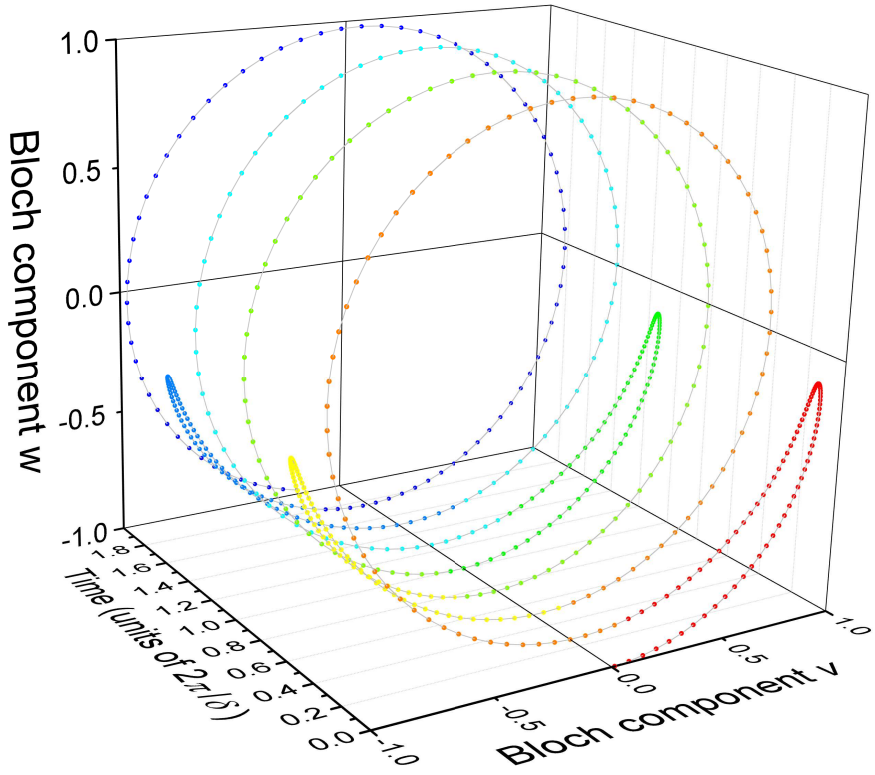

Fig. 2.6: A Bloch cylinder plot for two-level BCF at zero velocity and without spontaneous decay, with $\Omega_{eg} = \sqrt{3/2}\,\delta$ and $\chi = 45°$. Notable are the periodic reversals of rotation direction, which are due to the sinusoidal envelope of the beat trains which reverse sign every π/δ.

frequency reverses after each counterpropagating beat pair, causing the Bloch vector to reverse its direction of rotation. This reversal of rotation direction persists when the field parameters are not optimal, meaning that there is no phase accumulation over multiple cycles. Instead, any excess or deficit in phase rotation over one pair of beats is undone by the second pair of beats, because they have an equal excess or deficit, rotating in the opposite direction. A more careful analysis shows that the force does become more sensitive to deviations from optimal parameters at higher detunings, but at a much less severe rate than predicted by simple phase accumulation arguments [46].

Chapter 3

Polychromatic Forces

The average magnitude of the bichromatic force is determined in part by the fraction of time spent in "wrong-way" cycling that produces a negative force, as described in Chapter 2. This is unavoidable because the sinusoidal intensity envelope of the beats requires significant temporal separation of the beat peaks to establish clear ordering, leaving a mid-sequence gap during which spontaneous decay can shift population.

One possibility for improvement of the bichromatic force is to further shape the beats by the introduction of additional frequency components, extending it to a polychromatic force (PCF), as we have explored in Ref. [46]. This chapter summarizes the work described there, with a few additional insights. The ideal situation would be a sequence of infinitely narrow beat pairs with an infintesimal delay between them, such that ordering is established with a time-averaged excited-state fraction of zero. This would be accomplished if each of the two beat

trains had a Dirac comb envelope,

$$E_{Dirac} = E_0 \cos\left(\omega_{eg}^L \left(t \pm z/c\right)\right) \sum_{j=-\infty}^{\infty} \delta(t - jT), \tag{3.1}$$

with a Dirac delta function recurring with a repetition period T. The Dirac comb envelope has a cosine series expansion which follows

$$\sum_{j=-\infty}^{\infty} \delta(t - jT) \propto \sum_{n=0}^{\infty} \cos\left(\frac{\pi(2n+1)t}{T}\right) = \sum_{n=0}^{\infty} \cos\left((2n+1)\delta t\right), \tag{3.2}$$

for a fundamental frequency $\delta = \pi/T$. Much as the bichromatic sinusoidal envelope of frequency δ for a carrier frequency ω_{eg}^L was formed by overlapping cw fields of $\omega_{eg}^L \pm \delta$, this Dirac comb envelope is formed by overlapping cw fields of frequency $\omega_{eg}^L \pm (2n+1)\delta$, for n from 0 to ∞. This can be approximated by a truncated series,

$$E = E_0 \sum_{n=0}^{n_{\max}} \left[\cos\left(\left(\omega_{eg}^L + (2n+1)\delta\right)\left(t - z/c\right)\right) + \cos\left(\left(\omega_{eg}^L - (2n+1)\delta\right)\left(t - z/c\right)\right)\right] \tag{3.3}$$

for a beat train propagating in the $+\hat{z}$ direction. Similar to Eq. 2.11, the full corotating Rabi frequency when combining the $+z$- and $-z$-going beat trains is

written as

$$\begin{aligned}\Omega_{ij} &= 4\Omega_{ij}^{0}\sum_{n=0}^{n_{\max}}[\cos(kz)\cos((2n+1)\delta t)\cos((2n+1)\chi/2) \\ &+ i\sin(kz)\sin((2n+1)\delta t)\sin((2n+1)\chi/2)]. \qquad (3.4)\end{aligned}$$

At $n_{\max} = 0$, this reduces to the bichromatic arrangement with detunings $\pm\delta$ as previously seen. At $n_{\max} = 1$, detunings of $\pm 3\delta$ and $\pm\delta$ are required, and each beat train has an intensity envelope as shown in Fig. 3.1(a). The width of the largest lobe is clearly less than in the bichromatic case, which should allow the optimal phase shift χ to be less and to reduce the average excited state fraction. It is worth noting that the spacing between the large lobes is exactly equal to the width of those lobes, such that at $\chi = 90°$, the counterpropagating beats would not overlap at all. Thus at $n_{\max} > 1$, each excitation-deexcitation pair of beats will be well-separated from the next, marking a qualitative difference from the BCF arrangement.

Simulating a 1+1 system with a four-color field ($n_{\max} = 1$) across a range of Ω_{ij}^{0} and χ (Fig. 3.2) showed that the optimal $\Omega_{ij}^{0} = \delta$ and the optimal $\chi = 31.2°$. The optimal Rabi frequency amplitude is smaller in terms of δ than in the bichromatic case, but there are eight component lasers rather than four. As irradiance goes as the square of Rabi frequency, the four-color PCF requires 4/3 the total laser power at a given detuning, but produces 3/2 the force magnitude,

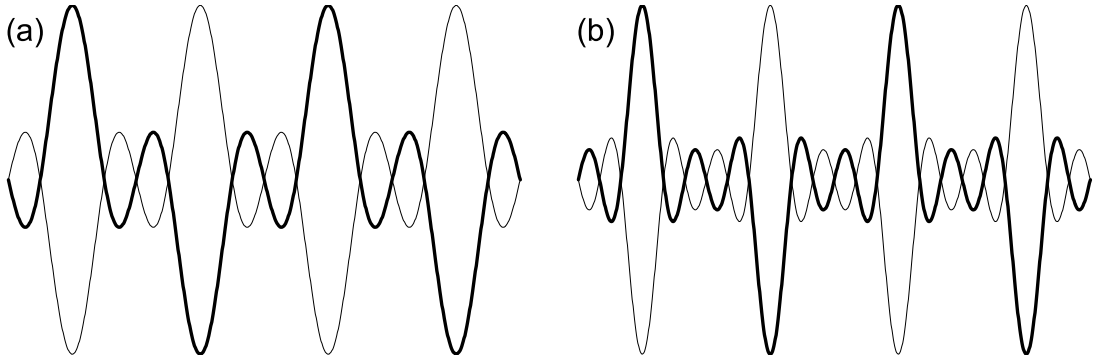

Fig. 3.1: Field envelopes for the truncated cosine series of the Dirac comb for (a) $n_{\max} = 1$ and (b) $n_{\max} = 2$. The sign of the envelope is indicated with bold lines. The lobe of greatest intensity becomes narrower as $n_{\max}$ increases.

for an overall increase in force per unit laser power by a factor of 9/8. The velocity range is also significantly increased, to about double the velocity range for BCF of the same fundamental detuning (Fig. 3.3), or 50% wider for the same total laser power. The excited state fraction also decreases to 28% from 41% for BCF.

At $n_{\max} = 2$, with "hexachromatic" beat trains, the optimal field parameters are $\Omega_{ij}^0 = \delta$ and $\chi = 21.1°$ (Fig. 3.4), and the optimal force is about 8/7 of the optimal 4-color force at the same δ(Fig. 3.3). This requires 3/2 the total laser power as the 4-color force, so the force per laser power is actually lower with a $n_{\max} = 2$ field than with a $n_{\max} = 1$ field by a factor of 16/21, and by a factor of 6/7 as compared to BCF. However, the excited-state fraction is further reduced to 20%, so in situations where a small excited state fraction is crucial, this may be a useful arrangement.

As is the case for bichromatic fields, for these polychromatic fields a full

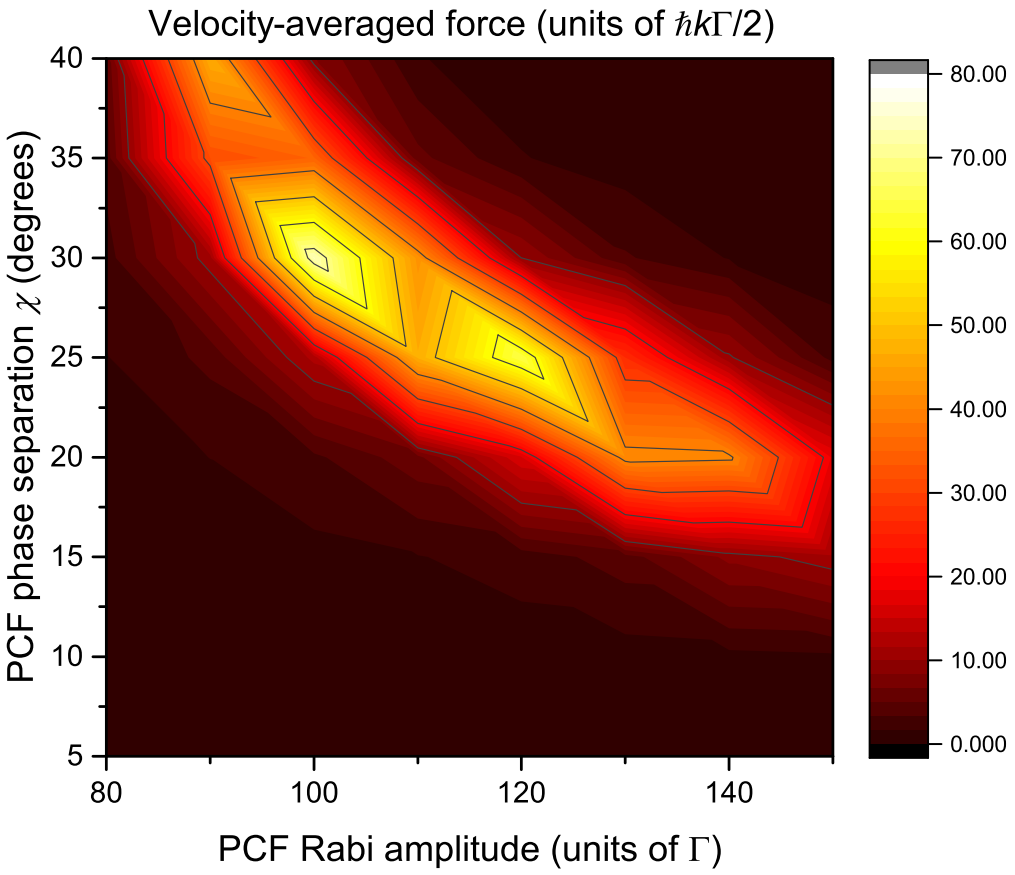

Fig. 3.2: Four-color polychromatic force at a fundamental detuning of $\delta = 100\,\Gamma$, averaged over the velocity range $|v| < 30\,\Gamma/k$, for a range of PCF field parameters. The optimum force occurs near $\Omega^0 = \delta$ and $\chi = 30°$.

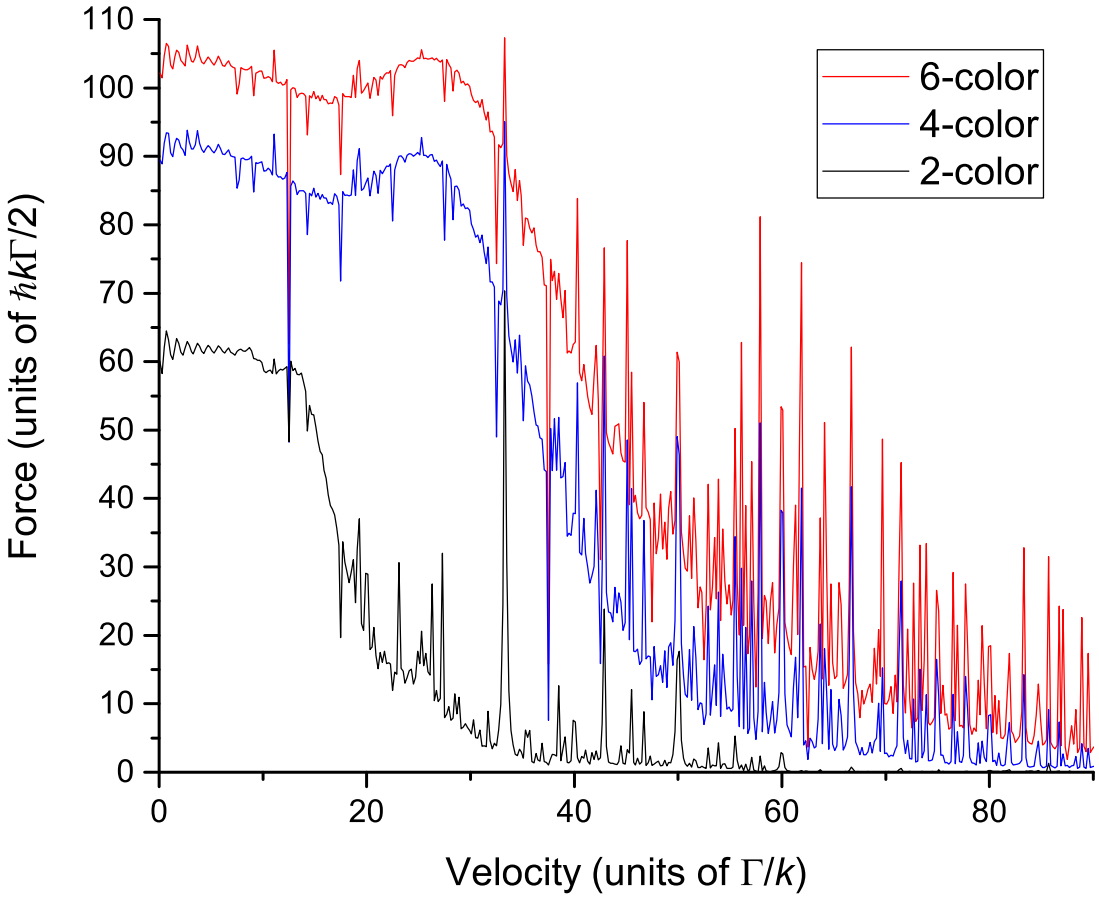

Fig. 3.3: Optimum force vs. velocity profiles for PCF driving at a fundamental detuning of $\delta = 100\,\Gamma$ with two, four, and six colors. The increase in force between four and six colors in less dramatic than the increase between two and four colors. The force is symmetric about zero velocity.

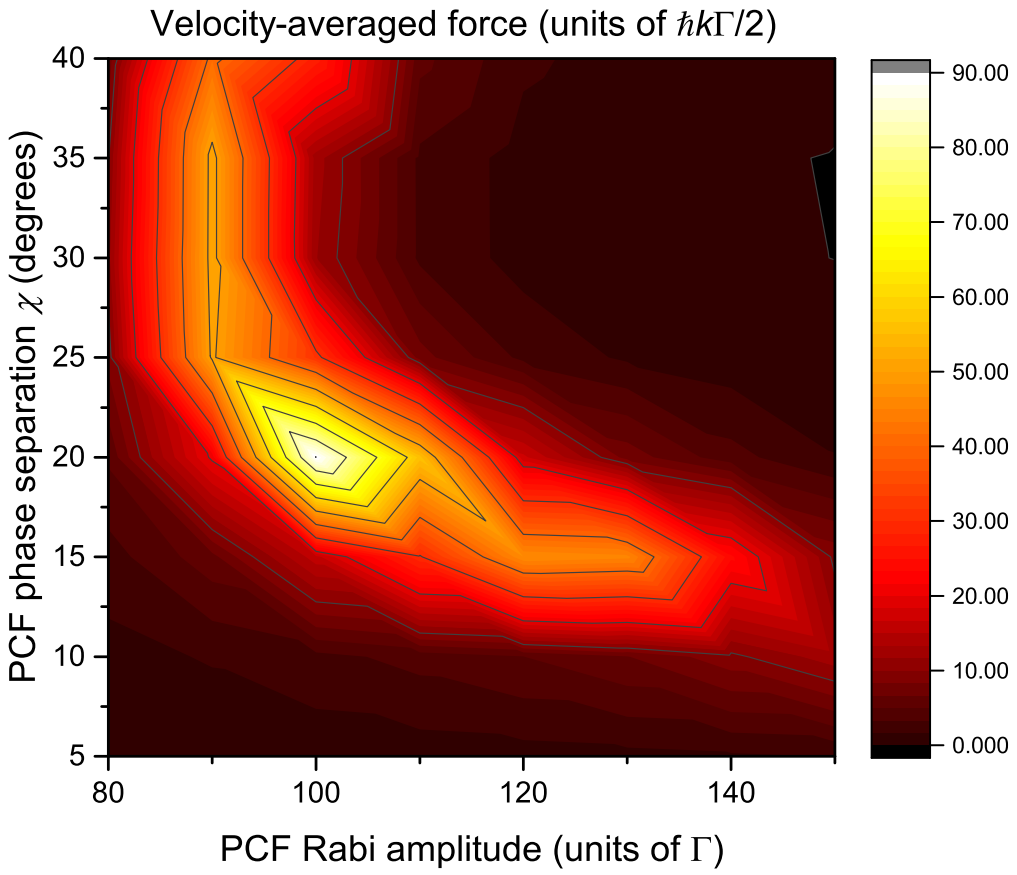

Fig. 3.4: Six-color polychromatic force at a fundamental detuning of $\delta = 100\,\Gamma$, averaged over the velocity range $|v| < 48\Gamma/k$, for a range of PCF field parameters. The optimum force occurs near $\Omega^0 = \delta$ and $\chi = 20°$.

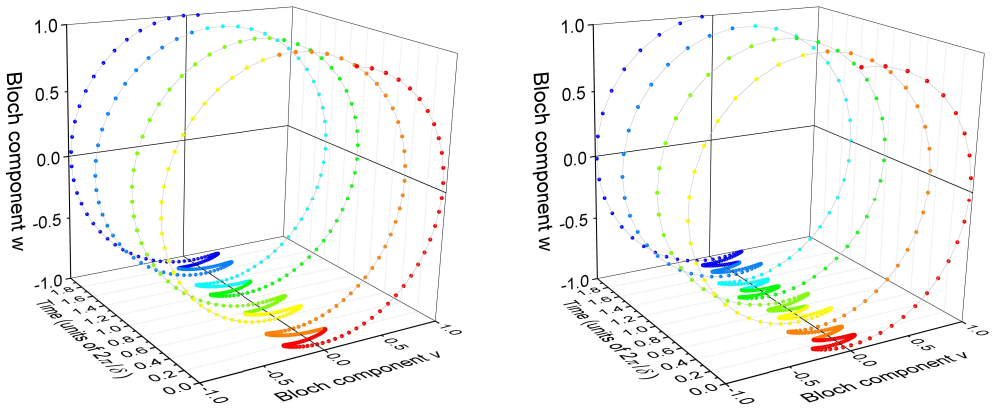

Fig. 3.5: Bloch cylinder trajectories for $n_{\max} = 1$ (left) and $n_{\max} = 2$ (right) PCF without spontaneous decay. Just as for the BCF, the rotation direction around the Bloch cylinder reverses at intervals of δ/π. The overshoot past the ground state is much smaller than with the BCF, and the system passes through the excited state more rapidly as $n_{\max}$ increases, as can be seen by the larger spacing between the points, which are plotted at fixed time intervals.

repetition period of the driving field envelope includes two of the primary beat note lobes from each direction, which alternate in sign. This causes the same wrapping and unwrapping of the Bloch vector (Fig. 3.5), giving the same robustness against power imbalances. For the PCF with optimal parameters, the excursions past the ground state before the precession direction reverses are several times smaller than in the BCF case, and the system passes through the excited state more rapidly. Both of these differences contribute to the lower excited-state fraction (Fig. 3.6).

In the laboratory, the 4-color PCF field could be produced by starting with a monochromatic laser of frequency $\omega - \delta$, then passing it through an acousto-optic modulator (AOM) driven with an acoustic wave at frequency 2δ, and finally retroreflecting both the zero-order and first-order beams after the AOM, in a minor

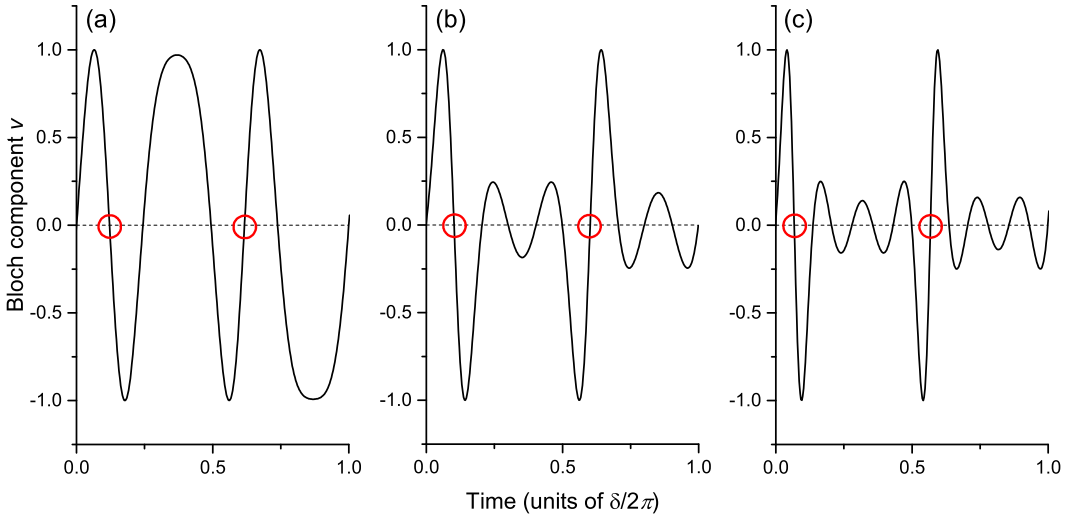

Fig. 3.6: The v component of the Bloch vector over a full two-pulse-pair oscillation for optimal (a) BCF, (b) 4-color PCF, and (c) 6-color PCF, without spontaneous decay. The value v=0 corresponds to the system being fully in either the ground or excited state, so the zero crossings that correspond to the excited state are circled for clarity. Oscillations around the ground state during the nominal "off" time between pulse pairs are much smaller in the two PCF cases than in the BCF case, but are of approximately equal magnitude between 4-color and 6-color PCF.

modification of the BCF scheme described in Ref. [38] (Fig. 3.7). This produces one output beam containing frequencies $\omega + \delta$ and $\omega - 3\delta$ and a second output beam containing frequencies $\omega - \delta$ and $\omega + 3\delta$. If these two beams are mixed on a 50/50 beamsplitter, two beams with the full 4-color PCF configuration are created, which can then be used as the two counterpropagating beams.

Alternatively, a system of two AOMs could be used, each driven at 2δ, with a mirror redirecting the first-order deflected beam from the first AOM into the second AOM (Fig. 3.7). This would duplicate the effects of the double-passed single AOM arrangement, but would allow the second AOM, which produces the $\pm 3\delta$ frequencies, to be independently tuned. This would allow for testing of predictions for the optimum relative power in the first and third harmonics.

Another option for producing sidebands is through use of an electro-optic modulator (EOM), which can create sidebands on an optical field by adding a time-dependent phase [47]. Unlike AOMs, EOMs do not produce an angular deflection of the different frequency components. If the 4-color PCF field were to be produced, all of the sidebands would need to be of the proper magnitude directly out of the EOM. In particular, the δ and 3δ sidebands should have equal magnitude and all other sidebands, including the carrier, should have zero magnitude.

If a voltage modulation $\beta \sin(\delta t)$ is applied to an EOM with light of frequency ω passing through it, frequency-modulated light with a time dependent

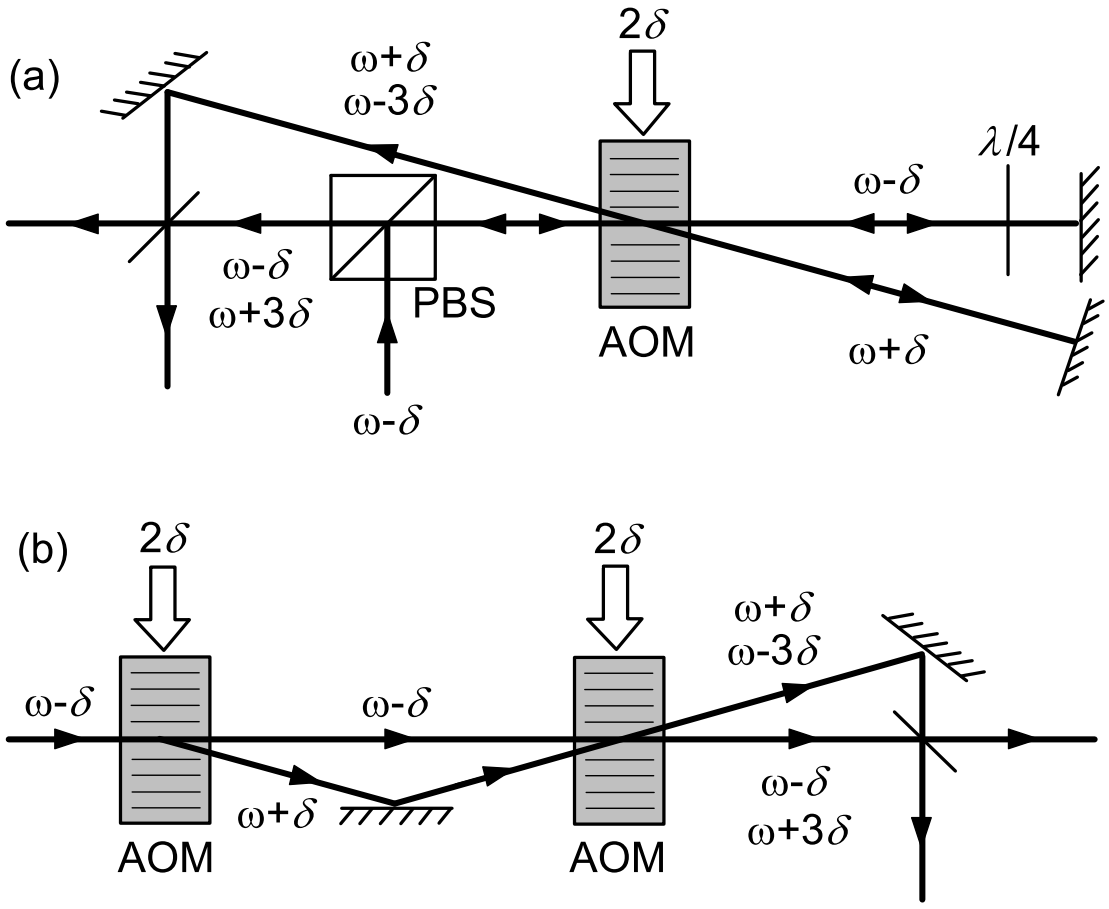

Fig. 3.7: Acousto-optic modulator (AOM) arrangements for creating 4-color PCF fields. In the single-AOM arrangement (a), a quarter-wave plate ($\lambda/4$) and a polarizing beam splitter (PBS) are used to separate the input and output beams after retroreflection. In the two-AOM arrangement (b), the relative powers of the first and third harmonic components can be tuned. In both cases, a beam containing frequencies $\omega - \delta$ and $\omega + 3\delta$ and a beam containing frequencies $\omega + \delta$ and $\omega - 3\delta$ are created with different propagation directions and are mixed on a 50/50 splitter to create two beams with the full 4-color PCF field.

phase results, with time dependence [47]

$$E = E_0 e^{i(\omega t + \beta \sin(\delta t))} = E_0 e^{i\omega t} e^{i\beta \sin(\delta t)}. \tag{3.5}$$

The final term can be expanded using the Jacobi-Anger expansion [48] as

$$e^{i\beta \sin(\delta t)} = \sum_{k=-\infty}^{\infty} J_k(\beta) e^{ik\delta t} \tag{3.6}$$

where J_k is the kth Bessel function of the first kind.

With voltage modulation of the EOM at a frequency δ, the magnitudes of the δ and 3δ sidebands are equal at $\beta = 3.05, 6.71, 9.97...$, but at none of these modulation amplitudes is the carrier magnitude zero. These two criteria can be simultaneously satisfied by driving the EOM at multiple frequencies δ and 3δ with magnitudes β and γ respectively, so that the total time-dependence of the electric field is given by

$$\begin{aligned} E &= E_0 e^{i\omega t} e^{i\beta \sin(\delta t)} e^{i\gamma \sin(3\delta t)} \\ &= E_0 e^{i\omega t} \sum_{k=-\infty}^{\infty} J_k(\beta) e^{ik\delta t} \sum_{\ell=-\infty}^{\infty} J_\ell(\gamma) e^{i\ell 3\delta t} \\ &= E_0 e^{i\omega t} \sum_{k=-\infty}^{\infty} \left(e^{ik\delta t} \sum_{n=-\infty}^{\infty} J_{k-3n}(\beta) J_n(\gamma) \right) \end{aligned} \tag{3.7}$$

The small amplitudes which simultaneously produce equal magnitude in the first and third harmonics and zero magnitude in the carrier are shown in

Fig. 3.8. Unfortunately, none of these points in parameter space also suppresses the second harmonic, and generally they do not suppress higher harmonics. Thus the scheme fails to produce the required four-color PCF field. It is possible that adding additional frequencies to the EOM driving modulation, or altering the phase between the driving frequencies, might allow for a closer reproduction of the desired light field. However, this added complication makes the relatively simple AOM-based alternative more appealing by comparison.

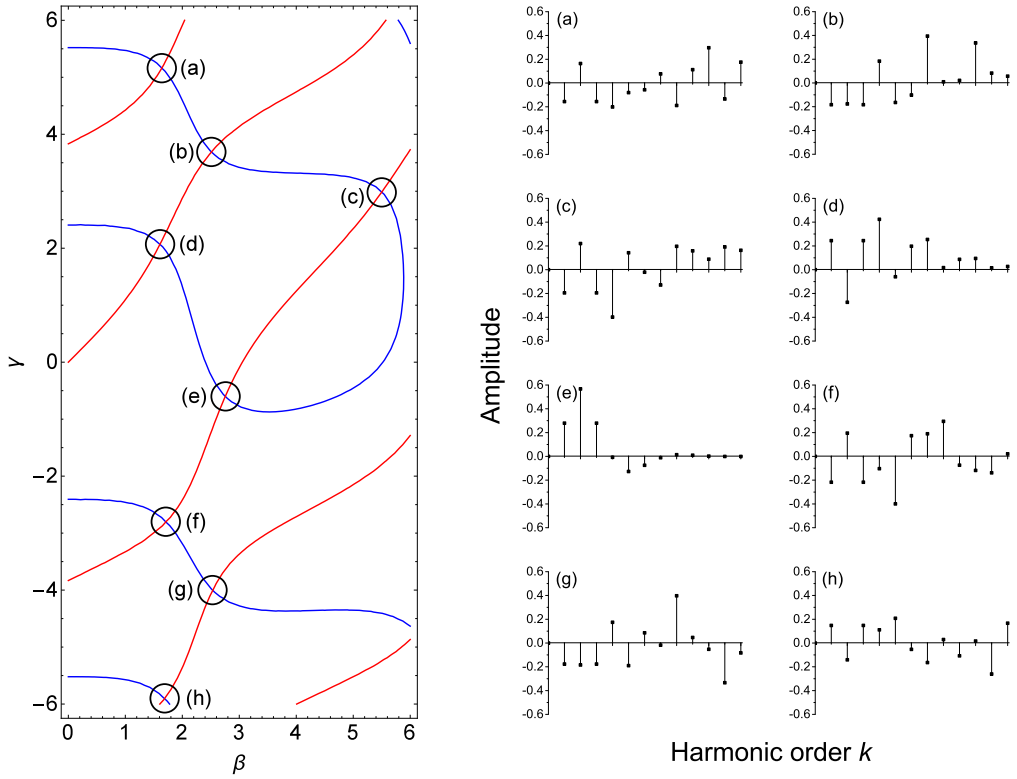

Fig. 3.8: Contours along which the carrier frequency of an optical wave passing through an EOM is suppressed (left, blue) and the first and third harmonics are of equal amplitude (left, red) when the EOM is driven with a sinusoidal voltage modulation at frequency δ and amplitude β together with a second sinusoid at frequency 3δ and amplitude γ. The sideband spectra of the outputs at the crossing points of the two sets of contours are shown on the right. None reproduce well the truncated Dirac comb series that we expect to be optimal for PCF experiments.

Chapter 4

Simplified Multi-Level Systems

When dealing with systems more complicated than the two-level 1+1 systems considered up to this point, a number of additional considerations arise. This chapter examines these complications in simple multilevel systems where they can be isolated, before applying the results to realistic molecular systems in Chapter 5. The majority of this chapter reprises work that was previously published in Ref. [49], with the exception of Sec. 4.4 which is original to this dissertation.

4.1 2+1 'Λ' Systems

The bichromatic force relies on time-dependent excited- and ground-state populations which synchronize with the intensity modulation of the bichromatic beat trains. This synchronization allows for the preferential absorption from one train and preferential emission into the other. In system of multiple states, which are coupled to each other via a network of two-state coherent couplings by optical fields, complicated coherences arise that do not necessarily lend themselves to the arguments which predict the two-level BCF as laid out in Chapter 2.

In order to examine the functioning of the BCF in coherently-coupled multilevel systems, a 2+1 lambda-type system (Fig. 4.1) was simulated first. Each of two lower levels, $|g_1\rangle$ and $|g_2\rangle$, are coupled through the same BCF optical field to an upper level, $|e_1\rangle$. The transition dipole moments of the two transitions in this model system are set to be different from each other, such that there is a fixed proportion between the Rabi frequencies on each transition, $\Omega_{e_1g_1} = \sqrt{2}\,\Omega_{e_1g_2}$. As a direct consequence, $\gamma_{11} = 2\gamma_{22}$. The unperturbed energy levels of the lower levels are set such that $\omega_{g_2} - \omega_{g_1} = 100\,\Gamma$, where $\Gamma = \gamma_{11} + \gamma_{12}$. These two aspects of the system, differing lower state energies and differing Rabi frequencies, comprise the main concerns with applying BCF to closed multilevel systems. Simulating the response of this lambda-type system shows how best to deal with multiple transitions, at least one of which will necessarily be off-resonant and at a non-optimal BCF Rabi frequency.

To aid comparisons, a total Rabi frequency amplitude Ω^{tot} is defined as the quadrature sum of the two Rabi amplitudes,

$$\Omega^{\text{tot}} = \sqrt{\left(\Omega^0_{e_1g_1}\right)^2 + \left(\Omega^0_{e_1g_2}\right)^2}. \tag{4.1}$$

When the bichromatic detuning is small compared to the splitting between the two lower levels ($\delta << |\omega_{g_1} - \omega_{g_2}|$), it is not possible to position the carrier frequency ω^L_{eg} of the BCF field to simultaneously address both transitions effec-

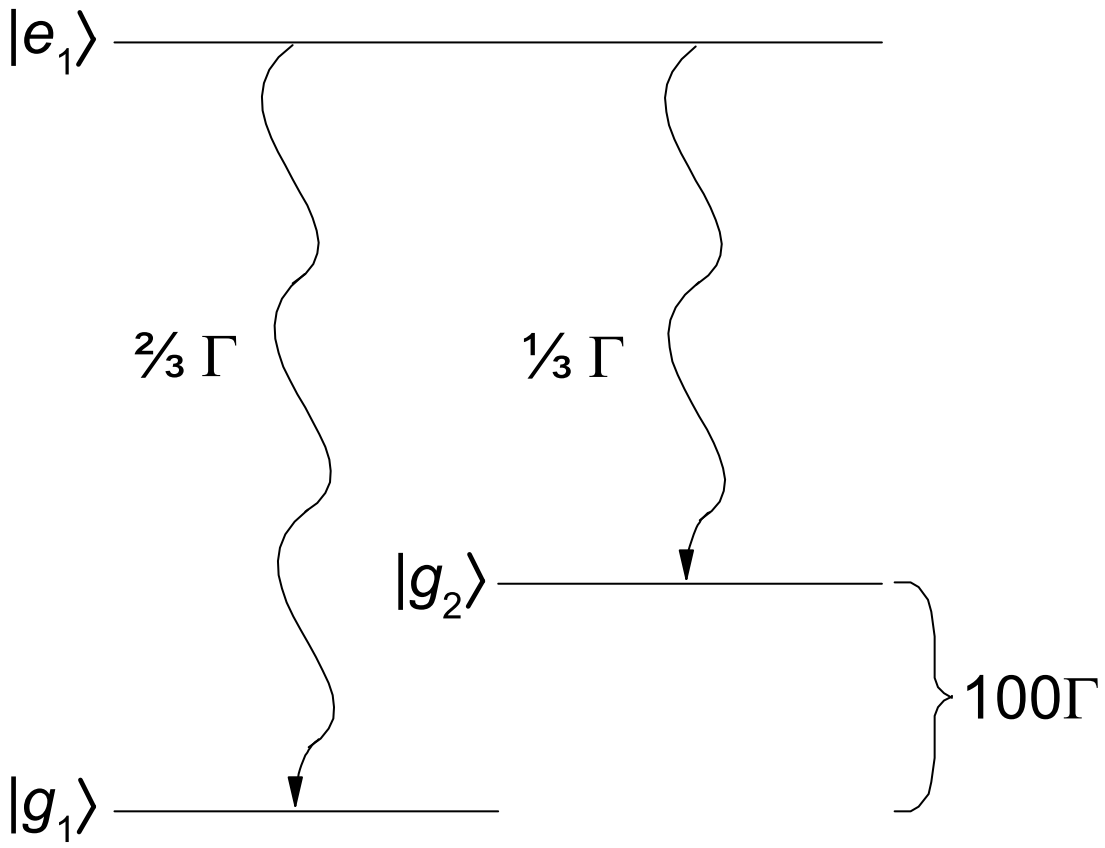

Fig. 4.1: The 2+1 system simulated in Section 4.1. Decay rates and the ground-state splitting are indicated; the ratio of Rabi frequencies on each transition was set equal to the ratio of the square roots of the branching fractions. This figure is reproduced from Ref. [49].

tively. In this small-detuning regime, simulations of the model 2+1 system show that a BCF carrier frequency resonant with one transition or the other gives a stronger force than a BCF carrier frequency tuned between the two transitions, as then, at least, one transition is being effectively addressed. When ω_{eg}^{L} is resonant with one of the transitions, the other transition sees the light as essentially a single-frequency laser, because the differences in detunings from the second transition are small compared to the average of these detunings. This acts as an effective off-resonant repump, preventing the system from pumping entirely into the non-resonantly-addressed state.

Force profiles for the cases where the BCF carrier frequency is resonant with either $|e_1\rangle \leftrightarrow |g_1\rangle$ or $|e_1\rangle \leftrightarrow |g_2\rangle$ were simulated at a fixed small detuning $\delta = 15\,\Gamma$ for a range of Ω^{tot} (Fig. 4.2). These simulations show that, in the small-detuning regime, the individual Rabi frequency of the transition aimed at should be tuned to be the optimal two-level Rabi frequency, $\sqrt{3/2}\,\delta$. Cuts at the optimal Rabi frequency in each case show force profiles which are similar in magnitude near zero velocity and in velocity range. This may be expected, as these depend only on δ in the two-level case at optimal irradiance. A possible problem with this argument may be the differing coupling strengths of the two transitions leading to differing population dynamics in the lambda-type system when selecting one or the other transition as the primary BCF transition. These population dynamics are therefore addressed in some detail.

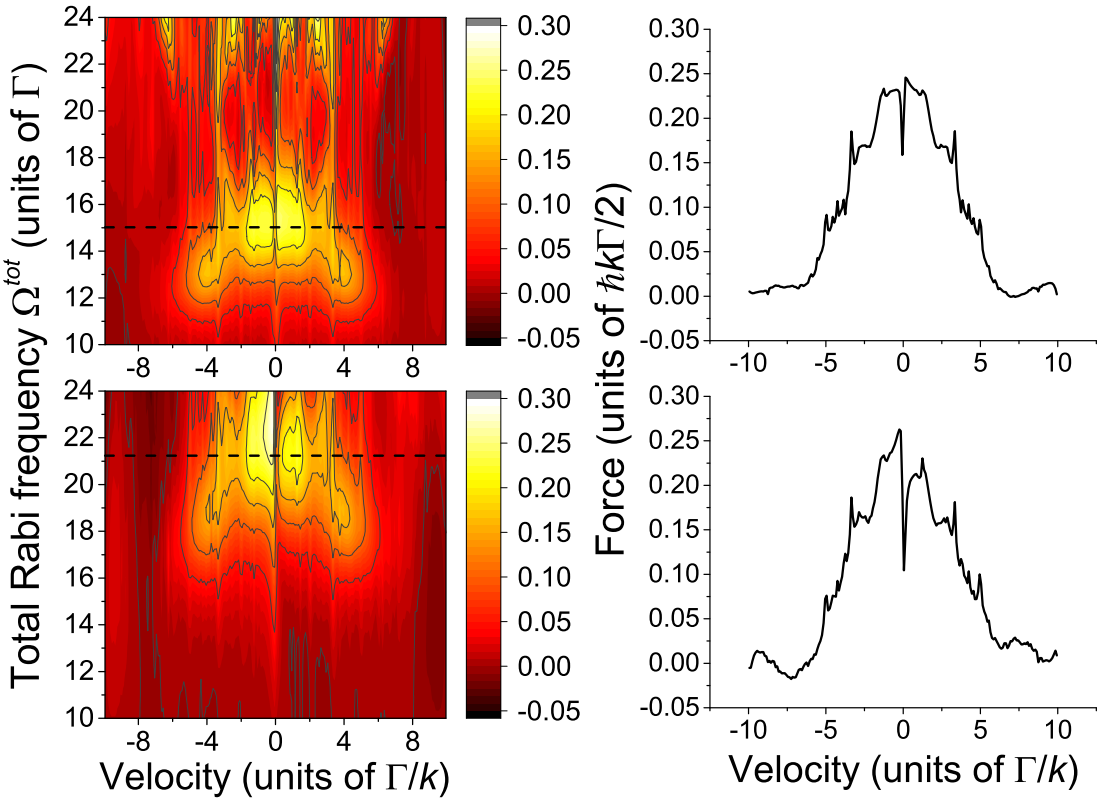

Fig. 4.2: BCF force from simulations of a lambda-type system, with the BCF carrier frequency resonant with the $|e_1\rangle \leftrightarrow |g_1\rangle$ transition (top) or the $|e_1\rangle \leftrightarrow |g_2\rangle$ transition (bottom). Force contours as a function of the total Rabi frequency Ω^{tot} and velocity (left) reveal the optimum Ω^{tot} for each transition (dashed line) which, though at different irradiances, result in similar force vs. velocity profiles (right). This figure is reproduced from Ref. [49].

When a two-level system is driven with resonant monochromatic illumination, and neglecting radiative decays, the population cycles between being fully in the ground state and fully in the excited state. With the inclusion of radiative decay, these oscillations are damped and the system settles at long times to a steady state of equal population in the ground and excited states. In a lambda system where both legs are driven by the same cw monochromatic field, assuming the $|e_1\rangle \leftrightarrow |g_1\rangle$ transition is being driven resonantly, the steady-state excited population becomes [50]

$$\Omega_{e_1g_1}^2 \Omega_{e_1g_2}^2 \Gamma \Delta_{e_1g_2}^2 / \mathcal{O}\left(\Omega_{e_1g_1}^6, \Omega_{e_1g_2}^4\right), \tag{4.2}$$

where $\Delta_{e_1g_2}$ is the detuning of the light from the $|e_1\rangle \leftrightarrow |g_2\rangle$ transition, and the $\mathcal{O}$ notation shows the leading powers in the two Rabi frequencies of the denominator. Full expressions for the populations in each of the three states of the lambda-type system can be found in Ref. [50]. If $\Delta_{e_1g_2} \neq 0$ and $\Omega_{e_1g_2} \neq 0$, there is a non-zero excited state population in the steady state. This means that the system remains at least partially bright, continuing to absorb light. However, the excited-state population is reduced compared to the resonantly-driven two-state system, and some population collects in the off-resonant state. For the model lamdba-type system discussed in this section, where the same optical field is coupling both ground states to the excited state, the detuning from resonance

for the second transition will necessarily be $\Delta_{e_1 g_2} = \omega_{g_2} - \omega_{g_1}$ in the case that the $|e_1\rangle \leftrightarrow |g_1\rangle$ transition is being resonantly driven. When the driving fields are in the BCF arrangement and in the small-detuning regime, as previously discussed it is expected that only the transition being resonantly addressed will contribute to the force. The total force in this arrangement should therefore be reduced by a factor of the fraction of the population in the states which are resonantly coupled, which can be estimated by calculating the steady-state $\rho_{e_1 e_1} + \rho_{g_1 g_1}$ in the monochromatic case.

This estimate is validated by simulation results (Fig. 4.3) of the model lamdba-type system for a range of small bichromatic detunings. In each case the carrier frequency ω_{eg}^{L} was set to the $|e_1\rangle \leftrightarrow |g_1\rangle$ transition frequency and the total Rabi frequency amplitude was set to the optimum for that transition. Due to the increase in the participating population fraction roughly proportional to $\Omega_{e_1 g_2}^2$ in this range of Rabi frequencies, and therefore roughly proportional to δ^2, the average force near zero velocity is roughly proportional to δ^3, remembering that the two-level BCF is proportional to δ. Up to a bichromatic detuning of one-quarter of the ground-state energy splitting, the force closely follows a curve defined by the product of the two-level bichromatic force and the equilibrium participating population fraction calculated from the monochromatic excitation case. This effectively defines the limits of the small-detuning regime. For this calculation, a single δ-independent fitting parameter of effective monochromatic Rabi frequency

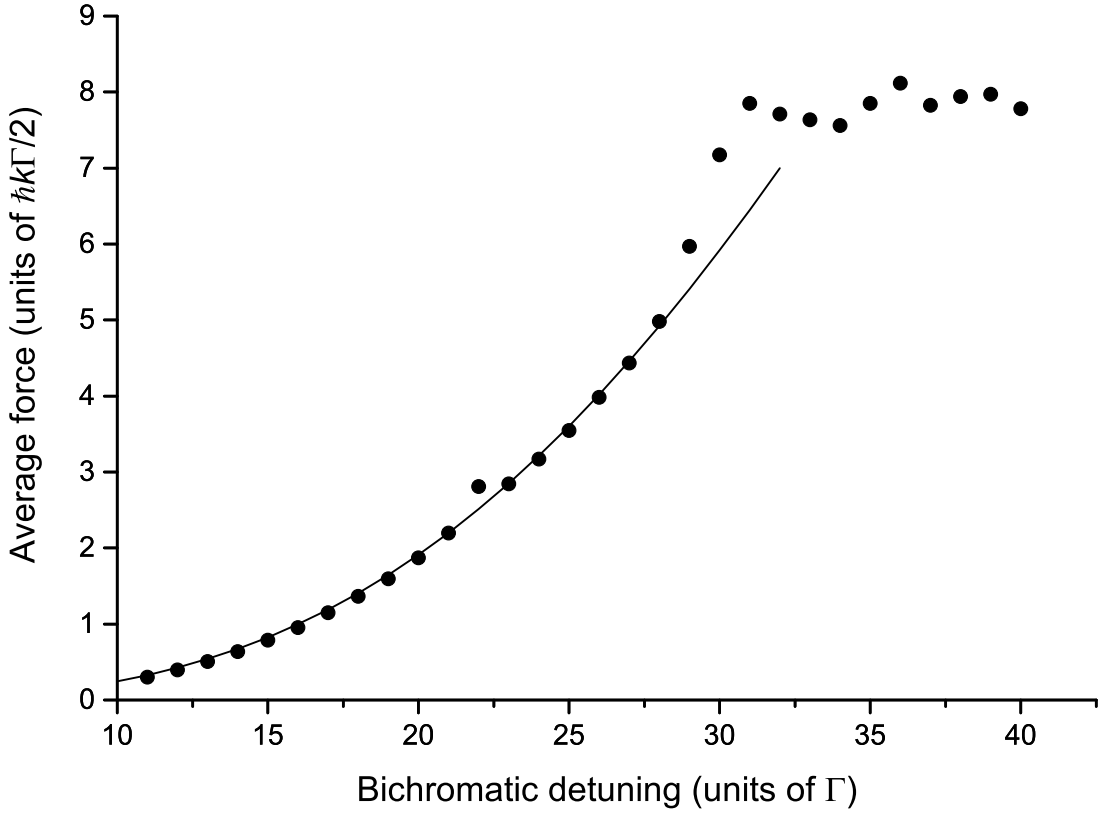

Fig. 4.3: Velocity-averaged force for BCF with carrier frequency resonant with the $|e_1\rangle \leftrightarrow |g_1\rangle$ transition of the system shown in Fig. 4.1. The Rabi frequency amplitude is $\Omega^0_{e_1 g_1} = \sqrt{3/2}\,\delta$ throughout. Points show results of direct simulation and the line shows the two-level force times an estimated participating fraction calculated for monochromatic excitation (see text). Beyond $\delta \approx 25\Gamma$, the system transitions to the intermediate-detuning regime. This figure is reproduced from Ref. [49].

was used to account for the actual driving having a time-dependent intensity. The best-fit effective monochromatic Rabi frequency was found to be 2.040(19) Ω^{tot}.

While the magnitude of the force scales non-linearly with detuning in the small-detuning regime, the velocity range of the force still scales linearly with detuning, as it does in the two-level case. A linear regression of the full-width at half-maximum (FWHM) of the force profiles vs. detuning gives a best-fit FWHM of 0.706(12) δ/k. This is wider than the FWHM of two-level BCF force profiles, such as in Fig. 2.5, due primarily to a softening of the edges beyond the small-velocity force plateau and not to any widening of that plateau.

In Fig. 4.3 it can also be seen that past the small-detuning regime, the force levels off, with no further increase in force between $\delta = 30\,\Gamma$ and $\delta = 40\,\Gamma$. Past this and approaching $\delta = \omega_{g_2} - \omega_{g_1}$, the force decreases to nearly zero. The model lambda-type system was simulated at a range of detunings crossing this intermediate-detuning region and at a range of total Rabi frequency amplitudes (Fig. 4.4). In this intermediate region, no total Rabi frequency amplitude produces any significant force. The near resonance of one of the bichromatic frequencies with the $|e_1\rangle \leftrightarrow |g_2\rangle$ transition completely disrupts the coherent BCF cycling in this arrangement, producing a "dead zone" in bichromatic detunings which must be avoided if a force is to be produced.

At detunings which are large compared to the ground-state splitting ($\delta \gg |\omega_{g_2} - \omega_{g_1}|$), a BCF can be produced at a $\Omega^{\text{tot}}/\delta$ lower than that in the small-

detuning region, as can be seen in the lower-right of Fig. 4.4. In this large-detuning regime, the splitting between the ground states becomes insignificant and the two states act as a single superposition state, so it might be expected that Ω^{tot} should satisfy the BCF criterion $\Omega^{\text{tot}} = \sqrt{3/2}\,\delta$. In this case, coherent effects are advantageous, as they allow for the use of less laser irradiance to produce the optimal force than would have been needed for either trainsition individually. It remains the case that the strongest force is produced when keeping the BCF carrier frequency resonant with the stronger transition.

In the large-detuning regime, the force and velocity range both grow linearly with δ when Ω^{tot} is scaled to remain at the δ-dependent optimal value (Fig. 4.5). In this particular lamdba-type system, the slopes of this linear growth are found by least-squares fitting to be 0.258(22) $\hbar k/2$ for the force and 0.123(21) $1/k$ for the FWHM velocity range. These are each below the equivalent slopes in the ideal two-level case, 0.637 $\hbar k/2$ and 0.3 1/k.

In summation, when dealing with a set of ground states coupled to a single excited state, the optimal arrangement for producing a bichromatic force is to have the quadrature sum of the Rabi frequencies of the transitions addressed bichromatically equal to $\sqrt{3/2}\,\delta$. To be "addressed bichromatically" is essentially to have one of the bichromatic frequencies be blue-detuned of resonance, and the other red-detuned. For sufficiently small detunings, the set of transitions addressed bichromatically will collapse to only one transition, and in that case

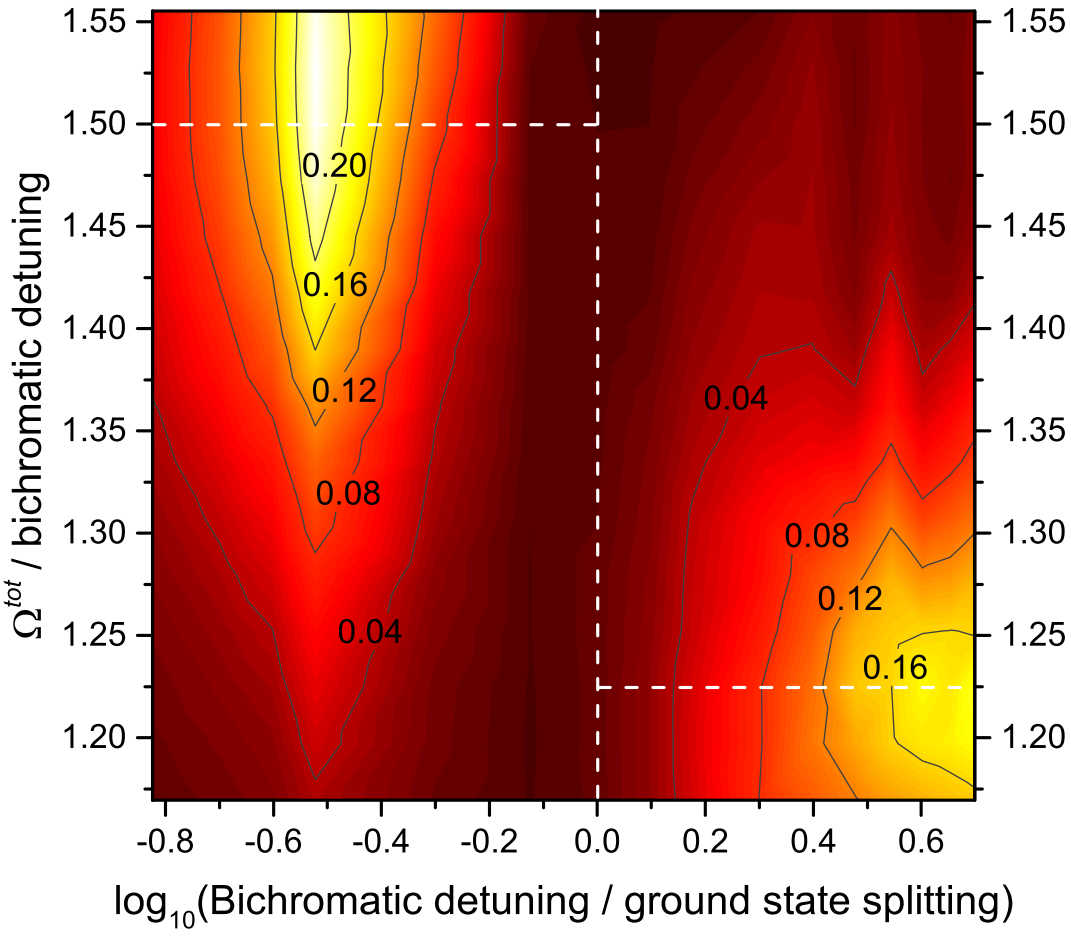

Fig. 4.4: Velocity-averaged force in an asymmetric lambda-type system, scaled by the bichromatic detuning δ, for a range of δ. The contours are given in units of $\hbar k/2$. Results show a "dead zone" in the force near $\delta = |\omega_{g_1} - \omega_{g_2}|$ (vertical dashed line), and very different optimal values of $\Omega^{\rm tot}/\delta$ in the small- and large-detuning regimes (horizontal dashed lines). This figure is reproduced from Ref. [49].

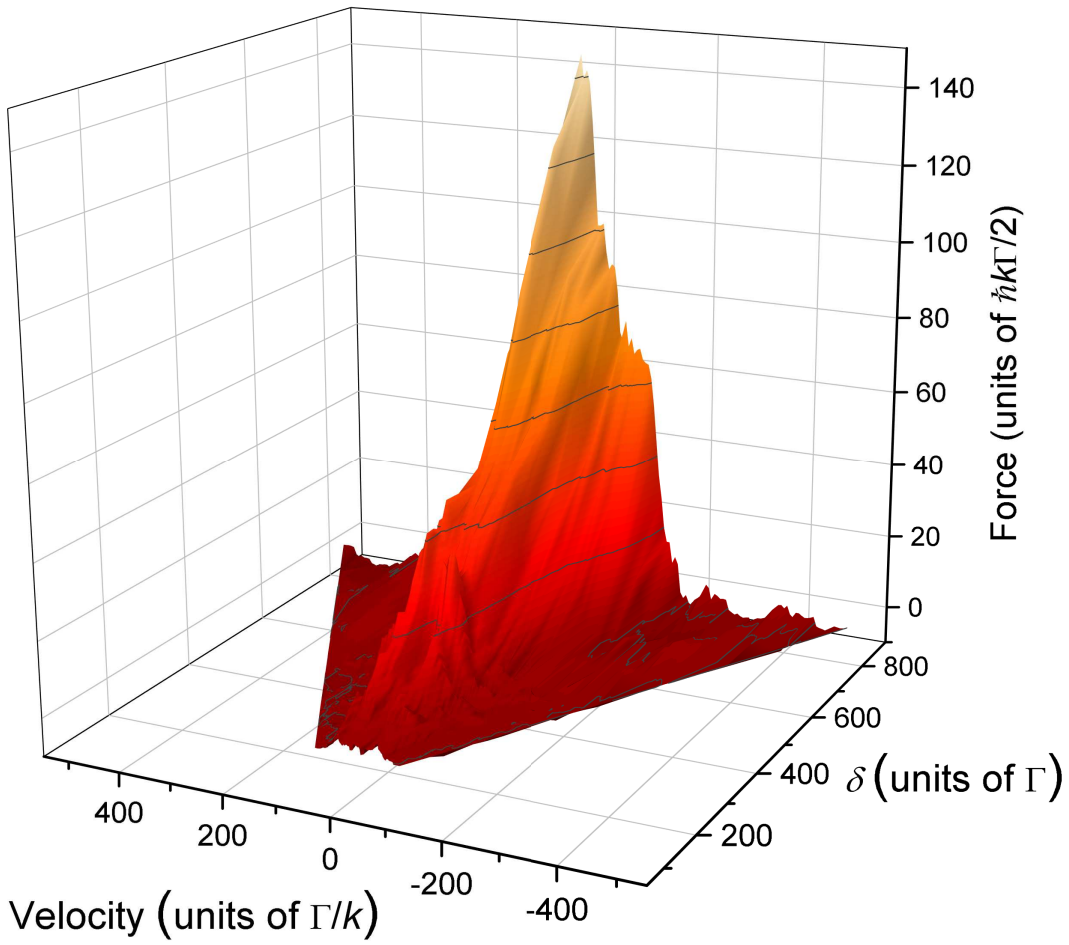

Fig. 4.5: Force due to large-detuning BCF in the Fig. 4.1 system. Data was smoothed over a velocity range of 0.1 δ/k. Both the force near zero velocity and the velocity range of the force increase with increased bichromatic detuning. This figure is reproduced from Ref. [49].

its individual Rabi frequency should be equal to $\sqrt{3/2}\,\delta$. In the large-detuning regime, all of the transitions are addressed bichromatically, and the total Rabi frequency amplitude Ω^{tot} should be equal to $\sqrt{3/2}\,\delta$. The intermediate case, where some transitions are addressed near-resonantly by only one of the bichromatic frequencies, destroys the bichromatic force and is to be avoided. For congested systems, where the small-detuning regime would require detunings so small as to no longer be large compared to the excited-state decay rate, this leads to an effective lower limit on useful bichromatic detunings given by the size of the energy splittings in the ground-state manifold.

4.2 Dark State Destabilization in Multilevel Systems

In multi-level systems without distant states, it is still possible for the system to evolve into an intrasystem dark state. This may be due to states existing which are inaccessible due to electric dipole selection rules, or particular coherent superpositions of degenerate states may have no excitation dipole amplitude for a given exciting field. If these states are populated in part by incoherent radiative decay, the dark fraction will grow over time as there will be some overlap of the incoherent decay state with the coherent dark superposition. For any system in which the ground-state has two more degenerate projection quantum states m than the excited-state multiplicity, there will exist two such dark superposition states regardless of the polarization of light used to couple the two manifolds [51].

Preventing the accumulation of population in these dark states has been a matter of prior study [51,6]. As such accumulation would cause the BCF to rapidly diminish to zero, two schemes for the prevention of dark state accumulation in the presence of BCF fields are investigated here. The first is the application of a skewed dc magnetic field and the second is rapid switching of the optical polarization state.

4.2.1 Skewed Magnetic Field

The application of a dc magnetic field to a state with angular momentum J and degeneracy $2J+1$ causes two primary effects, each due to precession of the electronic angular momentum around the magnetic field. The first is a breaking of the degeneracy of the $2J+1$ M_J levels due to Zeeman shifting; the size of these shifts is proportional in first order to M_J. The second is a mixing of the M_J levels, in the case that the magnetic field is not parallel to the quantization axis. Using both of these effects to destabilize dark states, by applying a dc magnetic field at a skewed angle to the exciting laser polarization, has been analyzed in detail in Ref. [51] and has been succesfully deployed in the context of radiative slowing of molecules in a number of cases [13].

To simulate the effects of using a skewed dc magnetic field to destabilize dark states while producing a bichromatic force, it is assumed here that the bichromatic fields are linearly polarized and that the polarization axis defines the quantization

axis z of the target system. The magnetic field is assumed to lie in the $x-z$ plane and is expressed in spherical tensor notation as

$$\vec{B} = \frac{B}{\sqrt{2}}\sin(\theta_{BE})\hat{T}_1^{-1} + B\cos(\theta_{BE})\hat{T}_1^0 - \frac{B}{\sqrt{2}}\sin(\theta_{BE})\hat{T}_1^{+1}, \tag{4.3}$$

where θ_{BE} is the angle between the magnetic field vector and the laser polarization axis.

The magnetic-field Hamiltonian is modeled by adding the additional terms

$$\frac{H_B}{\hbar} = \mu_B\left(\sum_{p,q}\vec{B}\cdot(g_s\hat{S} + g_L\hat{L}) + \sum_{i,j}\vec{B}\cdot(g_s\hat{S} + g_L\hat{L})\right) \tag{4.4}$$

to the Hamiltonian given in Eq. 2.12. Magnetic interactions with nuclear spins are neglected because they are generally small, and magnetic coupling between ground and excited states is neglected because for small dc magnetic fields this coupling is extremely small compared with typical optical energy level separations.

The simplest system on which to test this dark state destabilization scheme is a ${}^3P_0 \leftrightarrow {}^3S_1$ system, which is in the nomenclature used here a 3+1 system. The response of this system is simulated under BCF illumination in the presence of a skewed dc magnetic field, where the magnetic field units are scaled such that the first-order Zeeman shift is equal to $M_J B\cos(\theta_{BE})$ and B is expressed in units of the total excited-state decay rate Γ.

In this system, where $\hat{J} = \hat{L} + \hat{S}$ is the total angular momentum, and

only interactions between states of the same J, L, and S but differing M_J are considered, the matrix elements of the magnetic-field Hamiltonian are given by

$$\langle L,S;J,M_J|\,\frac{H_B}{\hbar}\,|L,S;J,M_J'\rangle = \mu_B(-1)^{S+L+2J-M_J+1}\,(2J+1)\times$$
$$\sum_{\zeta=L,S} g_\zeta\sqrt{\zeta(\zeta+1)(2\zeta+1)}\begin{Bmatrix}\zeta & J & J\\ J & \zeta & 1\end{Bmatrix}\sum_p B_p\begin{pmatrix}J & 1 & J\\ -M_J & p & M_J'\end{pmatrix}, \quad (4.5)$$

where $B_p = \vec{B}\cdot\hat{T}_1^p$. That this gives the correct matrix elements can be seen from Eqs. 5.126, 5.129, 5.135 and 5.138 of Ref. [5]. This shows that the self-interaction and therefore energy shift of a state is proportional to $B_0 = B\cos(\theta_{BE})$ and the coupling strength between adjacent projection states, $|M_J - M_J'| = 1$, is proportional to $B_1 = B/\sqrt{2}\sin(\theta_{BE})$, as the three lower terms in the three-J symbol must sum to zero for it to have a non-zero value.

In this arrangement, the optical BCF field couples only the $M_J'' = 0$ state to the excited state, and the magnetic field remixes any population that decays into the other projection states back into $M_J'' = 0$. As only the one transition is being addressed by the bichromatic fields, all the simulations discussed in this section have the Rabi frequency of that individual transition set to $\sqrt{3/2}\,\delta$.

Results from simulations with a fixed bichromatic detuning $\delta = 100\,\Gamma$ and across a range of magnetic field strengths and angles (Fig. 4.6) show a clear optimum set of magnetic field parameters. Away from this optimum, a ridge in the force follows a curve of constant $\sqrt{2}\,B\sin(\theta_{BE})$, meaning that there is a preferred

coupling strength between the ground states.

When the same set of simulations across magnetic field parameters was performed at various bichromatic detunings, the same pattern emerged. It was found that the optimal value of $\sqrt{2}\,B\sin(\theta_{BE})$ scales with the square-root of the bichromatic detuning, and additionally that the optimal Zeeman splitting $B\cos(\theta_{BE})$ scales linearly with the bichromatic detuning. Specifically, in the ${}^3P_0 \leftrightarrow {}^3S_1$ system, it was found by least-squares fitting that the optimal values for these parameters are

$$\begin{aligned} \sqrt{2}B\sin(\theta_{BE}) &= 1.184(31)\sqrt{\delta\Gamma}, \\ B\cos(\theta_{BE}) &= 0.2054(35)\delta. \end{aligned} \tag{4.6}$$

Eq. 4.6 can be rearranged to give expressions for the optimum magnetic field strength and angle in this system, directly:

$$\begin{aligned} B &= \delta\sqrt{0.700(37)\Gamma/\delta + 0.0422(14)}, \\ \theta_{BE} &= \tan^{-1}\left(4.07(13)\sqrt{\Gamma/\delta}\right). \end{aligned} \tag{4.7}$$

At the optimum magnetic field parameters, the magnitude of the bichromatic force scales linearly with the bichromatic detuning (Fig. 4.7). Least-squares fitting to the simulation data gives the average force near zero velocity as $F = 0.1203(27)\hbar k\delta$. In the ideal two-level case, the force is $F = 0.3183\hbar k\delta$, which is

around three times larger. In this system, three ground states are being constantly remixed and only one of them is bichromatically coupled to the excited state, so a force-reduction factor of about 1/3 is not unexpected.

For other multilevel systems the details will differ, but the basics of this remixing scheme can be expected to be similar, as can the scaling rules.

4.2.2 Polarization Switching

The use of a skewed dc magnetic field mixes the projection states of the system, reintroducing population into the state that is addressed by the optical fields. Another option for dealing with the build-up of population in dark states is to periodically change which states are dark. This can be accomplished by periodically changing the polarization state of the optical fields. In the simplest system which satisfies $J'' = J' + 1$, one where $J'' = 1$ and $J' = 0$, three polarization states are needed to completely prevent pumping into a dark state, as any two two-dimensional dark subspaces of the three-dimensional ground manifold will necessarily overlap in at least one superposition state. Thus, any two polarizations will necessarily have a mutual dark state. It is not possible to have three linearly-independent polarization states in a beam with a single propagation direction, so using polarization switching in this simplest system would require the addition of a new laser beam at a skewed angle [51]. For such a system, the skewed **B** field method is greatly preferable.

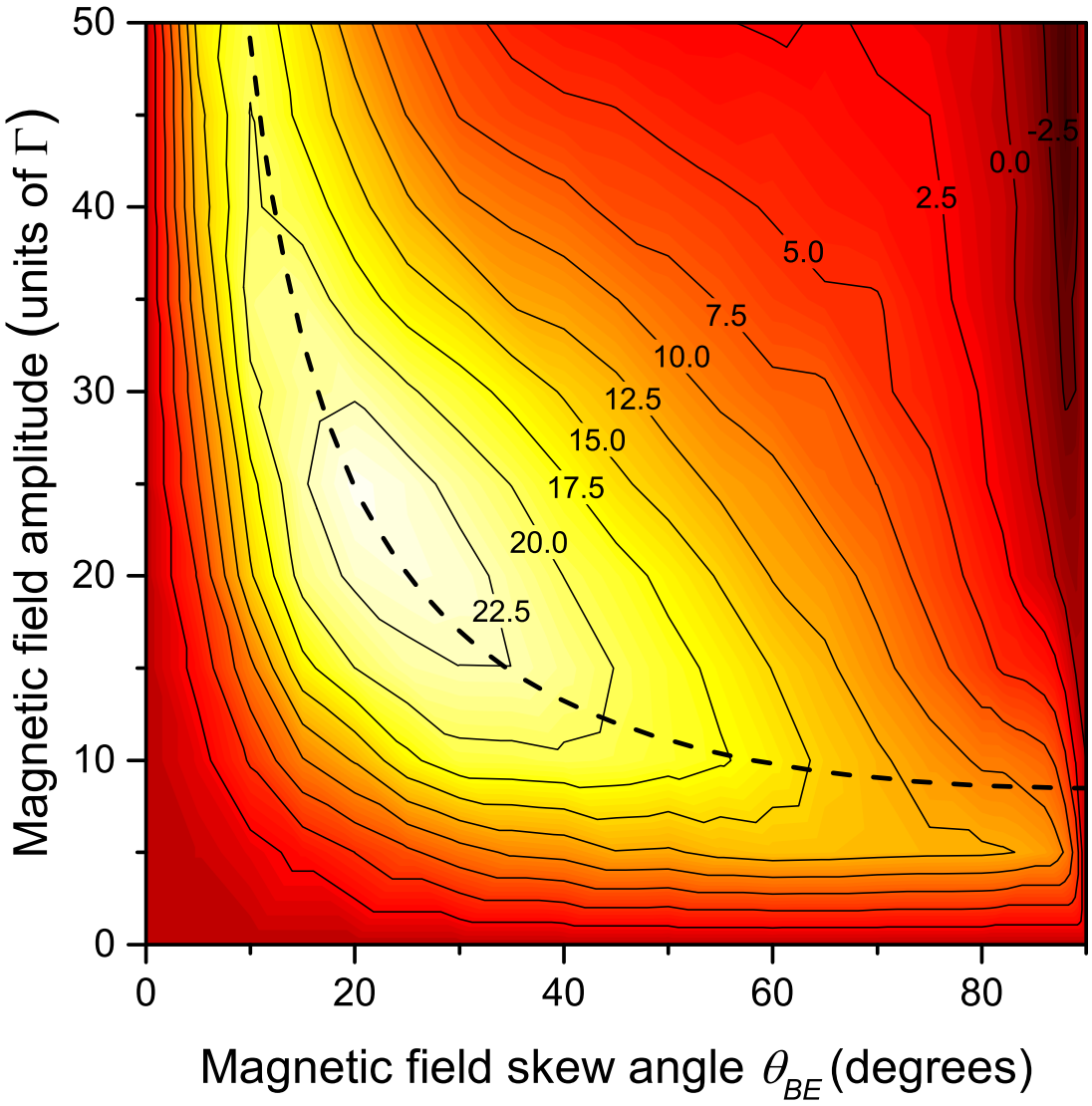

Fig. 4.6: Contours of velocity-averaged force for a ${}^3S_1 \leftrightarrow {}^3P_0$ system driven by a linearly-polarized BCF field of $\delta = 100\,\Gamma$ and $\Omega = 122.5\Gamma$, with a dc magnetic field of varying amplitude and angle. The dashed line that follows the ridge of the force defined by $\sqrt{2}B\sin(\theta) = 12\Gamma$. This figure is reproduced from Ref. [49].

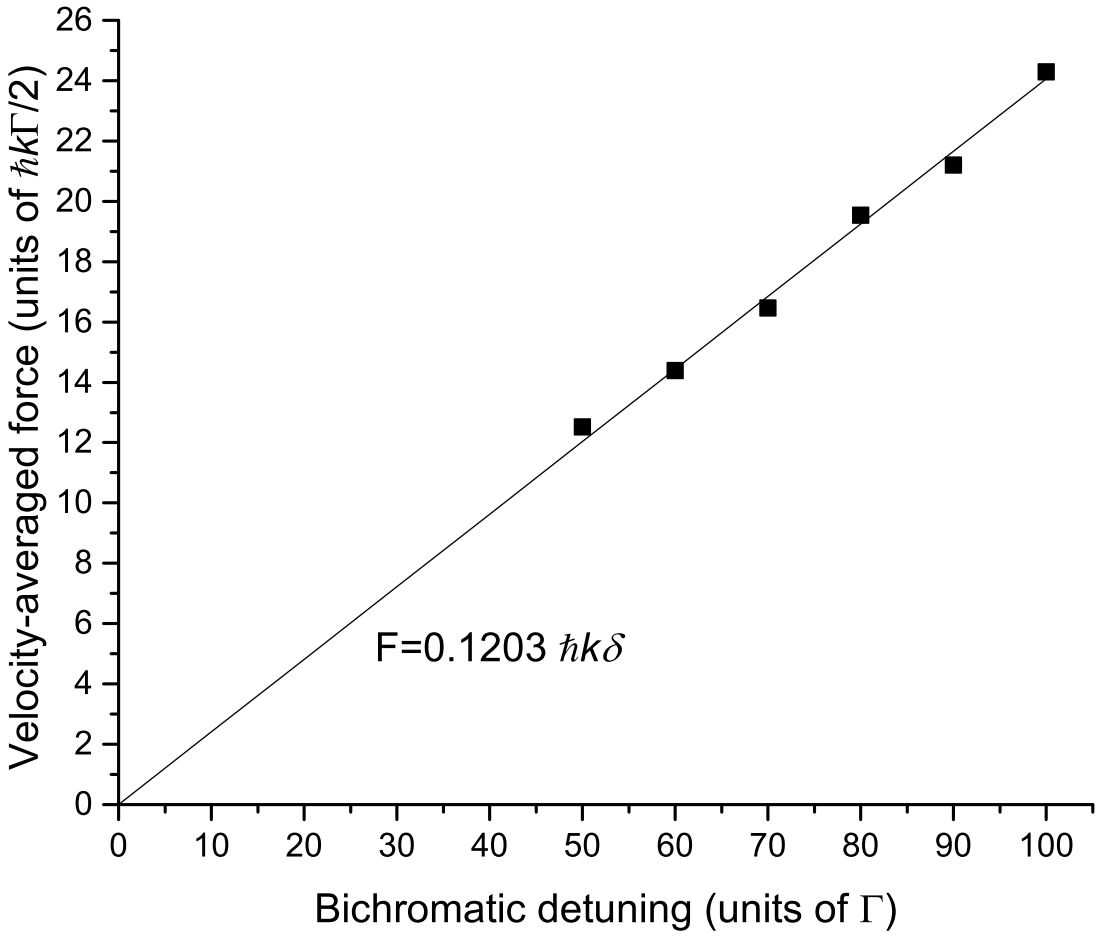

Fig. 4.7: At optimum magnetic field parameters and Rabi frequency, the bichromatic force with magnetic remixing in a ${}^3S_1 \leftrightarrow {}^3P_0$ system results in an average force that scales linearly with bichromatic detuning and is approximately one-third of the ideal two-level bichromatic force. This figure is reproduced from Ref. [49].

Transitions which satisfy $J'' = J' + 1$, but with $J'' > 1$, are more easily handled by way of polarization switching between σ^+ and σ^- polarization. For example, in a $J'' = 2 \leftrightarrow J' = 1$ transition, defining the quantization axis along the k-vector of the stimulating light, σ^+ light leaves $m'' = 1$ and $m'' = 2$ dark, while σ^- light leaves $m'' = -1$ and $m'' = -2$ dark. Clearly the dark-state spaces for these polarizations do not overlap, and the necessary polarization switching can readily be performed on a collinear pair of beams.

The simplest system for which polarization switching would be both necessary and feasible with just the collinear BCF beams is one with $J'' = 2$ and $J' = 1$. Such a system was simulated with a 5+3 $^5P_1 \leftrightarrow {}^5S_2$ arrangement with the polarization of the BCF field switched between σ^+ and σ^-. The switching was set to occur instantaneously with half-period T, as the pulse area of each bichromatic beat is crucial to the proper functioning of the bichromatic force. A smooth switching between one polarization and the other would entail non-constant pulse areas and would give poor results during the switch-over.

While one of the two polarizations is on, the system population will be optically pumped into the dark states, leading to a continual decrease in participating fraction. Each time the polarization switches, the system rephases and the coherence on which the BCF relies begins to build up. These two competing effects mean that a finite optimal switching time is expected.

To produce the strongest force, the coherence build-up time should be as

short as possible. In Chapter 2, it was shown that in the two-level case, the equilibration of the coherent cycling into its long-time quasiequilibrium was fastest if the initial phase of the bichromatic fields is set to $\theta = 45°$. In most of the simulations discussed in this disseration, the transient behavior is not included in evaluations of the force, as it is assumed to make up an insignificant part of the total interaction time. However, in this polarization switching scheme, the system is continually "shocked" and the transient behavior becomes significant. Simulations for which the global phase of the bichromatic fields is reset to a particular value θ at each polarization switch show that $\theta = 45°$ does result in the strongest time-averaged force, as expected. $\theta = 0°$, for which two-level simulations showed an initial reverse force, results in a weak reverse force in this switching scheme as well.

In the ${}^5P_1 \leftrightarrow {}^5S_2$ system, the transition dipole matrix elements of the three transitions driven by σ-polarized light are not equal. This results in differing Rabi frequencies for each transition, leading to some ambiguity about what laser irradiance will produce the strongest force. The BCF polarization switching scheme was simulated in this system at $\delta = 100\,\Gamma$ for a range of irradiances and switching times T. These simulations showed that the strongest force is achieved when the Rabi frequency on the $m' = 0 \leftrightarrow |m''| = 1$ transition is equal to $\sqrt{3/2}\,\delta$. A switching time of $T \approx 5/\Gamma$ is optimal (Fig. 4.8), with a shallower decline on the long-T side. The force at optimal switching time and Rabi frequency is approximately

$20\hbar k\Gamma/2$, which is about 1/3 of the ideal two-level force at the same bichromatic detuning.

In order to achieve these results in an experimental context, the polarization switching cycle must be phase-locked to the bichromatic beats. If the switching cycle is allowed to free run, the random starting phase at each polarization switch will cause a reduction in the force compared with these simulations. As the dark-state population builds up at a rate determined by the natural decay rate of the excited state, the polarization switches must also occur at a comparable rate (c.f. the $5/\Gamma$ optimal switching time in the above simulations). This will often be on the hundred nanosecond scale. The switching itself should occur fast enough that no significant portion of the switching cycle is taken up by the transitions, meaning single-nanosecond-scale switching. These are surmountable technical requirements, but do introduce added complexity, especially when compared with creating a constant magnetic field.

For comparison, dark-state destabilization by a skewed magnetic field was also simulated for the same ${}^5S_2 \leftrightarrow {}^5P_1$ model system, with π-polarized BCF fields. With the Rabi frequency optimized for $|m|$=1 transitions, such that two of the three available transitions were being driven with optimal Rabi frequency, the peak force over a considerable range of magnetic field parameters is found to be $24\hbar k\Gamma/2$. Unlike the polarization switching scheme, no fine-tuning of phases or timing is required. At least in this system, magnetic field remixing is the better

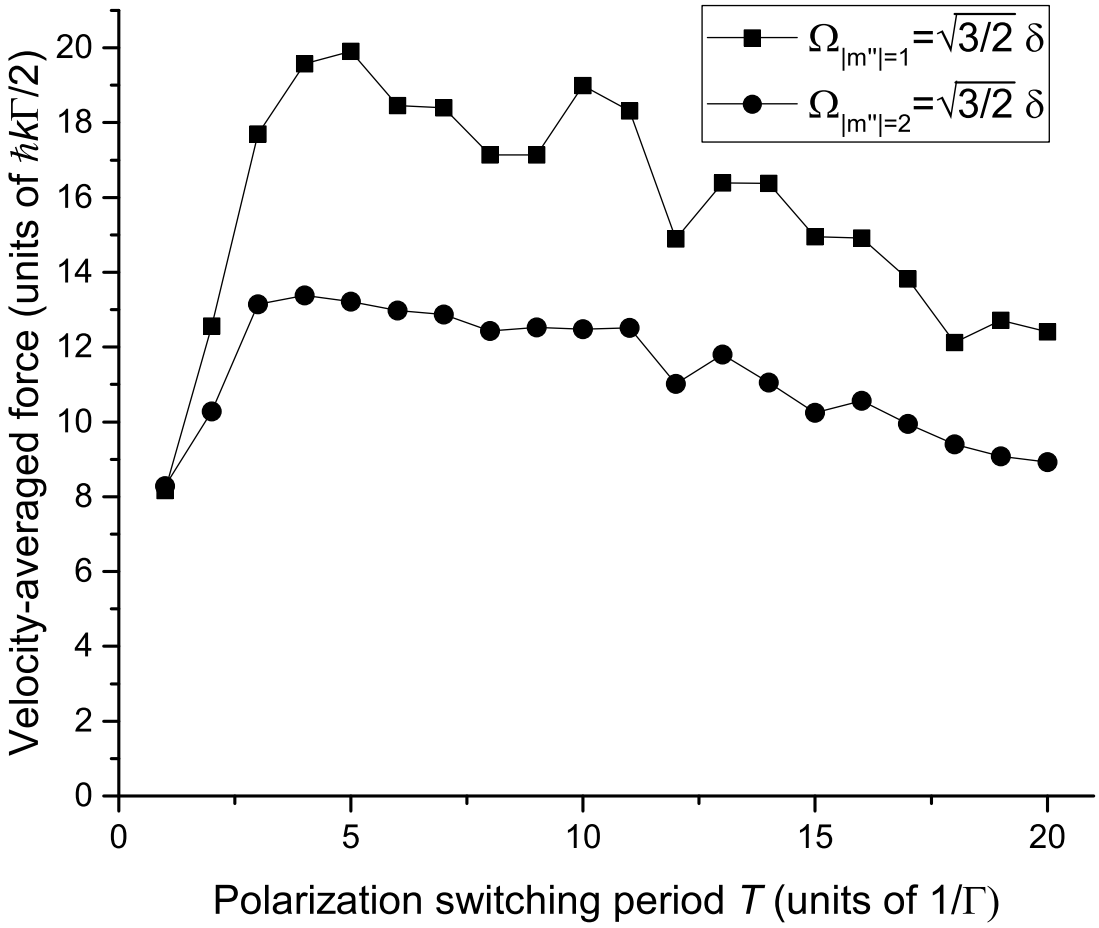

Fig. 4.8: Bichromatic force for a ${}^5S_2 \leftrightarrow {}^5P_1$ transition as a function of the switching period T between σ^+ and σ^- polarization states. The Rabi frequency is set to its optimum value for the $|m''| = 1 \leftrightarrow m' = 0$ transition or for the $|m''| = 2 \leftrightarrow |m'| = 1$ transition, giving the two curves above, and the bichromatic detuning is $100\,\Gamma$ throughout. This figure is reproduced from Ref. [49].

choice, but if a particular application cannot tolerate external magnetic fields, polarization switching remains a viable alternative.

4.3 Direct Repumping

Sections 4.1 and 4.2 deal with multilevel effects within collections of states that are all near-resonant with the same optical field. It is often the case, in contrast, that radiative decay gradually populates distant states, requiring a repumping scheme with additional optical fields to recover the population from these states. One repumping scheme is to simply add a repumping optical field tuned to the same transition that populated the distant state initially. A 1+1 system with a distant state was simulated to evaluate this scheme, where a continuous repumping laser field was used to transfer population from the dark state to the same excited state used by the cycling BCF transition. Because radiative decay is incoherent, the effects of multiple dark states are expected to be qualitatively similar to those simulated here for a single dark state, apart from the obvious impact of increased level degeneracies.

Setting the decay branching such that 5% of decays are to the distant state and simulating the reponse of the system to various BCF detunings and repump Rabi frequencies reveals a δ-dependent optimal repump Rabi frequency (Fig. 4.9). This is in contrast with repumping requirements for the incoherent radiative force, for which the force saturates with increased repump power. The difference can be

attributed primarily to interruption of the coherent BCF cycling by the repump laser which builds up competing coherence on the repump transition as the repump power increases.

As in the case of the magnetic remixing discussed in Sec. 4.2.1, this direct repumping scheme involves returning population to the BCF cycle by coherently coupling back to one of the BCF states. Also as in that case, the optimal coupling strength is proportional to $\sqrt{\delta}$. For the data in Fig. 4.9, least-squares fitting gives the optimal repump Rabi frequency for a 5% dark-state decay fraction as

$$\Omega_{ed}^{\mathrm{opt}} = 0.536(14)\sqrt{\delta\Gamma}. \tag{4.8}$$

Comparing the BCF with repumping at optimal parameters to the two-level BCF, the velocity range remains unchanged, but the peak force is reduced. For the case of 5% decay to a distant state, the force is reduced to approximately 50% of the two-level force. Further simulations were carried out to compare the reduction in force over a range of decay branching ratios, with the bichromatic detuning and overall excited-state decay rate remaining fixed. As seen in Fig. 4.10, as the branching fraction of spontaneous decays to the distant state increases, the peak force decreases monotonically. For very small dark-state branching fractions, the force converges to 2/3 of the two-level bichromatic force, the value expected based on steady-state population statistics. At large branching fractions, the peak force

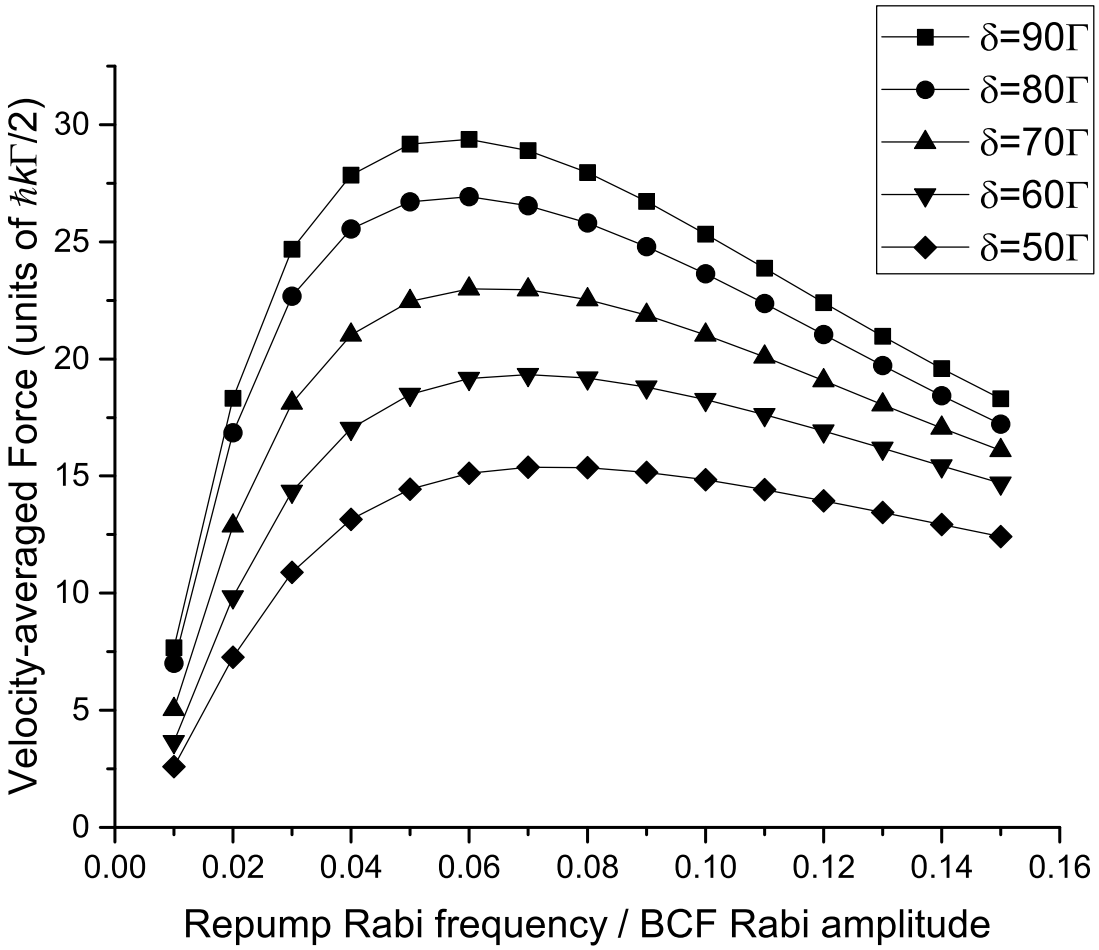

Fig. 4.9: In a 1+1 system with 5% of decays going to a distant state, the achievable force depends on the Rabi frequency for repumping out of the distant state. The force exhibits a clear optimum in the repumping Rabi frequency that depends on the bichromatic detuning δ. An optimum BCF Rabi amplitude of $\sqrt{3/2}\,\delta$ is assumed throughout. Solid lines are smooth curves to guide the eye. This figure is reproduced from Ref. [49].

decreases approximately linearly to zero. The optimal repumping Rabi frequency increases with the decay fraction to the dark state over most of the range, but begins to decline when more than 70% of the decay is to the dark state.

While BCF simultaneous with direct repumping can still provide a force in excess of the radiative force, that force is significantly reduced in comparison to the two-level BCF. The repump intensity must be fairly high and within an optimum range, as well. Overall, direct repumping should be avoided if possible.

4.4 Indirect Repumping

If the level structure allows it, a possibility for avoiding the deleterius effects of direct repumping on the BCF coherent cycling is to repump lost population into a different excited state that can decay into the BCF cycling transition. This allows for incoherent reintroduction of population, which cannot interrupt the cycling of the population that is still in the BCF states.

To simulate this arrangement, the longitudinal slowing force in a pair of two 1+1 systems was simulated with intersystem coupling only by spontaneous decay terms. The two states of the primary system are coupled with a BCF optical field, and the two states of the secondary system are coupled with a monochromatic cw optical field (Fig. 4.11).

The monochromatic cw Rabi frequency for repumping is introduced in two different forms, longitudinal and transverse. The longitudinal Rabi frequency

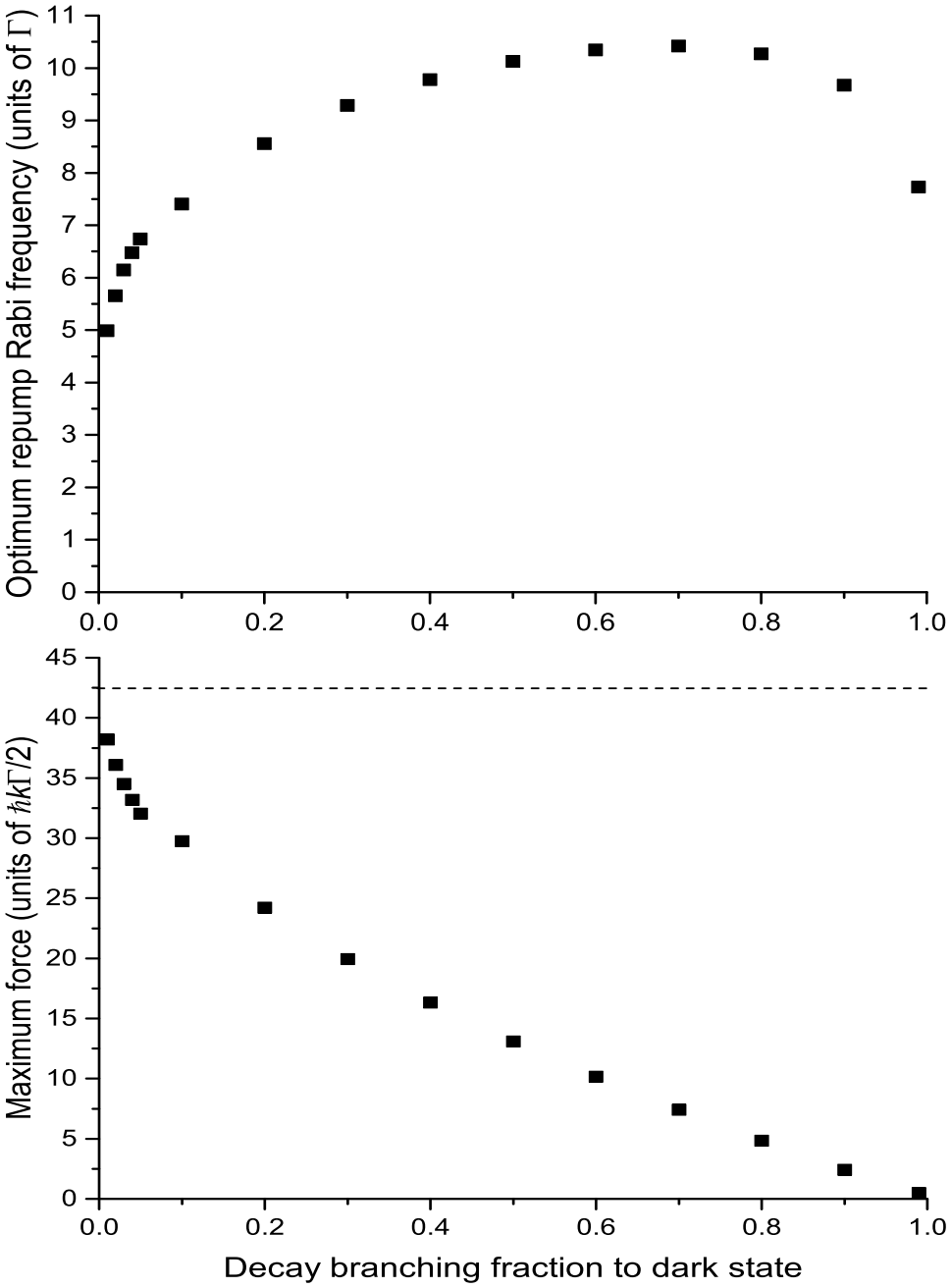

Fig. 4.10: At a fixed bichromatic detuning of $100\,\Gamma$, the optimal repump Rabi frequency (top) and the optimized force on molecules with near-zero velocities (bottom) depend on the branching ratio of excited state decays to a distant dark state. For very small decay rates to the dark state, the force is reduced from the two-level case only by a statistical factor equal to the participating state fraction (dashed line, bottom). This figure is reproduced from Ref. [49].

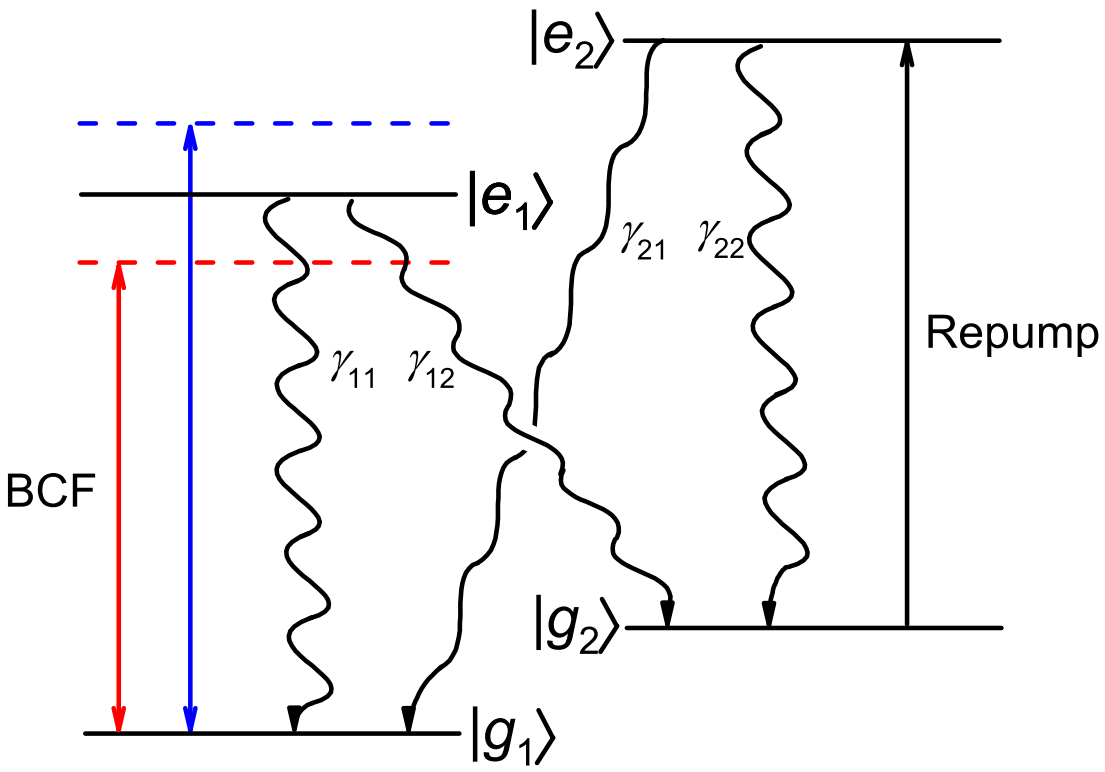

Fig. 4.11: A schematic diagram of BCF simultaneous with indirect repumping, with the labeling of the four states and four spontaneous decay pathways shown.

arises from an optical field with the same propagation direction as the BCF optical fields. Thus, its spatial dependence is necessary to model the effect on a target system moving at different velocities along that line. The longitudinal co-rotating repump Rabi frequency is therefore taken to be

$$\Omega_{MCR}^{\parallel} = \Omega_{MCR}^{0} e^{ik_{MCR}z}, \tag{4.9}$$

where z is the position and MCR is an abbreviation of monochromatic repump.

A test system with parameters $k_{MCR}/k = 1.09$, $\gamma_{11} = 0.96\,\Gamma$, $\gamma_{12} = 0.04\,\Gamma$, $\gamma_{21} = 0.98\,\Gamma$, and $\gamma_{22} = 0.02\,\Gamma$, for an arbitrary total excited state decay rate Γ which is taken to be equal between the two excited states, was simulated with a BCF field of $\delta = 50\,\Gamma$ and $\Omega^0 = \sqrt{3/2}\,\delta$ for a range of velocities and repump Rabi frequencies. The results (Fig. 4.12) showed a saturating behavior, as one might expect from a monochromatic repump, with the force at zero velocity increasing monotonically as the repump Rabi frequency increased.

However, the shape of the force profiles is not constant, having a much narrower width at lower repump Rabi frequencies. This can be explained by the Doppler shift between the repump field and the moving target, which shifts the repump off of resonance. In a simple model, the overall force can be estimated as

$$F(v) = F_{BCF}(v)\frac{T_{BCF}(v)}{T_{BCF}(v) + T_{MCR}(v)} \tag{4.10}$$

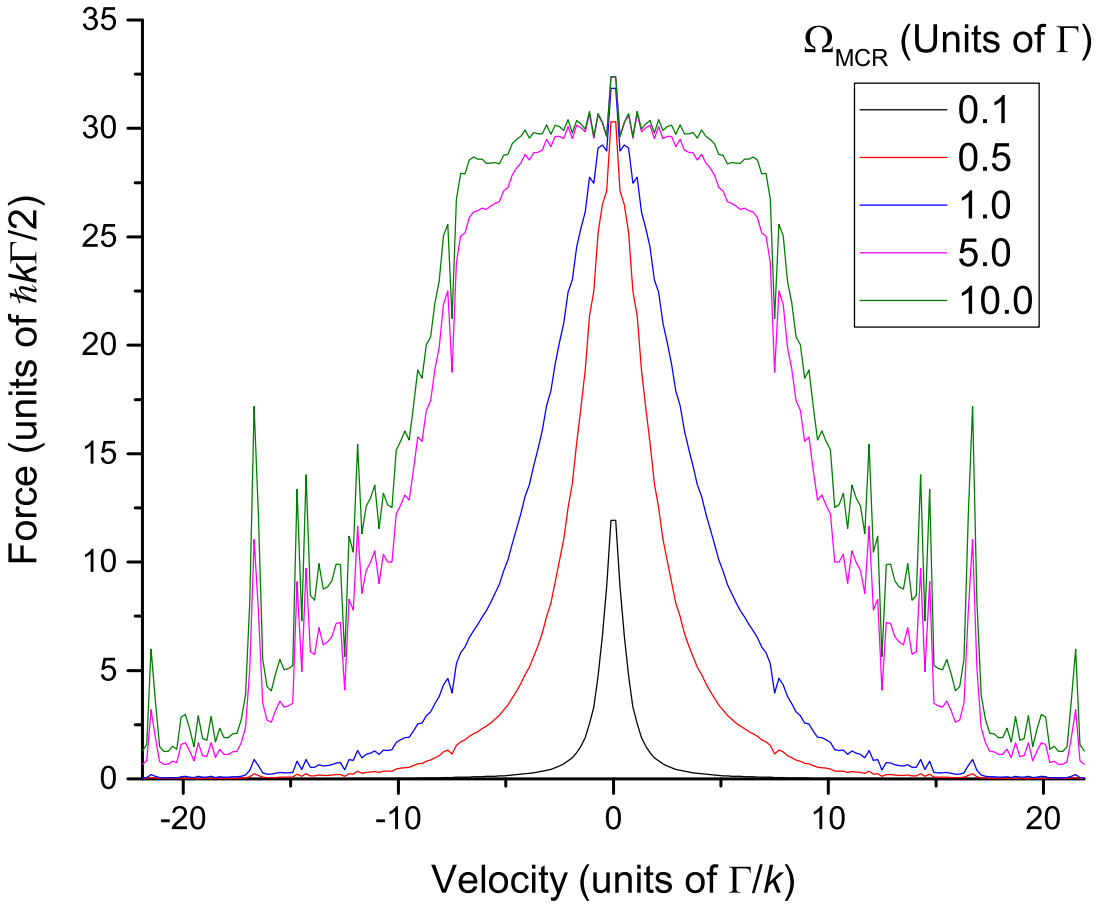

Fig. 4.12: Indirect longitudinal repumping simultaneous with BCF shows saturating behavior in the force as the repump Rabi frequency is increased. At greater speeds, the force saturates at higher repump Rabi frequencies, due to Doppler shifting.

where T_{BCF} is the average cycling time on the BCF transition before decay to the repump ground state and T_{MCR} is the average cycling time of the repump transition before decay to the BCF ground state. In short, the force is reduced only by the proportion of time spent in the repump transition, and not by any coherent effects. The two cycling times can be estimated as

$$\begin{aligned} T_{BCF} &= \left(\bar{\rho}_{ee}^{BCF}\gamma_{12}\right)^{-1} \\ T_{MCR} &= \left(\bar{\rho}_{ee}^{MCR}\gamma_{21}\right)^{-1} \end{aligned} \tag{4.11}$$

where the two $\bar{\rho}_{ee}$ are the average excited-state fractions in the isolated BCF and MCR cases.

In a two-level system driven by BCF optical fields, with $\Omega \gg \gamma$, the average excited state population in quasiequilibrium is approximately 41% [46].

For an isolated two-level system, with an excited state with decay rate Γ driven with a cw monochromatic optical field of constant real Rabi frequency Ω_{MCR}^{0} and detuned from the transition frequency by Δ, the steady-state excited state population is

$$\rho_{ee} = \frac{{\Omega_{MCR}^{0}}^2}{\Gamma^2 + 4\Delta^2 + 2{\Omega_{MCR}^{0}}^2}, \tag{4.12}$$

as can be seen by setting the each of the time-derivatives in Eq. 2.21 to zero and assuming a constant Ω_{eg}. In the situation that the driving field is on resonance for a stationary target, due to the Doppler offset the detuning from resonance as

seen by a moving target will be $\Delta = k_{MCR}v$.

Putting this together allows us to make an estimate, starting from the force in closed-system BCF, to the force when an indirect repump is added to open-system BCF. Using the same parameters in this estimation scheme that were used for the earlier indirect repump simulations, we can see that the estimation scheme exactly predicts the simulation results, including the softening of the force profile plateau due to Doppler shifts of the repump (Fig. 4.13). This verifies that the assertion that the indirect repump scheme avoids the deleterious coherent effects of the direct repump scheme is accurate, as this estimation scheme neglected any such effects. This also allows for quick evaluation of particular indirect repump schemes in the longitudinal configuration in actual systems. The obvious drawback is that to obtain a broad velocity profile, high repumping irradiance is needed to power-broaden the transition over the Doppler profile.

Fortunately, the issue of the narrowing of the force profiles due to Doppler shifts can be resolved more easily by using a transverse repumping beam perpendicular to the BCF beam axis. In this arrangement, there is no Doppler shift of the repump frequency from the velocity component along the direction of the BCF beams. For applications to longitudinal slowing, the BCF beam axis is the fast axis, and the transverse Doppler shift is ordinarily negligible. In this case,

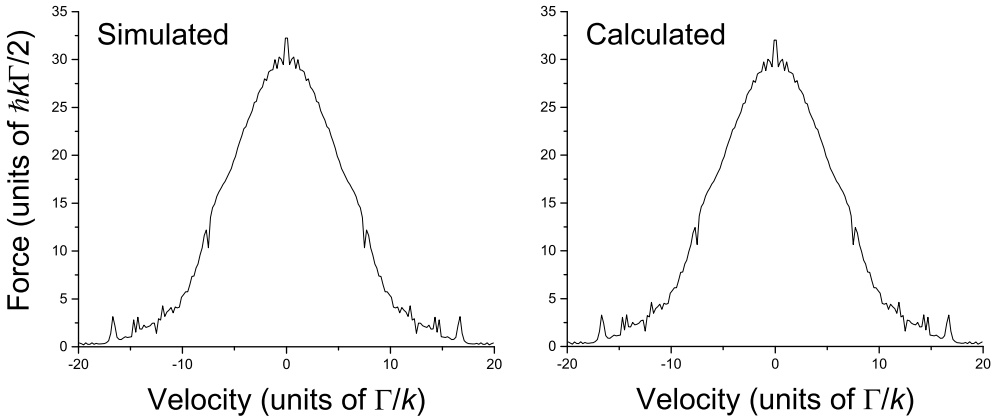

Fig. 4.13: Comparison of force profiles for indirect repumping during BCF, using a full numerical simulation (left) and calculated using Eqs. 4.10-4.12 (right), at repump Rabi frequency $\Omega^0_{MCR} = 2\,\Gamma$. In each case, the bichromatic detuning was set to $\delta = 50\,\Gamma$ and the BCF Rabi frequency amplitude to $\Omega^0 = \sqrt{3/2}\,\delta$. The calculated profile matches the simulation nearly exactly.

the repump Rabi frequency is simply

$$\Omega^{\perp}_{MCR} = \Omega^0_{MCR}. \tag{4.13}$$

Simulating the same system as in the earlier longitudinal repump scenario, but with a transverse repump, shows the expected lack of different velocity dependence at different repump intensities (Fig. 4.14). As the velocity term in Eq. 4.12 is always nearly zero, there only remains a saturation in repump intensity. The maximum attainable force when the repump transition is saturated can be very near to the force for a closed BCF transition, depending on the relative strengths of the decay pathways. For the model system discussed in this section, the force at

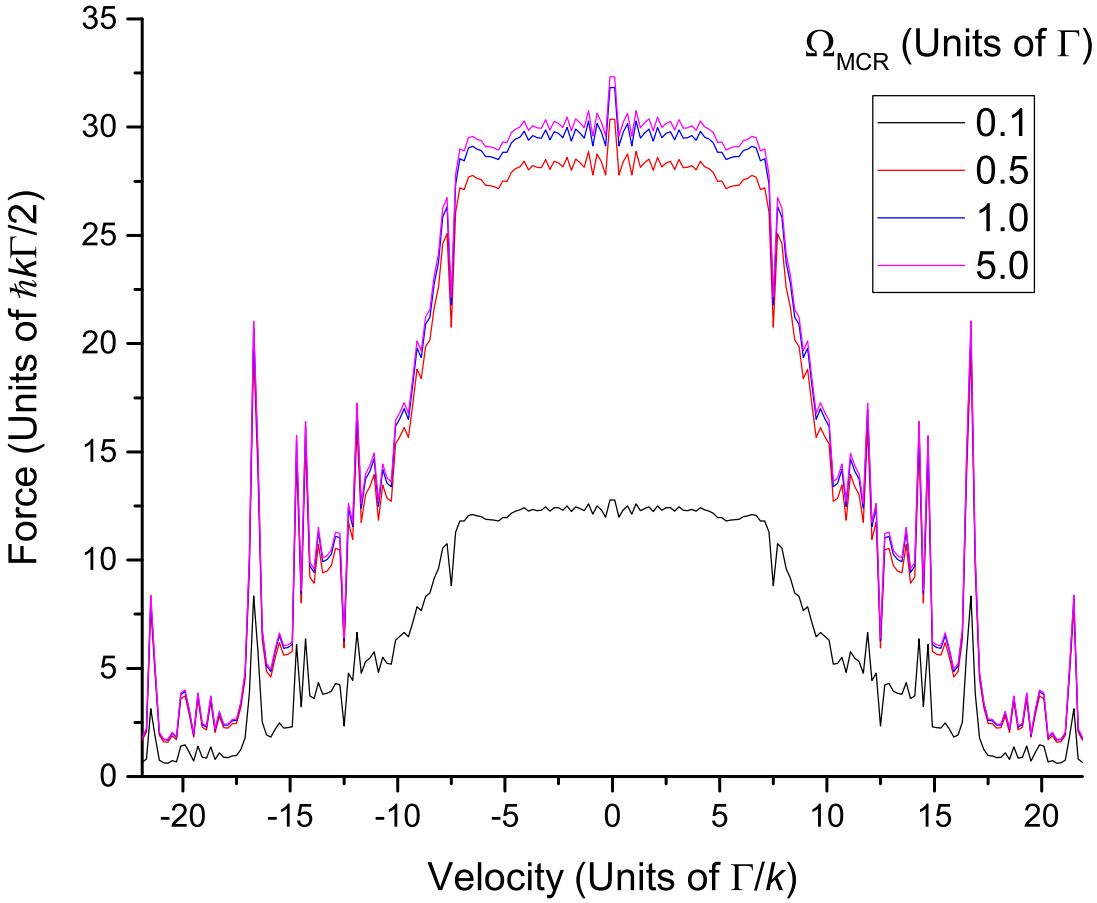

Fig. 4.14: Indirect transverse repumping simultaneous with BCF shows saturating behavior in the force as the repump Rabi frequency is increased. The saturation scale with repump Rabi frequency is velocity-independent, in contrast with indirect longitudinal repumping.

large repump Rabi frequencies is 96.8% of that for the closed two-level BCF. This is clearly a preferred method compared both with longitudinal indirect repumping and direct repumping, should it be possible for the system in question. As the large magnitude of the bichromatic force allows for a given change in velocity in a short interaction region, it is feasible to illuminate the entire interaction region with a sufficiently intense transverse repump beam.

It should be kept in mind that one of the key advantages of the bichromatic force is the rapid stimulated transition rate, which allows a much larger total momentum transfer than incoherent forces if the available interaction time is limited. Thus for weak out-of-system decay channels, it will often become possible to omit a repumping scheme altogether and allow the loss, as the time it would take to accumulate a large population in the distant state may be long compared to the needed interaction time. Nevertheless, for the case of rapid decay to dark states the need for repumping will be unavoidable.

Chapter 5

Molecular Systems

With the insight into the use of BCF in multilevel systems gained by examining simple model systems, as discussed in Chapter 4, its application to specific molecular systems can be examined. In this chapter, the use of BCF on calcium monofluoride and strontium monohydroxide is discussed.

5.1 Calcium Monofluoride

Calcium monofluoride has become a molecule of particular interest in the area of optical molecular slowing [7,8,52]. Being a diatomic molecule, CaF has vibrational and rotational states due to relative nuclear motion, in addition to all of its electronic states. The Franck-Condon factor (FCF), which measures vibrational wave-function overlap and can be used to estimate vibrational decay branching, has a remarkably high value of 0.999 for the (0-0) vibrational line between the $X\,^2\Sigma^+$ ground electronic state and the $B\,^2\Sigma^+$ excited electronic state [53]. This remarkably high FCF, along with the convenient 531 nm transition wavelength [54], which is very close to the widely-used second harmonic output of Nd:YAG

lasers at 532 nm, makes the $B \leftrightarrow X$ (0-0) line an appealing choice for a slowing transition.

The rotational quantum number N is restricted by dipole selection rules to change by exactly one during a transition [55]. If the $P_{11}(1.5)/^{P}Q_{12}(0.5)$ branch is driven, which has N''=1 and N'=0, spontaneous decay can only repopulate N''=1 levels. This branch is rotationally closed, removing a major avenue for out-of-system decay from the equation.

The $A\,^2\Pi$ state lies between the B and X states in energy, so that population in the B state may decay to the A state rather than to X. Decay rates to the different electronic states can be calculated from the Einstein A coefficients, which follow

$$A_{ij} = \frac{16\pi^3 \left|d_{ij}\right|^2}{3h\lambda^3\epsilon_0}, \tag{5.1}$$

which is proportional to $\nu_{ij}^3 \left|d_{ij}\right|^2$. Comparing $B \rightarrow X$ and $B \rightarrow A$ decays, the electronic transition dipole matrix elements have been estimated via ligand field modeling to be 1.73 ea_0 and 0.58 ea_0, respectively [56], and the transition frequencies have been measured to be 18833 cm$^-$1 and 2307 cm$^-$1, respectively [54]. These give a decay branching ratio of 4840:1, with spontaneous decays from the B state very strongly favoring the X state.

Taking these three factors (vibrational, rotational, and electronic) together, the $B \leftrightarrow X$ (0-0) $P_{11}(1.5)/^{P}Q_{12}(0.5)$ set of transitions should be about 99.8% closed. Specifically, an average of about 500 scattered photons per molecule can

occur before it ends up in a non-cycling state, if the $B \leftrightarrow X$ (0-0) $P_{11}(1.5)/{}^{P}Q_{12}(0.5)$ set of transitions is driven with no additional repumping.

Within the $v = 0$, $N = 1$ rovibrational level of the X state, for Ca isotopes of zero nuclear spin, fine and hyperfine splitting leads to twelve total quantum states at four energy levels. These level energies can be characterized by the molecular contants b, c, C, and γ. For the X state of CaF, $b = 109.184\,\mathrm{MHz}$, $c = 40.12\,\mathrm{MHz}$, $C = 2.9 \times 10^{-2}\,\mathrm{MHz}$, and $\gamma = 39.659\,\mathrm{MHz}$ [57]. Since the total electron spin is $S = 1/2$ and the total nuclear spin is $I = 1/2$, the four possible total angular momentum states are $F = (N+1), N, N, (N-1)$. The two levels for which $F = N$ will be distinguished by denoting them $F = N^{+}$ and $F = N^{-}$. The energies E_F of these four total angular momentum states, for any projection M_F, are [68]

$$\begin{aligned} E_{N+1} &= \frac{\gamma N}{2} + \frac{b}{4} + \frac{c}{4\,(2N+3)} + \frac{CN}{2}, \\ E_{N^{\pm}} &= -\frac{1}{4}\,(\gamma + b + C) \pm \frac{1}{4}\sqrt{(\gamma - C)^2(2N+1)^2 + (2b + c - 2C)(2b + c - 2\gamma)}, \\ E_{N-1} &= -\frac{\gamma(N+1)}{2} + \frac{b}{4} - \frac{c}{4(2N-1)} - \frac{C(N+1)}{2}. \end{aligned} \tag{5.2}$$

The eigenstates with $F = N$ in the X state are of mixed J character, where $\mathbf{J} = \mathbf{N} + \mathbf{S}$. In order to calculate transition strengths, it is useful to express the eigenstates as superpositions of pure J states $|(J)F\rangle$, which can be done by

introducing a mixing angle ϕ as

$$\begin{pmatrix} |F{=}1^+, M_F\rangle \\ \\ |F{=}1^-, M_F\rangle \end{pmatrix} = \begin{pmatrix} \cos\phi & \sin\phi \\ \\ -\sin\phi & \cos\phi \end{pmatrix} \begin{pmatrix} |(3/2)1, M_F\rangle \\ \\ |(1/2)1, M_F\rangle \end{pmatrix}, \tag{5.3}$$

where ϕ is given by [68]

$$\phi = \tan^{-1}\left(\frac{(2b+c-2C)\sqrt{N(N+1)}}{N(2N+1)\gamma - \frac{2N+3}{2}b - \frac{1}{2}c - N(2N+3)C - 2(2N+1)E_{N^-}}\right). \tag{5.4}$$

This gives a value for ϕ of 41.17° for $F = N = 1$ in the CaF X state, using the molecular constants previously stated.

In the $N'{=}0$ B state, the only possible value of J is 1/2. The hyperfine splitting of this state is small and has not been observed, so it is assumed for the purposes of this dissertation to be zero. The transition dipole matrix elements between the $N''{=}1$ X states and $N'{=}0$ B states, which will determine the strength with which they are coupled through an optical field, can be determined by expressing each in terms of Hund's case (a_β) basis states $|\Lambda, S, \Sigma, \Omega, J, I, F, M_F\rangle$. The transition dipole matrix element between two such states $|f\rangle$ and $|i\rangle$ for a

given polarization $p = 0, \pm 1$ is given by [58]

$$\begin{aligned}\langle f|\, T_p^{(1)}(\mathbf{d})\, |i\rangle &= (-1)^{F'-M'_F} \begin{pmatrix} F' & 1 & F \\ -M'_F & p & M_F \end{pmatrix} (-1)^{F+J'+I+1} \sqrt{(2F'+1)(2F+1)} \\ &\times \begin{Bmatrix} J & F & I \\ F' & J' & 1 \end{Bmatrix} \sum_{q=-1}^{1} (-1)^{J'-\Omega'} \sqrt{(2J'+1)(2J+1)} \begin{pmatrix} J' & 1 & J \\ -\Omega' & q & \Omega \end{pmatrix} \\ &\times \langle \Lambda', S, \Sigma'|\, T_q^{(1)}(\mathbf{d})\, |\Lambda, S, \Sigma\rangle \end{aligned} \tag{5.5}$$

where the primed variables are those of state $|f\rangle$ and the unprimed are those of state $|i\rangle$. The case (b) basis states can be expressed as linear combinations of case (a_β) states as per Eq. 6.149 of Ref. [5]:

$$|\eta, \Lambda; N, S, J\rangle = \sum_{\Sigma=-S}^{+S} (-1)^{J-S+\Lambda} (2N+1)^{1/2} \begin{pmatrix} J & S & N \\ \Omega & -\Sigma & -\Lambda \end{pmatrix} |\eta, \Lambda; S, \Sigma, J, \Omega\rangle\,. \tag{5.6}$$

Combining Eqs. 5.3 – 5.6 allows for the calculation of transition dipole matrix elements between N''=1 X states and N'=0 B states in CaF up to a common factor of $\langle \Lambda', S, \Sigma'|\, T_q^{(1)}(\mathbf{d})\, |\Lambda, S, \Sigma\rangle = 1.73\, e a_0$ [56]. Table 5.1 presents these matrix elements.

Table 5.1: Relative electric dipole matrix elements κ_{ij} for the $B \leftrightarrow X$ $P_{11}(0.5)/{}^{P}Q_{12}(1.5)$ branch in CaF, as defined in Eq. 5.7.

		F'=0	F'=1		
F''	m''_F	M'_F=0	M'_F=−1	M'_F=0	M'_F=1
	−2	0	-0.5774	0	0
	−1	0	0.4082	-0.4082	0
2	0	0	-0.2357	0.4714	-0.2357
	1	0	0	-0.4082	0.4082
	2	0	0	0	-0.5774
	−1	-0.5743	-0.0421	-0.0421	0
1^+	0	0.5743	0.0421	0	-0.0421
	1	-0.5743	0	0.0421	0.0421
	−1	0.0595	-0.4061	-0.4061	0
1^-	0	-0.0595	0.4061	0	-0.4061
	1	0.0595	0	0.4061	0.4061
0	0	0	0.3333	0.3333	0.3333

We now define the "relative dipole matrix element" κ_{ij} as

$$\kappa_{ij} = \frac{\sum_p \langle i| T_p^{(1)}(\mathbf{d}) |j\rangle}{\langle \Lambda', S, \Sigma' = 1/2| T_0^{(1)}(\mathbf{d}) |\Lambda, S, \Sigma = 1/2\rangle} \tag{5.7}$$

for convenience. Combining Eqs. 2.10 and 5.7 with the irradiance of a monochromatic plane wave gives practical units for the Rabi amplitude of one of these transitions at a particular irradiance I, measured in W/cm^2:

$$\Omega_{ij}^0 = \kappa_{ij}\sqrt{I}\,(2\pi \times 60\,\mathrm{MHz})\,. \tag{5.8}$$

All of this together allows for a complete picture of the CaF $B \leftrightarrow X$ (0-0)

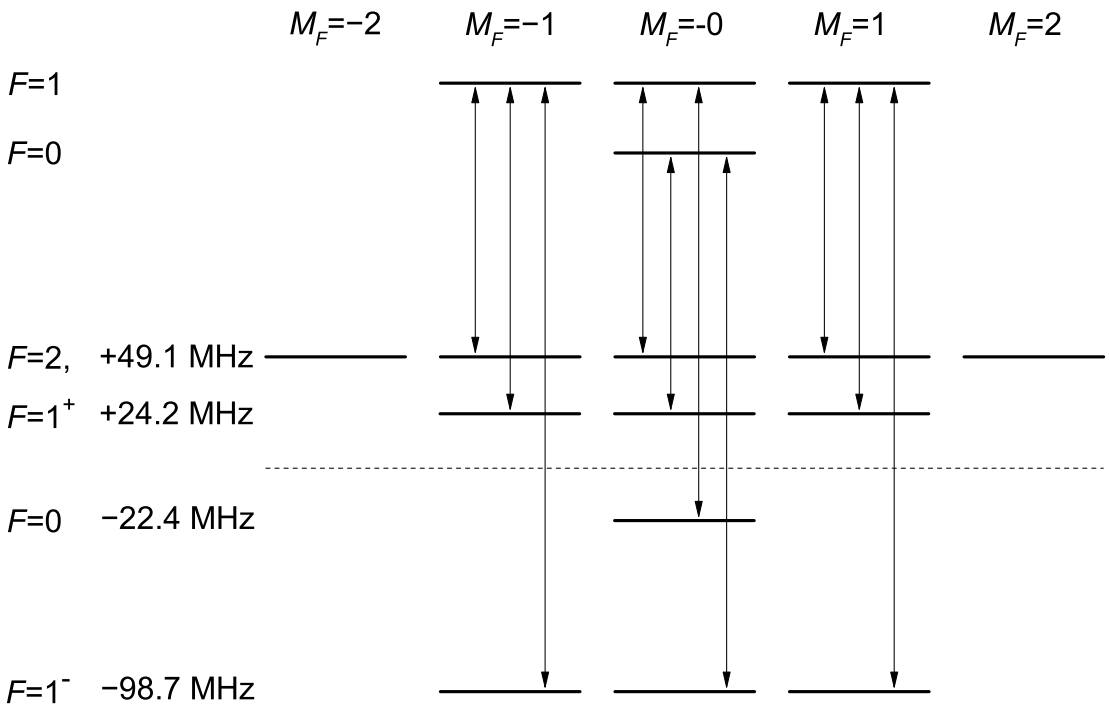

Fig. 5.1: The $B \leftrightarrow X$ $P_{11}(1.5)/^{P}Q_{12}(0.5)$ system in CaF, showing zero-field energy spacings. The hyperfine splitting of the B levels is taken to be negligible compared to the X state. The allowed transitions for π-polarized light are indicated. This figure is adapted from Ref. [49].

$P_{11}(1.5)/^{P}Q_{12}(0.5)$ transitions as a 12+4 multi-level system (Fig. 5.1). The four F'' levels are spaced such that any small-detuning BCF would be weak, and to properly enter the large-detuning regime, all four levels must be addressed. As such, a bichromatic detuning greater than 150 MHz will be required to produce a significant bichromatic force using these transitions in CaF. The B state natural lifetime has been measured to be 25.1±4 ns [59], so in terms of the excited state decay rate, $\delta > 24\Gamma$ is needed. When the system is driven with π-polarized light, the two $|M_F''| = 2$ states are dark, and to avoid optical pumping, destabilization is required as discussed in Sec. 4.2. In this case, all of the involved states have $\Lambda = 0$, so the $\hat{L}$ term of Eq. 4.4 is identically zero. The matrix elements of the $\hat{S}$ term between two case (b) states are given by Eq. (8.183) of Ref. [5], generalized to allow for a B-field not parallel to the z-axis:

$$\begin{aligned}\langle f|\,\vec{B}\cdot\hat{S}\,|i\rangle \;=\; & (-1)^{F'+J+I+1}\sqrt{(2F'+1)(2F+1)}\begin{Bmatrix} F & J & I \\ J' & F' & 1\end{Bmatrix} \\ & \times\; (-1)^{J+N+S+1}\sqrt{(2J'+1)(2J+1)}\begin{Bmatrix} J & S & N \\ S & J' & 1\end{Bmatrix} \\ & \times\; \sqrt{(S(S+1)(2S+1)}\sum_p B_p(-1)^{F-M_F}\begin{pmatrix} F & 1 & F' \\ -M_F & p & M_F'\end{pmatrix}. \quad (5.9)\end{aligned}$$

Each of the four excited states in this system is coupled to multiple ground states by π-polarized light. In Sec. 4.1 it was shown that for such an arrangement

of states, in the large-detuning regime, the optimal total Rabi amplitude is $\sqrt{3/2}\,\delta$. For each of the four excited states, the quadrature sum of κ_{ij} over the ground states coupled to it by π-polarized light is $1/\sqrt{3}$. This means that for large detunings, the same irradiance will be optimal for the entire system. As no ground state is coupled to more than one excited state, the full 12+4 system can be separated into two 2+1 and two 3+1 subsystems (Fig. 5.2) which are only coupled to each other through incoherent radiative decay. It was seen in Sec. 4.4 that in the case of radiatively-coupled subsystems, combining independent subsystem results through population arguments works very well in predicting the behavior of the full system. As such, each of the four subsystems was simulated independantly, with no magnetic field, and the results combined with a weighting equal to the proportion of the 12 ground states that are included in each subsystem. This assumes that each of the ground states begins equally populated, and any radiative redistribution and dark-state remixing equilibrates to keep the populations in each subsystem constant.

This approach necessarily cannot model a remixing scheme, but it can give an idea of the optimal BCF carrier frequency within the transition manifold, and can estimate the expected force at a given bichromatic detuning. Three detunings in the large-detuning regime were simulated: $30\,\Gamma$, $50\,\Gamma$, and $100\,\Gamma$, each with its optimal total Rabi frequency, across a range of carrier frequencies (Fig. 5.3). The results indicate that it is best to be red-detuned from the center of mass of the

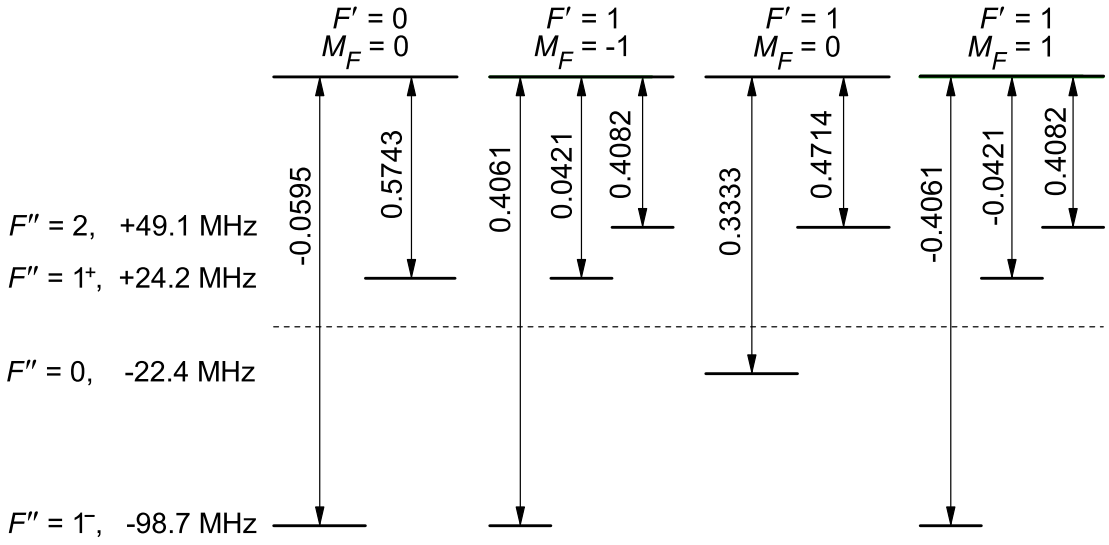

Fig. 5.2: The four subsystems defined by isolating the $\Delta M_F = 0$ transitions of the $B \leftrightarrow X$ $P_{11}(1.5)/{}^{P}Q_{12}(0.5)$ branches in CaF. Relative dipole transition matrix elements are indicated for each transition. This figure is adapted from Ref. [49].

transitions, more closely addressing the $F'' = 2$ or $F'' = 1^+$ transitions, and that the force attainable in CaF using BCF still greatly exceeds the radiative force, which also must contend with the multiplicity of the ground state. The largest recorded radiative force on CaF was achieved driving the $A \leftrightarrow X$ transition, and had an average magnitude of $0.024\,\hbar k\Gamma_A/2$ [7], about two orders of magnitude weaker than even the simulated $30\,\Gamma$ BCF results.

To find the optimal magnetic field parameters for dark state remixing, and to check the validity of the subsystem results, the full 12+4 system with BCF optical driving and a dc skewed magnetic field was simulated at the same bichromatic detunings and Rabi frequencies as the subsystem simulations. A range of carrier

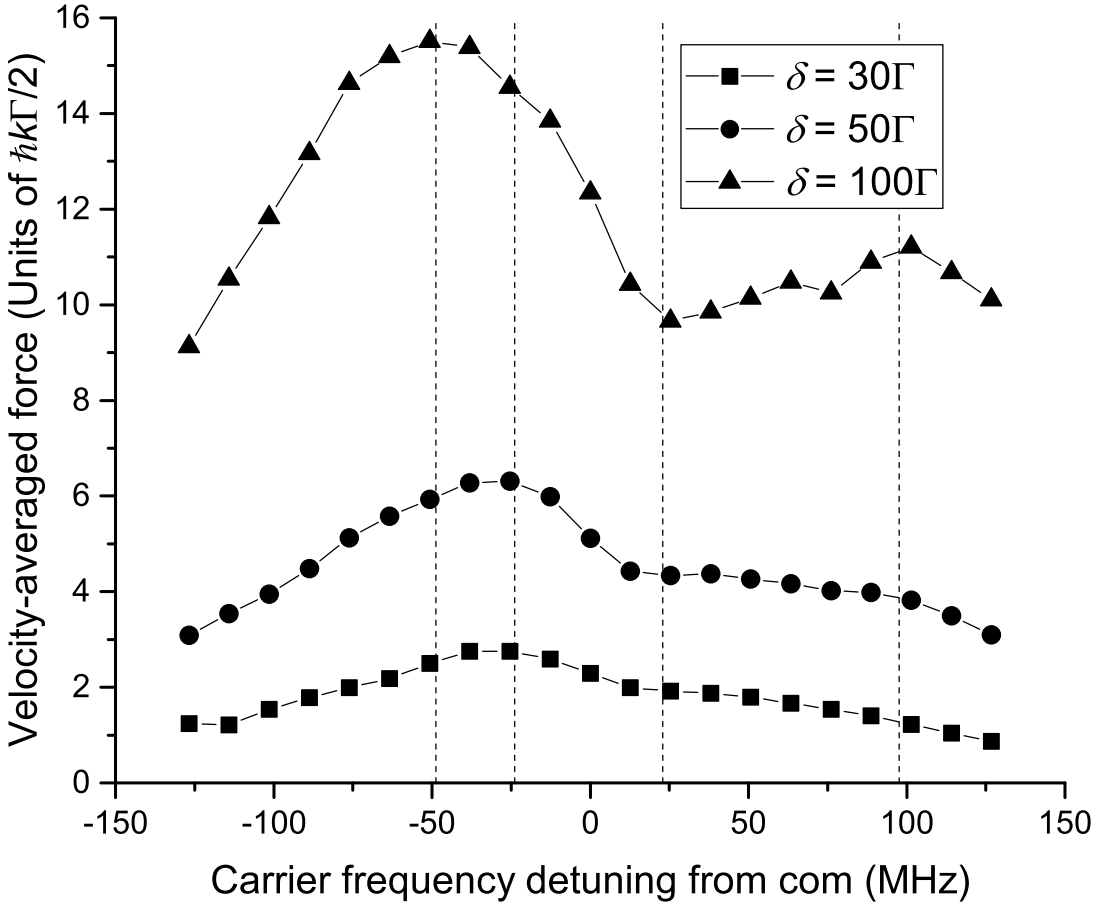

Fig. 5.3: A weighted average of the force on isolated subsystems of the $B \leftrightarrow X$ $P_{11}(1.5)/{}^{P}Q_{12}(0.5)$ branches in CaF gives an estimate for the optimal carrier frequency detuning from the transition center of mass of the system and for the peak force. Resonances are indicated with vertical dashed lines. This figure is reproduced from Ref. [49].

Table 5.2: A summary of results for two different methods of estimating the BCF for π-polarized light in the sixteen-level $B \leftrightarrow X$ $P_{11}(0.5)/^{P}Q_{12}(1.5)$ system in CaF, assuming no repumping. The methods are (a) a weighted subsystem-based multilevel simulation, and (b) a full 16-level simulation of the complete system, including dark-state remixing by a dc magnetic field. In the final row of the table, we consider the fraction of molecules remaining after slowing by 60 m/s, taking into account decays into distant dark states.

	δ=30Γ		δ=50Γ		δ=100Γ	
	(a)	(b)	(a)	(b)	(a)	(b)
Irradiance (W/cm^2)	45.2	45.2	125.6	125.6	503	503
Carrier detuning from c.o.m. (MHz)	-32	-38	-30	-38	-47	-38
Magnetic field magnitude (Gauss)	—	29.2	—	29.4	—	37.1
Magnetic field angle	—	71°	—	61°	—	66°
Force near zero velocity ($\hbar k\Gamma/2$)	2.8	2.6	6.3	5.8	15.5	14.2
Velocity range (m/s)	110	120	130	170	190	250
Average excited fraction	0.23	0.18	0.21	0.15	0.18	0.14
Time to slow by 60 m/s (μs)	84	91	38	41	15	17
Fully-slowed population fraction	0.21	0.27	0.53	0.61	0.80	0.83

frequencies and magnetic field magnitudes and angles were simulated at each detuning, and the optimal set of parameters within the ranges was determined from these simulations as summarized in Table 5.2. The force profiles produced at the optimal parameters are shown in Fig. 5.4. The subsystem analysis predicts force magnitudes within 10% of those predicted by the full simulations at optimal parameters, demonstrating its usefulness for estimating the BCF magnitude with less computational time than full simulations.

The average excited-state fraction was recorded during each simulation, and the average over the high-force velocity plateau was calculated at the optimal parameters for each of the three simulated bichromatic detunings. At $\delta = 30\,\Gamma$, the average excited-state fraction was about P_e=1/6. The excited-state fraction

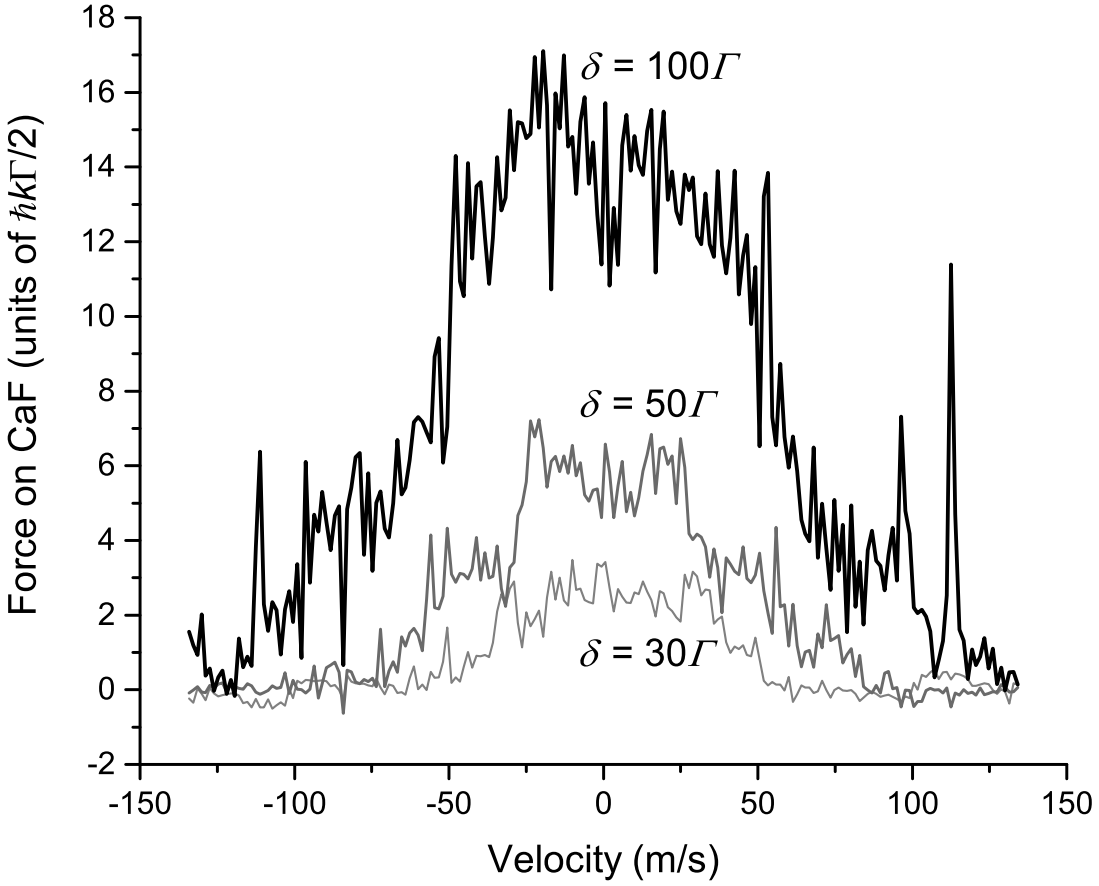

Fig. 5.4: Simulations of the bichromatic force for the sixteen-level $B \leftrightarrow X$ $P_{11}(0.5)/^{P}Q_{12}(1.5)$ system in CaF, with dark-state remixing by a dc magnetic field. These forces far exceed the radiative force of $\sim$0.024 $\hbar k\Gamma/2$ realized in Ref. [7] for the similar $A \leftrightarrow X$ system. The strength and velocity range of the force increase with the bichromatic detuning throughout the range of detunings simulated. This figure is reproduced from Ref. [49].

converged to 1/7 as the detuning increased, a value which has been previously predicted by statistical arguments [60]. The time available prior to out-of-system decay depends on this excited-state fraction, being equal to $\tau_B/(0.002P_e)$, where τ_B is the natural lifetime of the B state and 0.002 is the estimated out-of-system branching fraction. The out-of-system loss time is therefore about 75 μs.

The SrF MOT produced by the DeMille group [10] was loaded from a buffer-gas-cooled beam, and slowing of the SrF by 60 m/s was sufficient to load the trap. Using the bichromatic force at $\delta = 30\,\Gamma$, these simulations predict that 27% of illuminated CaF molecules with N''=1 would be slowed by 60 m/s before being lost to distant dark states. This fraction increases with higher detuning, and is 83% at $\delta = 100\,\Gamma$. These results indicate that as long as the required laser irradiance is available, a repump-free optical decelerator is feasible for CaF and other molecules with similar near-cycling transitions.

5.2 Strontium Monohydroxide

One such molecule is the linear triatomic molecule strontium monohydroxide, SrOH. It has been the subject of intense recent work by the Doyle group [61,62], with a view towards direct laser slowing and trapping. SrOH is isoelectronic to CaF [63], but as a linear triatomic molecule it has three vibrational modes: a Sr-O stretching mode, a bending mode, and an O-H stretching mode, so the full vibrational state is written as $(\nu_1\nu_2^\ell\nu_3)$ incorporating the three mode numbers,

respectively, and a bending mode angular momentum number ℓ (out-of-phase bending vibrations in different planes will produce rotation around the molecular axis, which carries angular momentum). These additional modes present a number of additional decay pathways from a given excited state, leading generally to less-closed transitions.

Like in CaF, the $\tilde{X}\,^2\Sigma^+$ state can be excited to the $\tilde{A}\,^2\Pi$ state or to the $\tilde{B}\,^2\Sigma^+$ state. The Franck-Condon factors between the (000) vibrational states of $\tilde{A}$ or $\tilde{B}$, and the various vibrational states of $\tilde{X}$, can be calculated via the **GF** matrix formalism and Sharp-Rosenstock approach [64], as carried out by Ivan Kozyryev for SrOH [65] (Table 5.3). Given the FCFs for each (000)-(000) vibrational transition, less than 50 spontaneous decays can occur before a molecule is lost out of a (000)-(000) cycle. Even given the strength of BCF, this would almost certainly not be sufficient time to achieve the desired change in velocity. Fortunately, as seen in Sec. 4.4, indirect repumping can recover population from distant dark states without negatively affecting BCF cycling. If either the $\tilde{A}(000) \leftrightarrow \tilde{X}(000)$ or $\tilde{B}(000) \leftrightarrow \tilde{X}(000)$ bands is used for the primary BCF transition, the other excited (000) state can be repumped as an intermediate state that decays primarily back into the BCF cycle.

The same rotational branch ($P_{11}(1.5)/^PQ_{12}(0.5)$) can be used as in CaF in order to achieve rotational closure, with the attendant issue of optical pumping into intrasystem dark states. This can be addressed as before by the application

Table 5.3: Calculated Franck-Condon factors between vibrational states of SrOH [65].

	$\tilde{A}(000)$	$\tilde{B}(000)$
$\tilde{X}(000)$	0.9546	0.9772
$\tilde{X}(100)$	0.0430	0.0186
$\tilde{X}(200)$	0.0016	0.0022
$\tilde{X}(02^00)$	0.0008	0.0020

of a skewed dc magnetic field, whose effects on the $\tilde{X}$ and $\tilde{B}$ states are still described by Eqs. 4.4 and 5.9. In the case of the $\tilde{A}$ state, $^2\Pi_{1/2}$ states are largely insensitive to magnetic fields [66], so the effects of magnetic fields on this state will be neglected here.

The structure of the $\tilde{X}$ (000) N=1 state can be calculated from the molecular constants $\gamma = 72.706$ MHz, $b = 1.155$ MHz, and $c = 1.673$ MHz [67], noting that $b \equiv b_F - c/3$ [67,68]. This gives the energy levels shown in Fig. 5.5. Using the same methods to analyze J-mixing as in CaF, the mixing angle is determined to be less than half a degree, and the pure-J states can be taken to be the eigenstates of the system.

The relative dipole transition matrix elements for the $P_{11}(1.5)/^PQ_{12}(0.5)$ branches of $\tilde{B} \leftrightarrow \tilde{X}$ are calculated similarly to CaF, though due to the assumption of pure J states, the results are exact in this case (Table 5.4). The $\tilde{A}$, J=$1/2^+$ state is a state of positive parity and can be written in terms of case (a_β) states

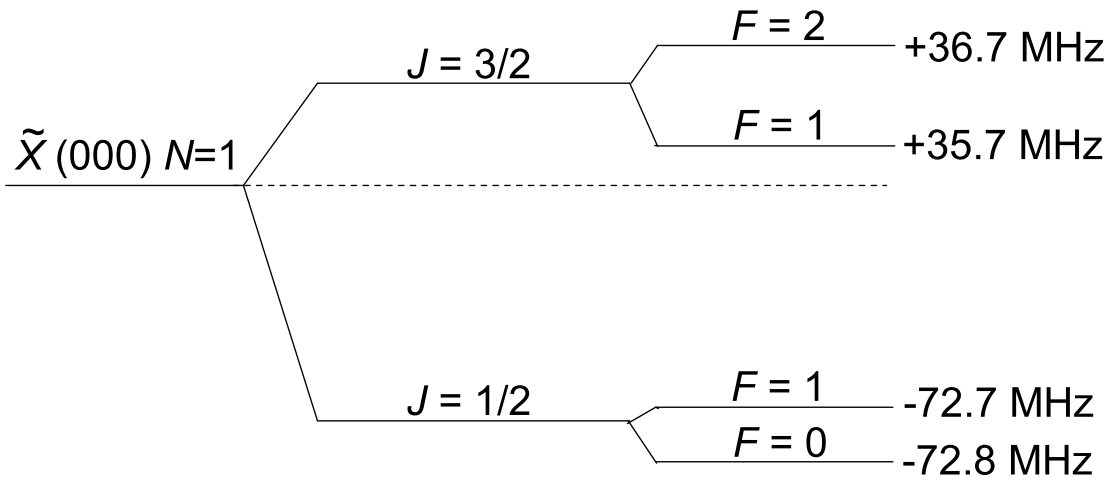

Fig. 5.5: The energy levels due to spin-orbit and hyperfine splitting of the $N = 1$ states of $\tilde{X}$ in SrOH (splittings not shown to scale). The spin-orbit splitting of 107 MHz is much larger than the hyperfine splittings of 1 and 0.1 MHz.

$|\Lambda, S, \Sigma, \Omega, J\rangle$ as

$$\frac{1}{\sqrt{2}}\left|1, \frac{1}{2}, -\frac{1}{2}, \frac{1}{2}, \frac{1}{2}\right\rangle + \frac{1}{\sqrt{2}}\left|-1, \frac{1}{2}, \frac{1}{2}, \frac{1}{2}, -\frac{1}{2}, \frac{1}{2}\right\rangle. \tag{5.10}$$

From this expansion, the relative dipole transition matrix elements for the $P_{11}(1.5)/Q_{12}(0.5)$ branches of $\tilde{A} \leftrightarrow \tilde{X}$ can be calculated (Table 5.5).

The natural lifetimes of the $\tilde{A}$ and $\tilde{B}$ states are not accurately known, but are between 20 and 30 ns [63]. It is assumed here that the lifetime for each is 25 ns. Using the (000)-(000) Franck-Condon factors and the transition wavelengths, which are 688 nm for $\tilde{A} \leftrightarrow \tilde{X}$ [69] and 611 nm for $\tilde{B} \leftrightarrow \tilde{X}$ [63], formulas in practical units for the Rabi amplitudes of these transitions at a particular irradiance I,

Table 5.4: Relative electric dipole matrix elements κ_{ij} for the $\tilde{B} \leftrightarrow X$ $P_{11}(0.5)/^{P}Q_{12}(1.5)$ branch in SrOH.

		F'=0	F'=1		
F''	m''_F	M'_F=0	M'_F=−1	M'_F=0	M'_F=1
	−2	0	$-1/\sqrt{3}$	0	0
	−1	0	$1/\sqrt{6}$	$-1/\sqrt{6}$	0
2	0	0	$-\sqrt{2}/6$	$\sqrt{2}/3$	$-\sqrt{2}/6$
	1	0	0	$-1/\sqrt{6}$	$1/\sqrt{6}$
	2	0	0	0	$-1/\sqrt{3}$
	−1	$-\sqrt{2}/3$	$\sqrt{2}/6$	$\sqrt{2}/6$	0
1^+	0	$\sqrt{2}/3$	$-\sqrt{2}/6$	0	$\sqrt{2}/6$
	1	$-\sqrt{2}/3$	0	$-\sqrt{2}/6$	$-\sqrt{2}/6$
	−1	−1/3	−1/3	−1/3	0
1^-	0	1/3	1/3	0	−1/3
	1	−1/3	0	1/3	1/3
0	0	0	1/3	1/3	1/3

measured in W/cm^2, are found to be

$$\begin{aligned} \Omega^0_{\tilde{A}\leftrightarrow\tilde{X},ij} &= \kappa_{ij}\sqrt{I}\,(2\pi \times 87.0\,\mathrm{MHz})\,, \\ \Omega^0_{\tilde{B}\leftrightarrow\tilde{X},ij} &= \kappa_{ij}\sqrt{I}\,(2\pi \times 73.7\,\mathrm{MHz})\,. \end{aligned} \tag{5.11}$$

These are only rough estimates, given the uncertainities in the excited state lifetimes, but will serve for the current purposes of simulation.

Using a bichromatic detuning of $\delta = 50\,\Gamma = 318\,\mathrm{MHz}$, a subsystem-based set of simulations was carried out to estimate the optimal carrier frequency for BCF on the $P_{11}(1.5)/^{P}Q_{12}(0.5)$ branches of (000)-(000) $\tilde{A} \leftrightarrow \tilde{X}$ and $\tilde{B} \leftrightarrow \tilde{X}$.

Table 5.5: Relative electric dipole matrix elements κ_{ij} for the $\tilde{A} \leftrightarrow X$ $P_{11}(0.5)/Q_{12}(1.5)$ branch in SrOH.

		F'=0	F'=1		
F''	m''_F	M'_F=0	M'_F=−1	M'_F=0	M'_F=1
	−2	0	$-1/\sqrt{6}$	0	0
	−1	0	$\sqrt{3}/6$	$-\sqrt{3}/6$	0
2	0	0	−1/6	1/3	-1/6
	1	0	0	$-\sqrt{3}/6$	$\sqrt{3}/6$
	2	0	0	0	$-1/\sqrt{6}$
	−1	−1/3	1/6	1/6	0
1^+	0	1/3	−1/6	0	1/6
	1	−1/3	0	−1/6	−1/6
	−1	$-\sqrt{2}/3$	$-\sqrt{2}/3$	$-\sqrt{2}/3$	0
1^-	0	$\sqrt{2}/3$	$\sqrt{2}/3$	0	$-\sqrt{2}/3$
	1	$-\sqrt{2}/3$	0	$\sqrt{2}/3$	$\sqrt{2}/3$
0	0	0	$\sqrt{2}/3$	$\sqrt{2}/3$	$\sqrt{2}/3$

This detuning is well into the large-detuning regime, as compared to the 107 MHz spin-orbit spliitng of the $\tilde{X}$, N=1 state, so Ω^{tot} for each set of transitions was set to the optimal value of $\sqrt{3/2}\,\delta$. The simulation results show that BCF blue-detuned from the c.o.m. of the transitions will be more effective for $\tilde{A} \leftrightarrow \tilde{X}$ than red detuning, which makes sense because the the carrier frequency is then closer to the stronger $J'' = 1/2$ transitions. In contrast, in $\tilde{B} \leftrightarrow \tilde{X}$, the $J'' = 3/2$ transitions are stronger, and a red-detuned carrier frequency is more effective (Fig. 5.6).

Using the carrier frequencies that maximize force in the subsystem simulations, the entire 12+4 systems for both $\tilde{A} \leftrightarrow \tilde{X}$ and $\tilde{B} \leftrightarrow \tilde{X}$ were simulated

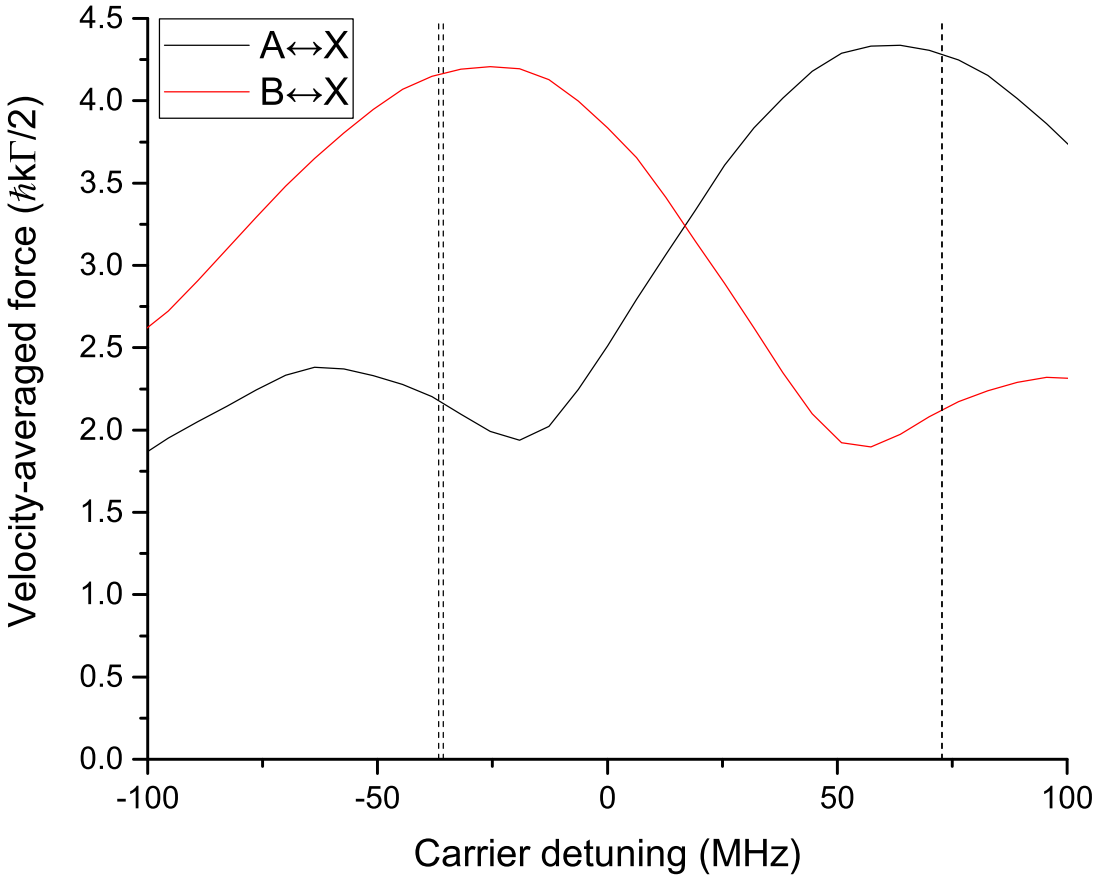

Fig. 5.6: Velocity-averaged BCF for $\delta = 50\,\Gamma$ on the $P_{11}(1.5)/Q_{12}(0.5)$ $\tilde{A} \leftrightarrow \tilde{X}$ and $P_{11}(0.5)/^{P}Q_{12}(1.5)$ $\tilde{B} \leftrightarrow \tilde{X}$ transitions, simulated using the isolated subsystem method across a range of BCF carrier detunings. The four transition frequencies are indicated with dotted lines, though the two $J'' = 1/2$ transitions are not fully resolved at this scale.

across a range of magnetic field parameters for the dark-state remixing skew dc magnetic field, using the same bichromatic detuning and Rabi frequency. The results show a BCF which does not decrease significantly as the skew angle goes to 90° (Fig. 5.7). This is due to the extremely small hyperfine splitting, which allows magnetic mixing of the hyperfine levels at moderate magnetic field strengths.

For magnetic field parameters in the region where the force is largest, the velocity profiles of the force show a by-now familiar shape (Fig. 5.8). A dip in the force near zero velocity is also evident, which appears to be a general feature of BCF profiles in this system at this detuning. This dip does not represent a significant problem, as the magnitude of the force is still significant even at the center of the dip. Using the $\tilde{A} \leftrightarrow \tilde{X}$ transitions, the average force for molecular velocities between -30 m/s and $+30$ m/s is 6.95 $\hbar k\Gamma/2$. This force would accelerate an SrOH molecule by 60 m/s in 77.9 μs. The average excited-state fraction in this velocity range is about 1/7, and using the estimated 25 ns decay lifetime, 445 spontaneous decay photons would be scattered during the acceleration. However, with a FCF of 0.9546 for the (000)-(000) band, the chance of a molecule staying in the BCF cycle for 445 decays is vanishingly small. Thus repumping is required.

If a repump from $\tilde{X}$ (100) to $\tilde{B}$ (000) is saturated, population statistics tell us that the isolated excited-state fraction in the repump transition should be the ratio of the number of excited states to the total number of states, $4/16 = 0.25$. Using Eq. 4.10, the equilibrated force with this repump is estimated to be

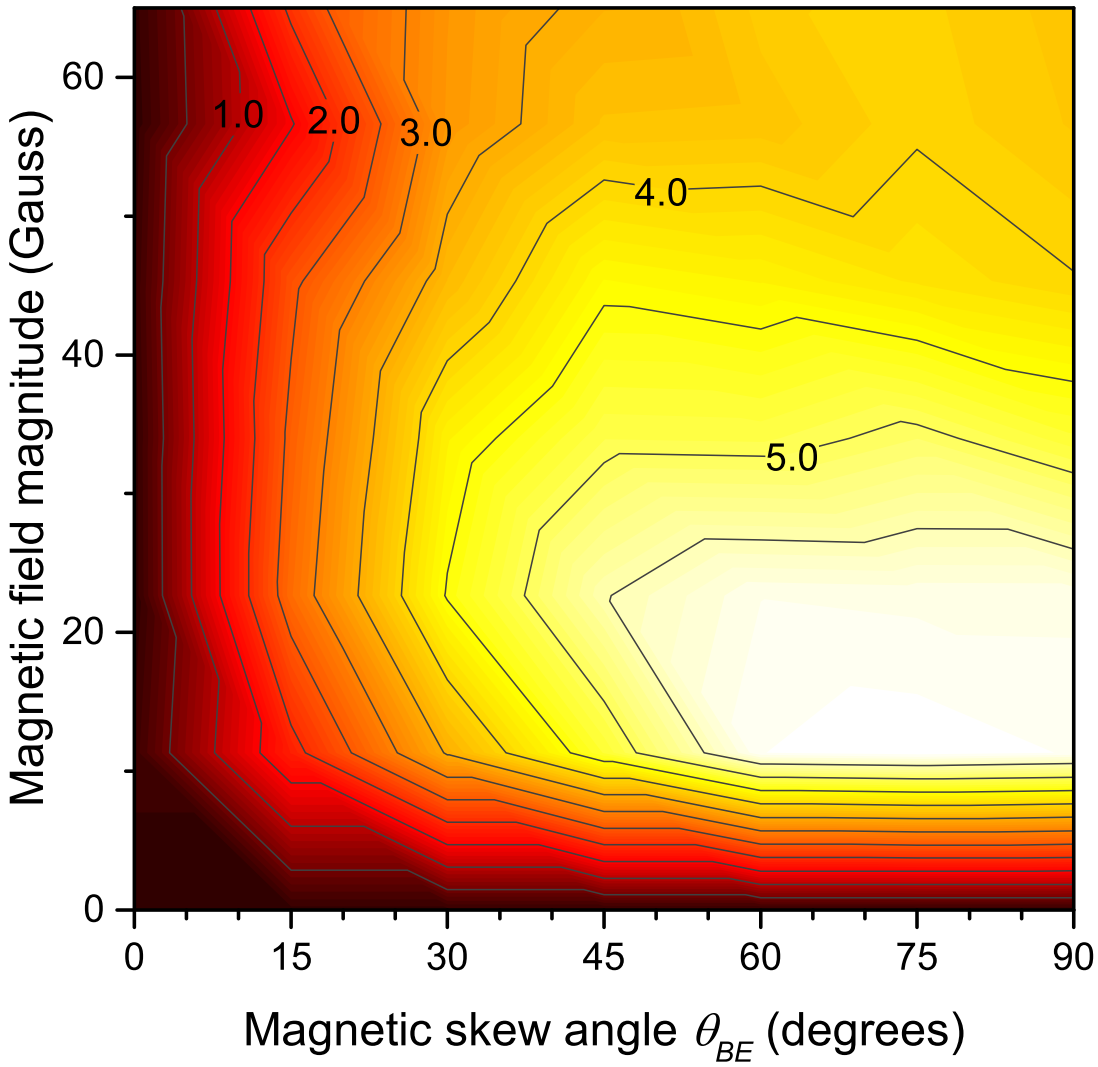

Fig. 5.7: Velocity-averaged force contours, in units of $\hbar k\Gamma/2$, from simulations of $\delta = 50\,\Gamma$ BCF in the isolated 12+4 SrOH $\tilde{A} \leftrightarrow \tilde{X}$ (000)-(000) $P_{11}(1.5)/Q_{12}(0.5)$ system across a range of magnetic field parameters.

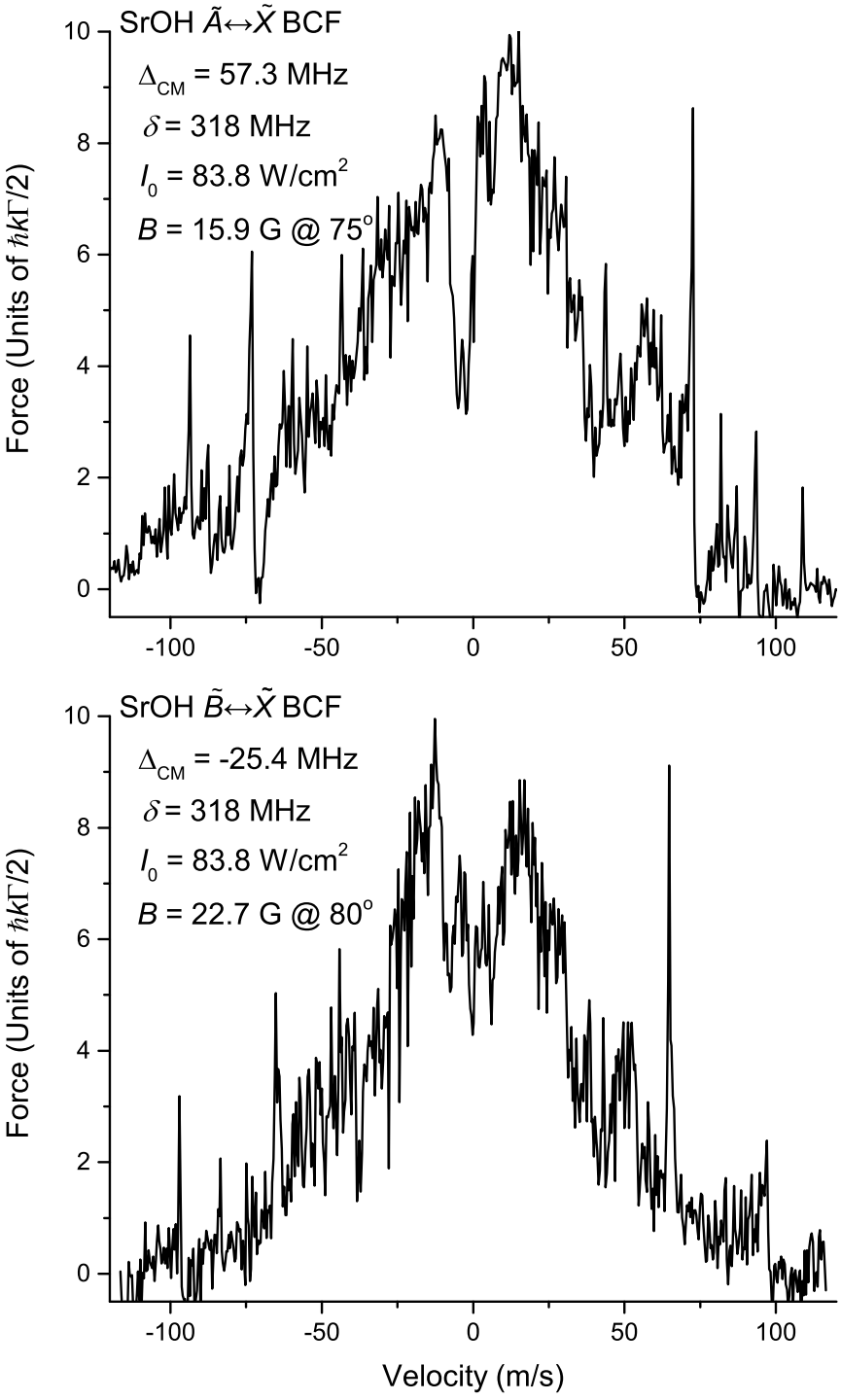

Fig. 5.8: Force vs. velocity profiles for $\delta = 50\,\Gamma$ BCF using the $P_{11}(1.5)/Q_{12}(0.5)$ $\tilde{A} \leftrightarrow \tilde{X}$ (top) and $P_{11}(0.5)/^{P}Q_{12}(1.5)$ $\tilde{B} \leftrightarrow \tilde{X}$ (bottom) transitions of SrOH, simulating the full 12+4 system with optimal magnetic field parameters as listed.

97.5% of the force in the closed 12+4 system. This implies 456 spontaneous decay photons in the time it would take to slow by 60 m/s. With the (000)-(100) decay channel closed by repumping, out-of-system decays would be 0.0024 of all decays. At this level of closure, 33% of addressed SrOH molecules would be slowed by 60 m/s before going dark.

Adding an additional saturated repump from $\tilde{X}(02^00)$ to $\tilde{B}(000)$ would create a 24+4 repump system, which would have an excited-state fraction at saturation of 1/7. This gives an equilibrated force of 95.8% of the closed system force, and a total closure of 0.9984, with the majority of the remaining decays to $\tilde{X}(200)$. This gives a 48% probability of an SrOH molecule being slowed by 60 m/s.

Using the $\tilde{B} \leftrightarrow \tilde{X}$ transitions at $\delta = 318\,\mathrm{MHz}$, the average force for molecular velocities between -30 m/s and $+30$ m/s is 6.59 $\hbar k\Gamma/2$. This is lower numerically, but the wavenumber k for this transition is larger, such that the force using $\tilde{B} \leftrightarrow \tilde{X}$ is about 7% stronger overall. This gives an expected number of decays of 417 to slow by 60 m/s, similar to the $\tilde{A} \leftrightarrow \tilde{X}$ case. The (000)-(000) FCF is more favorable at 0.9772 in this case, but $\tilde{B} \rightarrow \tilde{A}$ decay is also allowed. Estimating that the electronic decay branching is similar to that of the isoelectronic CaF, with 1 out of 4840 decays from $\tilde{B}$ ending in $\tilde{A}$ rather than $\tilde{X}$, the total closure with no repumping would be 0.9770. At that rate, less than one in ten thousand molecules would be slowed by 60 m/s. After repumping $\tilde{X}(100)$ through $\tilde{A}(000)$,

the closure rate is worse than that of using the $\tilde{A}$ state with one repump, even without considering the additional decay pathway of $\tilde{B} \rightarrow \tilde{A}$. Thus for SrOH, where at least one repump is almost certainly required, $\tilde{A} \leftrightarrow \tilde{X}$ BCF looks to be superior to $\tilde{B} \leftrightarrow X$ BCF.

This analysis is all based on simulation results at $\delta = 318\,\mathrm{MHz}$. It is of course possible to achieve stronger forces by increasing the bichromatic detuning, though this requires an increase in laser irradiance, the optimal value of which is proportional to δ^2. Practically, there is a trade-off between number of repumping frequencies required and the power required in the BCF lasers.

5.3 Experimental Design for BCF on CaF

To test the effectiveness of BCF in calcium monofluoride, it is easier to deflect a molecular beam, rather than slow it. The effect can be seen simply by measuring the position of the final beam, rather than needing the time-resolved measurement necessary for discerning slowing, and for well-collimated beam, smaller effects can be distinguished. This allows for shorter interaction regions and less required power for initial tests.

The BCF scheme laid out for CaF in Sec. 5.1 assumed a starting population in X, v=0 and N=1. A low rotational and vibrational temperature is necessary to have significant population in this rovibrational state. One relatively easy way to achieve this is to entrain CaF into a pulsed supersonic jet expansion. By briefly

opening a small aperture from a high-pressure region to a low-pressure one, the random motion of the gas in the high-pressure region is converted to directional motion out of the nozzle, cooling the translational and internal degrees of freedom [70].

For a monatomic carrier gas, the translational temperature T_p of a supersonic jet is expansion is given by

$$T_p = T_0 \left[1 + \frac{1}{3}\mathcal{M}^2\right]^{-1}, \tag{5.12}$$

where $\mathcal{M}$ is the Mach number of the beam, which is the ratio of the translational speed to the local speed of sound. The Mach number a distance x away from the nozzle of aperture diameter D can be estimated by [71]

$$\mathcal{M} = 3.26\left(\frac{x}{D} - 0.075\right)^{2/3} - 0.61\left(\frac{x}{D} - 0.075\right)^{-2/3} \tag{5.13}$$

up to a terminal Mach number of

$$\mathcal{M}_T = 133(P_0 D)^{0.4} \tag{5.14}$$

where P_0 is the backing pressure behind the nozzle in atmospheres and D is measured in centimeters [71]. The mean velocity of the jet at a given Mach

number is given by [72]

$$\bar{v} = \mathcal{M}\sqrt{\frac{5kT_0}{3m}}\left(1+\frac{1}{3}\mathcal{M}^2\right)^{-1/2}. \tag{5.15}$$

For example, at a backing pressure of three atmospheres and a nozzle aperture diameter of 1 mm, the terminal mach number is 82, occurring 12.6 cm downstream from the nozzle. At this Mach number, the translational temperature of the monatomic carrier gas is 0.13 K. The mean terminal velocity, which is dependent on the atomic mass of the gas species, would be 559 m/s for argon.

By seeding sulfur hexafluoride into an inert carrier gas such as argon, and laser-ablating a calcium target near the aperture of the expanding seeded-argon jet, hot CaF is formed, then taken up by the beam and cooled by collisions with the cold carrier gas [58]. Molecules entrained in such an expansion will rotationally cool with an efficacy dependent on such factors as the position of the ablation site relative to the expansion aperture, the timing of the ablation, and the energy in each abalation pulse [73]. Temperatures for diatomic molecules between 1 and 10 K have been regularly achieved through this method [73].

The relative thermal population of each rotational level in the ground state is given by [5]

$$\frac{N_N}{N_0} = (2N+1)\, e^{-hcBN(N+1)/kT}, \tag{5.16}$$

where the rotational constant B is 0.3437 cm^{-1} for the X state of CaF [76]. The

population in N=1 is maximized at 47% at 1.2 K, and decreases to 13% at 10K. A sufficient sample of the desired state of CaF can be produced through this method.

The supersonic beam can be collimated by first passing it through a conical skimmer, which has a restricted angular acceptance from the expansion nozzle and smoothly trims off the sides of the expansion without disrupting the central part [74]. After this, additional slit-shaped collimators can be added as needed. By collimating the molecular beam to a small size, the entire beam can be illuminated at the necessary BCF irradiances with realistic power requirements.

I now turn to a brief description of the specific experimental apparatus presently being used for initial tests in our own laboratory.

The dc magnetic field for dark state destabilization is created by a Helmholtz coil arrangement, which ensures a well-defined field magnitude and angle with little sensitivity to precise positioning of the interaction region within the coil volume. The field at the center of a pair of Helmholtz coils with current I flowing through N turns of radius R in each coil is given by

$$B = \left(\frac{4}{5}\right)^{3/2} \frac{\mu_0 N I}{R} \tag{5.17}$$

A 40 Gauss magnetic field, which is slightly larger than the optimum magnetic fields predicted for the BCF detunings simulated in Sec. 5.1, will be produced with two 10.9-cm average radius coils of 100 turns each, with a current of 4.84 A. In our apparatus, such coils are placed in air around a small interaction chamber

based on a Kimball Physics 2.75″ "spherical cube." Using 16 AWG copper magnet wire, the total resistance of the coils is approximately 1.88 Ω, requiring 9.10 V of potential difference to create the necessary current. These values of current and voltage are upper limits on what is expected to be necessary, so a modest power supply that can source 5A at 12V should be sufficient to drive the field coils. Significant heating will occur, as the magnet wire will be dissipating about 22 W of power at the 40 Gauss settings. This will be offset by direct thermal contact with a cooled water line, keeping the equilibrium temperature in a safe range.

The skew angle θ_{BE} can be set for linearly-polarized BCF simply by keeping the orientation of the magnetic field constant and rotating the optical polarization with a half-wave plate placed directly before the interaction region.

The generation of a laser field at the required frequency and power will be accomplished by amplification and doubling of a 1062 nm diode laser, in our case a Photodigm PH1064DBR100T8 distributed Bragg reflector (DBR) diode. About 5 mW of the output power of the diode is fiber-coupled into an IPG Photonics YAR-10K-1064-LP-SF fiber laser, which can produce over 10 W of output power. The high-power 1062 nm light is then passed through a Covesion MSHG1064-0.5-10 MgO:PPLN doubling crystal to produce over 1W of 531 nm light.

The production of the four components of the BCF optical field can be produced via acousto-optic modulators, in an identical fashion to earlier work on transverse deflection BCF [44]. The laser output is stabilized to $\omega_{eg}^{L} - \delta$, and a

portion is frequency-shifted in the AOM by $+2\delta$ before being recombined with the original frequency to form a beam with both bichromatic frequencies. In the case of longitudinal slowing, this bichromatic beam would need to be split and given appropriate Doppler offsets to address the molecular beam in a molecule-stationary frame. For deflection the velocity along the laser propagation direction is near zero, so this is unnecessary and the bichromatic laser beam can simply be directed through the interaction region and then retro-reflected to pass through it again from the opposite direction. Due to the necessary beat-phase relation of $\chi = 45°$ at the interaction region, the retroreflection must occur at a distance of $c\delta/8$ away. For $\delta = 30\,\Gamma = 190$ MHz, this places the retroreflector 19.7 cm away from the interaction region.

For an elliptically-shaped laser, the total power at irradiance I is given by

$$P = \pi I w_x w_y \tag{5.18}$$

for axial lengths w_x and w_y. For deflection, consider an elliptical BCF beam aligned such that w_y is perpendicular to the molecular beam propagation direction and w_x is parallel to it. If w_y is set to the transverse extent of the molecular beam at the interaction region, and P is set by available laser power, there is a fixed inverse relationship between I and w_x, which sets the interaction length. The interaction time is then determined by the velocity across the interaction length, which can be predicted from the supersonic jet velocity given by Eq. 5.15.

Estimating the force attained at a given detuning by a linear interpolation of the forces at the three detunings simulated, which is valid at least in the range of $30\,\Gamma \leq \delta \leq 100\,\Gamma$, this gives change in velocity as a function of detuning, at a particular molecular beam size and laser power,

$$\Delta v = \frac{\left(106.6\frac{\delta}{\Gamma} - 1562\right) P}{\left(\frac{\delta}{\Gamma}\right)^2 w_y v_x} \frac{\mathrm{m}\cdot\mathrm{s}}{\mathrm{kg}}. \tag{5.19}$$

Perhaps surprisingly, in the range $30\,\Gamma \leq \delta \leq 100\,\Gamma$, a larger change in velocity can be accomplished with a smaller detuning. At $w_y = 1$ mm, $v_x = 559$ m/s, $P = 250$ mW, and $\delta = 30\,\Gamma$, a change in velocity of 0.83 m/s is expected, giving an angular deflection of 2.2 milliradians. This preference for lower detunings does not extend to longitudinal slowing, as the interaction length is then set primarily by the crossing angle rather than the laser spot width. As described in Sec. 5.1, the primary limitation for CaF would be the out-of-system loss time.

Detection of the molecular beam position downstram will be accomplished through off-diagonal excitation on the $A \leftrightarrow X$ (1-0) line at 585 nm [75], a wavelength we produce using a Coherent 699 ring dye laser with Rhodamine 6G dye. The A, $v = 1$ state will preferentially decay diagonally to X, $v = 1$ at 606 nm [76], so that the laser-induced fluorescence (LIF) is well to the red of the laser light and can be isolated with cut-off filters before detection. With sufficient LIF, the spatial profile of the fluorescence can be imaged directly with a camera. Alterna-

tively, a translating slit can be used as a spatial filter before collection onto a single photodetector, and a spatial profile can be built up from trials over multiple slit positions. Differencing the spatial profiles with and without the BCF beams will show what proportion of the beam is deflected by the BCF and to what extent.

Chapter 6

Conclusions and Outlook

6.1 Conclusions

I have shown in the course of this dissertation that the bichromatic force, which has been previously demonstrated to greatly exceed the radiative force in two-level atomic systems, has the potential to be extended fruitfully to more complex laser fields and to multilevel systems.

By adding additional laser frequencies at $\pm 3\delta$, the bichromatic force is extended to a polychromatic force (PCF), which creates a stronger force for a given total laser power and has a smaller average excited-state fraction. Additionally, as the PCF field is created by an overlap of monochromatic sources, it has the same periodic phase rotation reversal as BCF, which contributes to the robustness of the force against imbalances in beat phase and power. Additional odd harmonics can be added to make the optical field more closely approximate a Dirac comb, but the diminishing returns from doing so indicate that four colors constitute the ideal PCF configuration.

Simulations of the BCF on multilevel systems show that BCF can be used in both a small- and large-detuning regime relative to the range of transition frequencies in the system. In the large-detuning regime, the optimal laser irradiance is the one that produces a quadrature sum Rabi frequency $\Omega_{\text{tot}} = \sqrt{3/2}\,\delta$ and the optimal carrier frequency is tuned near a transition rather than at the c.o.m. of the system, both of which were open questions prior to the work described here.

I have shown that techniques for destabilization of intrasystem dark state formation that have previously been used in conjunction with the radiative force can also work in conjunction with the bichromatic force and developed general scaling rules for optimal parameters for destabilization via magnetic field. Specifically, the optimal Zeeman splitting scales as δ and the optimal intra-ground-state coupling scales as $\sqrt{\delta}$.

Recovering population that has been lost through radiative decay to non-cycling states can be achieved through optical repumping. Direct repumping, where population is reintroduced directly into the BCF cycle, has been shown to be possible, but it interacts suboptimally with the coherent cycling of the BCF. This causes specific requirements for repump powers and results in a lowering of the force. Indirect repumping, where population is transferred to a state that spontaneously decays back into the BCF cycle, was found to avoid both of these issues and is thus the preferred repumping method when it is available.

My simulations of BCF in realistic models of the molecules CaF and SrOH

show that the BCF can be used to produce forces orders of magnitude stronger than the radiative force with readily attainable laser irradiances and magnetic fields. An overview for an experimental test of BCF deflection for a CaF molecular beam has been given.

6.2 Outlook

The system described in Sec. 5.3 is substantially developed in our lab at UConn. In the immediate future, it will be utilized to measure BCF beam deflection to demonstrate molecular BCF, since this has not yet been achieved anywhere. The details of the experiment and its results will be a primary subject of the thesis of Scott Galica. I have also been collaborating with the Doyle group at Harvard to develop plans for experimental demonstration of BCF in SrOH, also through molecular beam deflection for intial experiments.

Looking ahead, molecular BCF is of primary interest as a technique for more efficiently slowing molecules to trappable velocities. The velocity range of a static BCF field is not sufficient to slow a room-temperature thermal beam to rest, as can be seen by comparing the jet velocities of Eq. 5.15 to the velocity ranges in Table 5.2. However, a functional room-temperature BCF decelerator could still be accomplished by extending the velocity range, either through a multi-stage arrangement of sequential BCF field interaction regions, or by chirping the laser frequency to follow the decreasing mean velocity of the molecules, as has been

demonstrated already in our lab for BCF slowing of He^* [44]. Alternatively, the initial velocity of the molecules can be greatly decreased through use of a buffer-gas cooled source, similar to the CaF source used by the Doyle group [8] or the SrF source used by the DeMille group [12].

One of the commonly-encountered problems when radiatively slowing molecular beams is the need for transverse confinement [77]. As the longitudinal velocity of the beam is slowed, the transverse velocity is generally unaffected, leading to a "pancaking" of the beam where the angular spread increases drastically. If this occurs over an extended region, it can greatly reduce the flux of molecules delivered to a trapping region. Using BCF can avoid this problem, as the entire slowing interaction can take place on a length scale that does not allow for the transverse velocity of the molecules to move them out of the trapping region. Essentially, the molecules can be stopped on demand directly at the trapping position.

Once molecules have been slowed and then trapped, using for example the molecular MOT techniques pioneered by the DeMille group [13,14], a plethora of opportunities for exploring ultracold molecular physics becomes available. Examples include using the dipole moment of ultracold polar molecules as qubits in a quantum computer [78], finer measurement of the electron electric dipole moment by measuring the precession of polar molecules in external field [79,80], and exploration of Rydberg physics in loosely-bound states that are stable only in ultracold settings, including both traditional Rydberg states like $CaF^+ + e^-$ and more exotic

systems, such as "heavy Rydberg" states of CaF near the ion-pair limit $Ca^+ + F^-$ [81].

For small molecules in general, the very favorable results from indirect repumping simulations open a wide vista of possibilities. A transition need not be closed to the level of the CaF or SrOH transitions examined here in order to achieve a strong and sustained optical force using BCF, as long as an indirect repumping route is available. The PCF, with its relative reduction in excited state population and its larger force per unit laser power, may also become an attractive tool in cases where decay to distant states is a limiting factor.

Appendix A

Mathematica Code

A significant portion of this dissertation is based on numerical solutions of the time dependence of the density matrix for various systems. I include here a representative Mathematica notebook that can be used to carry out some of these solutions. It was tested and optimized using Mathematica version 10.

Though little of the original remains, the code is ultimately based on a FORTRAN program for computing the BCF in two-level systems to compare with experimental results by Grimm et al [28,82], supplied to our group courtesy of Hal Metcalf. This program was updated and then reproduced in Mathematica by Drew Chieda [15,44], and then further updated to provide more flexibility to study PCF by Scott Galica [46].

Each of these previous versions had solved for the time dependence of the Bloch vector. As this approach does not generalize to multilevel systems, this version uses the density matrix instead, for a system with an arbitrary number of states in both the ground and excited manifold.

Below is a pseudocode description of the functioning of a version of the

program that can model PCF fields, which includes BCF fields when $n_{\max} = 0$. Following the pseudocode is the full Mathematica code and then a usage guide for utilization of the code.

A.1 Pseudocode

Define the form of the co-rotating BCF/PCF Rabi frequency as per Eq. 3.4

$$\begin{aligned} \Omega BCF(t,z) &= 4\Omega \sum_{n=0}^{n_{\max}} [\cos(kz)\cos((2n+1)d\,t)\cos((2n+1)\chi/2 \\ &+ i\sin(kz)\sin((2n+1)d\,t)\sin((2n+1)\chi/2)] \end{aligned} \tag{A.1}$$

Open user input file

Read in the number of calculations *ncalc*

Do for the number of calculations

Read in calculation parameters

$nmax$, PCF field series truncation limit

mm, Number of ground states

nn, Number of excited states

γ_{ij}, $1 \le i \le nn$, $1 \le j \le mm$, State-to-state decay rates

Δe_i, $1 \le i \le nn$, Excited state energies referenced to com

Δg_i, $1 \le i \le mm$, Ground state energies referenced to com

$\mu eSIN_{ij}$, $1 \le i, j \le nn$, The $p = \pm 1$ term of $\langle e_i| H_B |e_j\rangle / B_{\pm 1}$

$\mu eCOS_{ij}$, $1 \leq i, j \leq nn$, The $p = 0$ term of $\langle e_i| H_B |e_j\rangle / B_0$

$\mu gSIN_{ij}$, $1 \leq i, j \leq mm$, The $p = \pm 1$ term of $\langle g_i| H_B |g_j\rangle / B_{\pm 1}$

$\mu gCOS_{ij}$, $1 \leq i, j \leq mm$, The $p = 0$ term of $\langle g_i| H_B |g_j\rangle / B_0$

B, dc magnetic field magnitude

θBE, dc magnetic field skew angle

Ω, BCF Rabi amplitude factor

d, Fundamental bichromatic detuning

$Omegaeg_{ij}$, $1 \leq i \leq nn$, $1 \leq j \leq mm$, $\kappa_{ij} \times \langle i| \hat{r} \cdot \hat{\epsilon} |j\rangle$

θ, Global phase of BCF field at $t = 0$

χ, Relative BCF beat train phase

δL, Detuning of BCF carrier frequency from transition com

xkvmin, Minimum velocity to simulate

xkvmax, Maximum velocity to simulate

xkvsteps, Number of velocity steps

tequil, Time to allow for system equilibration

Initialize output table with one entry for each velocity step

Do for each velocity step *ve*

Compute fixed-velocity Rabi frequency for each transition

$$\Omega eg_{ij}(t) = Omegaeg_{ij} \cdot \Omega BCF(t, ve \cdot t)$$

Compute fixed-velocity Rabi frequency gradient for each transitiion

$$D\Omega eg_{ij}(t) = Omegaeg_{ij} \left(\frac{\partial}{\partial z} \Omega BCF(t, z)\right)\Big|_{z=ve \cdot t}$$

Set sampling time as in the original FORTRAN code

$$tend = 2\pi \left(1/\left|ve\right| + 200/d\right)$$

Set sampling interval as in the original FORTRAN code

$$dt = 3/\mathrm{Max}\left[d, 10\left|ve\right|\right]$$

Compute Hamiltonian as

$$H = \begin{pmatrix} H_e & H_{eg} \\ H_{eg}^{\dagger} & H_g \end{pmatrix} \tag{A.2}$$

$$\left(H_e\right)_{ij} = \Delta e_i \delta_{ij} + B\left(\sin\theta_{BE}\mu eSIN_{ij}/\sqrt{2} + \cos\theta_{BE}\mu eCOS_{ij}\right) \tag{A.3}$$

$$\left(H_{eg}\right)_{ij} = \left(\Omega_{eg}\right)_{ij}/2 \tag{A.4}$$

$$\left(H_g\right)_{ij} = \left(\delta L + \Delta g_i\right)\delta_{ij} + B\Big(\sin\theta_{BE}\mu gSIN_{ij}/\sqrt{2} + \cos\theta_{BE}\mu gCOS_{ij}\Big) \tag{A.5}$$

Compute dispersion matrix as

$$\frac{\partial\rho}{\partial t} = \begin{pmatrix} \Gamma_e & \Gamma_{eg} \\ \Gamma_{eg}^{\dagger} & \Gamma_g \end{pmatrix} \tag{A.6}$$

$$\left(\Gamma_e\right)_{ij} = -\left(\sum_{k=1}^{mm} \frac{\gamma_{ik} + \gamma_{jk}}{2}\right)\rho eiej \tag{A.7}$$

$$\left(\Gamma_{eg}\right)_{ij} = -\left(\sum_{k=1}^{mm} \frac{\gamma_{ik}}{2}\right)\rho eigj \tag{A.8}$$

$$\left(\Gamma_g\right)_{ij} = \delta_{ij}\sum_{k=1}^{nn} \gamma_{ki}\rho ekek \tag{A.9}$$

Compute starting state as

$$\rho eiej(-tequil) = 0 \quad \text{(A.10)}$$

$$\rho eigj(-tequil) = 0 \quad \text{(A.11)}$$

$$\rho gigj(-tequil) = \delta_{ij}/mm \quad \text{(A.12)}$$

Compute equations of motion for ρ as a matrix equation

$$\dot{\rho} = \frac{1}{i}\left(H \cdot \rho - \rho \cdot H\right) + \frac{\partial \rho}{\partial t} \quad \text{(A.13)}$$

Extract the upper diagonal part of the matrix equation

Numerically solve the system of equations from $-tequil$ to $tend$

Set FF, EE, and $icount$ to zero

Do for each time step between 0 and $tend$

FF += $\sum_{i,j} 2\,\mathrm{Re}\left[\rho eigj(t) \times D\Omega eg^{*}_{ij}(t)\right]$ (force at t)

EE += $\sum_{i} \rho eiei(t)$ (excited state fraction at t)

$icount$++

End time loop

Enter $FF/icount$ and $EE/icount$ into output table for this velocity

End velocity loop

Export parameters and output table as a TSV file

End calculation loop

A.2 Mathematica Code

```
(*mplusn_hamiltonian_PCF.nb*)
(*Author : Leland Aldridge*)
(*Last Modified : July 25, 2016*)
(*Given a definition of an m + n system of user - defined number of levels, polychromatic optical parameters, and skew DC magnetic field parameters, this notebook constructs a system of equations of motion for the density matrix of the system and then solves them numerically. It does this by first constructing a Hamiltonian and then explicitly obtaining a formula for the derivatives of the components of the density matrix from the Liouville equation.*)

(*Compute a row of the excited states sub-Hamiltonian, starting from the diagonal. Included are field-free level energies and magnetic dipole effects*)
eRow[start_, end_] := Table[If[i == start, Δe[i] + B (Sin[θBE] μeSIN[start, i]/
    Sqrt[2] + Cos[θBE] μeCOS[start, i]), B (Sin[θBE] μeSIN[start, i]/Sqrt[2] +
    Cos[θBE] μeCOS[start, i])], {i, start, end}]
(*Using the eRow function, construct the excited-state sub-Hamiltonian*)
eMatrix[n_] := Block[{s}, (For[i = 1, i <= n, i++, If[i == 1, s = {eRow[1, n]},
    AppendTo[s, Join[Table[Conjugate[s[[k, i]]], {k, 1, i - 1}], eRow[i, n]]]]];
    Return[s])]
(*Compute a row of the ground states sub-Hamiltonian, starting from the diagonal. Included are field-free level energies (dressed) and magnetic dipole effects*)
gRow[start_, end_] := Table[If[i == start, δL + Δg[i] + B (Sin[θBE] μgSIN[start,
    i]/Sqrt[2] + Cos[θBE] μgCOS[start, i]), B (Sin[θBE] μgSIN[start, i]/Sqrt[2]
    + Cos[θBE] μgCOS[start, i])], {i, start, end}]
(*Using the gRow function, construct the ground state sub-Hamiltonian*)
gMatrix[m_] := Block[{s}, (For[i = 1, i <= m, i++, If[i == 1, s = {gRow[1, m]},
    AppendTo[s, Join[Table[Conjugate[s[[k, i]]], {k, 1, i - 1}], gRow[i, m]]]]];
    Return[s])]
(*Compute the ground-excited sub-Hamiltonian, including the Rabi frequencies due to the optical field coupling*)
egMatrix[n_, m_, t_] := Table[Table[Ωeg[i, j, t]/2, {j, 1, m}], {i, 1, n}]
(*Using the sub-Hamiltonians, construct the full Hamiltonian*)
H[α_, β_, t_] := (Block[{top, bottom}, top = Table[ Flatten[{eMatrix[α][[x]],
    egMatrix[α, β, t][[x]]}], {x, 1, α}]; bottom = Table[ Flatten[{
    ConjugateTranspose[egMatrix[α, β, t]][[y]], gMatrix[β][[y]]}], {y, 1, β}];
    Return[Transpose[ Table[Flatten[{Transpose[top]
    [[z]], Transpose[bottom][[z]]}], {z, 1, α + β}]]])
(*Functionalize the preferred naming scheme of ρeigj*)
```

```
ρpart[n_, m_, t_] := ToExpression["ρ" <> n <> m <> "[" <> ToString[t] <>
    "]"]
(*Construct a list of all the matrix elements of ρ for a given system size*)
ρList[n_, m_] := (string = "{"; For[i = 1, i <= n + m, i++, For[j = i, j <= n
    + m, j++, string = string <> If[i <= n, "ρe" <> ToString[i], "ρg" <>
    ToString[i - n]] <> If[j <= n, "e" <> ToString[j], "g" <> ToString[j - n]]
    <>                                                          ","]];
    Return[ToExpression[StringDrop[string, -1] <> "}"]])
(*Construct the phenomenological dispersion terms of the density matrix time
    derivatives, for decay rates γ between states*)
eDispRow[start_, n_, m_, w_] := Block[{s, temp}, (For[j = start, j <= n, j++,
    If[j == start, temp = {Sum[-γ[j, k], {k, 1, m}] ρpart["e" <> ToString[j],
    "e" <> ToString[j], w]}, AppendTo[temp, Sum[-(γ[start, k] + γ[j, k])/2,
    {k, 1, m}] ρpart[ "e" <> ToString[start], "e" <> ToString[j], w]]]]; Re-
    turn[temp])]
eDispMatrix[n_, m_, w_] := Block[{s}, (For[i = 1, i <= n, i++, If[i == 1, s =
    {eDispRow[1, n, m, w]}, AppendTo[s, Join[Table[Conjugate[s[[k, i]]], {k, 1,
    i - 1}], eDispRow[i, n, m, w]]]]]; Return[s])]
gDispMatrix[n_, m_, t_] := Table[Table[ If[i == j, Sum[γ[k, i] ρpart["e" <>
    ToString[k], "e" <> ToString[k], t], {k, 1, n}], 0], {i, 1, m}], {j, 1, m}]
egDispMatrix[n_, m_, t_] := Table[Table[ Sum[-γ[i, k]/2, {k, 1, m}] ρpart["e" <>
    ToString[i], "g" <> ToString[j], t], {j, 1, m}], {i, 1, n}]
DispMatrix[n_, m_, t_] := (Block[{top, bottom}, top = Table[ Flatten[{
    eDispMatrix[n, m, t][[x]], egDispMatrix[n, m, t][[x]]}], {x, 1, n}]; bottom =
    Table[Flatten[{ConjugateTranspose[egDispMatrix[n, m, t]][[y]],
    gDispMatrix[n, m, t][[y]]}], {y, 1, m}]; Return[Transpose[ Table[Flatten[{
    Transpose[top][[z]], Transpose[bottom][[z]]}], {z, 1, n + m}]]])
(*Compute the starting state, where the system is decoherent and population is
    equally distributed among the ground states*)
equGround[n_, m_] := (Block[{temp}, temp = {}; For[i = 1, i <= n + m, i++,
    (AppendTo[temp, {}]; For[j = i, j <= n + m, j++, AppendTo[temp[[i]],
    If[i <= n && j <= n, 0, If[i == j, 1/m, 0]]]])]; Return[temp]])
(*Construct an actual matrix out of the density matrix elements for a given system
    size*)
ρ[n_, m_, t_] := Table[Table[ If[i >= j, ρpart[ If[j <= n, "e" <> ToString[j], "g"
    <> ToString[j - n]], If[i <= n, "e" <> ToString[i], "g" <> ToString[i -
    n]], t], Conjugate[ρpart[ If[i <= n, "e" <> ToString[i], "g" <> ToString[i
    - n]], If[j <= n, "e" <> ToString[j], "g" <> ToString[j - n]], t]]], {i, 1, n
    + m}], {j, 1, n + m}]
(*Select and read input file*)
{FileNameSetter[Dynamic[infile]], Dynamic[infile]}
instr = OpenRead[infile];
```

```
indir = DirectoryName[infile];
SetDirectory[indir];
ncalcs = Read[instr, Number]; (*read number of batch calcs to make*)
dircount = 1;
While[DirectoryQ[ "mplusn_PCF_" <> DateString[{"MonthShort", "-",
      "DayShort"}] <> "_" <> ToString[dircount]], dircount++];
outdir = CreateDirectory[ "mplusn_PCF_" <> DateString[{"MonthShort", "-",
      "DayShort"}] <> "_" <> ToString[dircount]];
SetDirectory[outdir];
CopyFile[infile, outdir <> "/parameters.txt"];
xkvstepsD = 1;
ntimeD = 1;
(*Batch calculations*)
ProgressIndicator[Dynamic[cprog], {1, ncalcs}]
(*Velocity steps*)
ProgressIndicator[Dynamic[vprog], {1, Dynamic[xkvstepsD]}]
(*Time steps*)
ProgressIndicator[Dynamic[tprog], {1, Dynamic[ntimeD]}]
(*Co-rotating Rabi frequency definition*)
ΩBCF[t_, z_] := 4 Ω Sum[(Cos[(2 n + 1) χ/2] Cos[ z] Cos[(2 n + 1) (d*t + θ)] +
      I*Sin[(2 n + 1) χ/2] Sin[z] Sin[(2 n + 1) (d*t + θ)]), {n, 0, nmax}];
(*Main calculation loop*)
Timing[
Do[
cprog = calc;
outstr = OpenWrite["mplusn_bcf_output" <> ToString[calc] <> ".dat"];
Write[outstr, "Calculation Number " <> ToString[calc] <> " of " <>
      ToString[ncalcs]];
Write[outstr, "Parameters"];
(*Dirac comb cosine series termination point, zero gives BCF*)
nmax = IntegerPart[N[Read[instr, Number]]];
Write[outstr, "Series termination number = " <> ToString[nmax]];
(*number of levels*)
mm = IntegerPart[N[Read[instr, Number]]];
Write[outstr, "Number of ground states = " <> ToString[mm]];
nn = IntegerPart[N[Read[instr, Number]]];
Write[outstr, "Number of excited states = " <> ToString[nn]];
(*decay rates*)
gamma = {};
For[i = 1, i <= nn, i++, (gammarow = {}; For[j = 1, j <= mm, j++, AppendTo[
      gammarow, N[Read[instr, Number]]]; Write[outstr, "gamma_" <>
```

```
        ToString[i] <> "_" <> ToString[j] <> " = " <> ToString[Last[gammarow]]
        <> " Gamma"];];AppendTo[gamma, gammarow];)];
γ[n_, m_] := gamma[[n, m]];
(*unperturbed energy levels*)
Deltae = {};
For[i = 1, i <= nn, i++, AppendTo[Deltae, N[Read[instr, Number]]]; Write[outstr,
        "Delta_e" <> ToString[i] <> " = " <> ToString[Last[Deltae]] <> "
        Gamma"];];
Δe[n_] := Deltae[[n]];
Deltag = {};
For[i = 1, i <= mm, i++,AppendTo[Deltag, N[Read[instr, Number]]]; Write[
        outstr, "Delta_g" <> ToString[i] <> " = " <> ToString[Last[Deltag]] <>
        " Gamma"];]; Δg[n_] := Deltag[[n]];
(*matrix elements of the magnetic-field- dependent terms of the Hamiltonian, mag-
        netic dipole only, "sin" terms for perpendicular component (Δm=+/-1) and
        "cos" terms for parallel component (Δm=0)*)
muesin = {};
For[i = 1, i <= nn, i++, (muesinrow = {}; For[j = 1, j <= nn, j++,
        AppendTo[muesinrow, N[Read[instr, Number]]]; Write[outstr, "mu_e" <>
        ToString[i] <> "_" <> ToString[j] <> "SIN = " <> ToString[Last[
        muesinrow]]];]; AppendTo[muesin, muesinrow];)];
μeSIN[n_, m_] := muesin[[n, m]];
muecos = {};
For[i = 1, i <= nn, i++, (muecosrow = {}; For[j = 1, j <= nn, j++,
        AppendTo[muecosrow, N[Read[instr, Number]]]; Write[outstr, "mu_e" <>
        ToString[i] <> "_" <> ToString[j] <> "COS = " <> ToString[Last[
        muecosrow]]];]; AppendTo[muecos, muecosrow];)];
μeCOS[n_, m_] := muecos[[n, m]];
mugsin = {};
For[i = 1, i <= mm, i++, (mugsinrow = {}; For[j = 1, j <= mm, j++,
        AppendTo[mugsinrow, N[Read[instr, Number]]]; Write[outstr, "mu_g" <>
        ToString[i] <> "_" <> ToString[j] <> "SIN = " <> ToString[Last[
        mugsinrow]]];]; AppendTo[mugsin, mugsinrow];)];
μgSIN[n_, m_] := mugsin[[n, m]];
mugcos = {};
For[i = 1, i <= mm, i++, (mugcosrow = {}; For[j = 1, j <= mm, j++,
        AppendTo[mugcosrow, N[Read[instr, Number]]]; Write[outstr, "mu_g" <>
        ToString[i] <> "_" <> ToString[j] <> "COS = " <> ToString[Last[
        mugcosrow]]];]; AppendTo[mugcos, mugcosrow];)];
μgCOS[n_, m_] := mugcos[[n, m]];
(*magnetic field parameters*)
B = N[Read[instr, Number]];
```

```
Write[outstr, "Magnetic field magnitude = " <> ToString[B] <> " Gamma"];
thetaBEx = N[Read[instr, Number]];
Write[outstr, "Magnetic field angle = " <> ToString[thetaBEx] <> " degrees"];
θBE = thetaBEx*Degree;
(*Optical field parameters*)
Ω = N[Read[instr, Number]];
Write[outstr, "BCF Rabi amplitude = " <> ToString[Ω] <> " Gamma"];
d = N[Read[instr, Number]];
Write[outstr, "Bichromatic detuning = " <> ToString[d] <> " Gamma"];
(*Transition electric dipole moments between ground and excited states, normal-
    ized*)
Omegaeg = {};
For[i = 1, i <= nn, i++, (Omegaegrow = {}; For[j = 1, j <= mm, j++, AppendTo[
    Omegaegrow, N[Read[instr, Number]]]; Write[outstr, "kappa_e" <>
    ToString[i] <> "_g" <> ToString[j] <> " = " <> ToString[Last[
    Omegaegrow]]];]; AppendTo[Omegaeg, Omegaegrow];)];
Ωeg[n_, m_, t_] := Omegaeg[[n, m]] ΩBCF[t, ve*t];
DΩeg[n_, m_, t_] := Omegaeg[[n, m]] D[ΩBCF[t, z], z] /. z -> (ve*t);
(*More optical field parameters*)
xtheta = N[Read[instr, Number]];
Write[outstr, "Initial global phase = " <> ToString[xtheta] <> " degrees"];
xchi = N[Read[instr, Number]];
Write[outstr, "Relative BCF phase = " <> ToString[xchi] <> " degree"];
δL = N[Read[instr, Number]];
Write[outstr, "BCF carrier frequency detuning = " <> ToString[δL] <>
    " Gamma"];
(*Velocity range of simulations*)
xkvmin = N[Read[instr, Number]]; (*minimum velocity for calc in γ/ k*)
Write[outstr, "Minimum velocity = " <> ToString[xkvmin] <> " Gamma/k"];
xkvmax = N[Read[instr, Number]]; (*maximum velocity for calc in γ/ k*)
Write[outstr, "Maximum velocity = " <> ToString[xkvmax] <> " Gamma/k"];
xkvsteps = N[Read[instr, Number]];(* number of velocity steps between kvmin and
    kvmax*)
Write[outstr, "Number of velocity steps = " <> ToString[xkvsteps] <>
    " Gamma/k"];
tequil = N[Read[instr, Number]];(*time to allow for steady- state equilibration*)
Write[outstr, "Equilibration time = " <> ToString[tequil] <> " 1/Gamma"];
xkvstepsD = xkvsteps;
(*prepare data for calculations*)
χ = xchi/180*\[Pi]; (*phase difference in radians*)
θ = xtheta / 180*\[Pi]; (*initial phase in radians*)
vrange = xkvmax - xkvmin;
```

```
BCF = Table[{i, 0, 0}, {i, xkvmin + (vrange/(2 xkvsteps)), xkvmax, vrange/
      xkvsteps}];
Do[
vprog = vcnt;
ve = BCF[[vcnt, 1]];
(*Initialize computational parameters for force and ODE*)
dF = 0;
(*Define/reset computational rolerances*)
rtol = 8; (*relative tolerance*)
atol = 8; (*absolute tolerance*)
tstart = -tequil; (* give the solution some time to reach equilibrium behavior*)
(*Set the sampling interval and sampling time region, as in original FORTRAN
      code*)
dt = 3*(1/(Max[Abs[d], Abs[BCF[[vcnt, 1]]]*10));
tend = 2 \[Pi]/Abs[BCF[[vcnt, 1]]]*(1 + 200*Abs[BCF[[vcnt, 1]]]/d);
FF = 0;
EE = 0;
icount = 0;
iflag = 1;
ntime = IntegerPart[tend/dt] - 1;(*number of time steps*)
ntimeD = ntime;
(*Construct the equations of motion from the Hamiltonian, via the Liouville equa-
      tion*)
rates = ((1/ I (H[nn, mm, t].ρ[nn, mm, t] - ρ[nn, mm, t].H[nn, mm, t]) +
      DispMatrix[nn, mm, t]));
(*Solve the equations of motion*)
solution = NDSolve[{Flatten[ D[Table[ρ[nn, mm, t][[i, i ;; (nn + mm)]], {i, 1, (nn
      + mm)}], t]] == Flatten[ Table[rates[[i, i ;; (nn + mm)]], {i, 1, (nn +
      mm)}]], Table[ρ[nn, mm, tstart][[i, i ;; (nn + mm)]], {i, 1, (nn + mm)}]
      == equGround[nn, mm]}, ρList[nn, mm], {t, tstart, tend}, Method ->
      "ExplicitRungeKutta",MaxSteps -> ∞];
tstart = 0;
(*Sample the force and excited-state fraction from the solved density matrix tra-
      jectories*)
Do[
tprog = tcnt;
tstop = tstart + dt; (*assign new tstop*)
If[tstop > 0, (*Past the allowed equilibration time, evaluate force and add to av-
      erage*)
icount++;
(*Instantaneous force is given by -Tr(ρ∇H)*)
```

```
dF = Sum[2*(Re[(ρpart["e" <> ToString[i], "g" <> ToString[j], tstop]*
      Conjugate[DΩeg[i, j, tstop]])]), {i, 1, nn}, {j, 1, mm}] /. solution[[1]];
FF = FF + dF;
dE = Sum[(Re[ρpart["e" <> ToString[i], "e" <> ToString[i], tstop]]), {i, 1, nn}]
      /. solution[[1]];
EE = EE + dE;
];
tstart = tstop;
, {tcnt, 1, ntime}]; (*Do loop over time*)
BCF[[vcnt, 2]] = FF/icount; (*average force*)
BCF[[vcnt, 3]] = EE/icount; (*average excited fraction*)
, {vcnt, 1, xkvsteps}] (*Do loop over velocitites*)
Export[outstr, BCF, "TSV"]; (*Save output force vs. velocity data to file*)
Close[outstr];
, {calc, 1, ncalcs}] (*Do loop over ncalcs*)
Close[instr];
SetDirectory[indir];
] (*end timing call*)
```

A.3 Usage Guide

The current version of the multilevel BCF/PCF simulation program, given above, takes an input file which requires explicit entry of all system parameters. This includes the zero-field energies of the states, the relative electric dipole coupling strengths between the states of the ground and excited manifolds, and the magnetic coupling strengths between the states within each manifold. This allows for flexibility in simulating arbitrary systems but does require pre-calculation of these parameters for molecular systems.

Many of the parameters will be fixed for a particular system under consideration; the remaining parameters are those that specify the externally applied fields, optical and magnetic, and the velocities at which to compute the force.

For atomic systems, the Atomic Density Matrix (ADM) application for Mathematica is freely available from Rochester Scientific [83] and can be used to compute the energy levels and coupling strengths needed for these simulations. Starting from hyperfine constants and state numbers, the ADM application can construct a full description of the system, including interaction with optical or static EM fields, in full or in the RWA. I am not aware of any similar application that can do the same for arbitrary molecular systems, diatomic or otherwise. For the molecular systems considered in this dissertation, a complete description of the method for computing the relevant parameters is given in Chapter 5.

The input file format for supplying parameters to the Mathematica program is a plaintext file, which begins with the number of parameter sets to be simulated, followed by one parameter set per line with the parameters separated by tabs. The order in which the parameters are expected is given in the pseudocode description of the program in Sec. A.1. The parameters are expected to be in units of Γ and k, with the magnetic field strength in units of $\hbar\Gamma/\mu_B g_s$.

The system-fixed parameters are determined in the following way. The numbers of states in the ground- and excited-state manifolds are given by mm and nn, respectively. In units of Γ, the channel decay rates $\gamma_{ij} = \kappa_{ij}^2$. $Omegaeg_{ij}$ gives the relative strength of the Rabi frequency on each transition, and is equal to κ_{ij} times a geometric factor based on the light polarization. For example, with π-polarized light, $Omegaeg_{ij} = \kappa_{ij}$ for transitions where $\Delta M_F = 0$, and is

zero otherwise. κ_{ij} is computed via Eqs. 5.3 – 5.7. The field-free energies, Δe_i and Δg_i, are entered in units of Γ and are referenced to the respective excited- or ground-state manifold center of mass energies. The magnetic coupling parameters, $\mu eSIN_{ij}$, $\mu eCOS_{ij}$, $\mu gSIN_{ij}$, and $\mu gCOS_{ij}$ are computed from Eqs. 5.3 and 5.9.

For example, the matrix elements of $\vec{B} \cdot \hat{S}$ within the excited-state manifold of the CaF $B \leftrightarrow X$ $P_{11}(1.5)/{}^{P}Q_{12}(0.5)$ system are, as given by Eq. 5.9,

$$\begin{pmatrix} 0 & \frac{1}{2}B_{-1} & \frac{1}{2}B_0 & \frac{1}{2}B_{+1} \\ -\frac{1}{2}B_{+1} & -\frac{1}{2}B_0 & -\frac{1}{2}B_{+1} & 0 \\ \frac{1}{2}B_0 & \frac{1}{2}B_{-1} & 0 & -\frac{1}{2}B_{+1} \\ -\frac{1}{2}B_{-1} & 0 & \frac{1}{2}B_{-1} & \frac{1}{2}B_0 \end{pmatrix} \tag{A.14}$$

with the states $|F, M_F\rangle$ ordered as $|0,0\rangle$, $|1,-1\rangle$, $|1,0\rangle$, $|1,+1\rangle$. The matrix elements depend on the spherical components of the magnetic field, and the matrix is split into the part depending on B_0, $\mu eCOS$, and the part depending on $B_{\pm 1}$, $\mu eSIN$, for entry into the input file. In this case,

$$\mu eCOS = \begin{pmatrix} 0 & 0 & \frac{1}{2} & 0 \\ 0 & -\frac{1}{2} & 0 & 0 \\ \frac{1}{2} & 0 & 0 & 0 \\ 0 & 0 & 0 & \frac{1}{2} \end{pmatrix} \tag{A.15}$$

and

$$\mu eSIN = \begin{pmatrix} 0 & \frac{1}{2} & 0 & -\frac{1}{2} \\ \frac{1}{2} & 0 & \frac{1}{2} & 0 \\ 0 & \frac{1}{2} & 0 & \frac{1}{2} \\ -\frac{1}{2} & 0 & \frac{1}{2} & 0 \end{pmatrix}. \tag{A.16}$$

The terms that depend on B_{+1} pick up a negative sign due to the definition of the magnetic field in spherical coordinates, Eq. 4.3. It should also be noted that this makes $\mu eSIN$ Hermitian.

The remaining external parameters are determined as follows. The Dirac comb series truncation limit $n_{\max}$ determines the form of the optical field: 0 gives a BCF field, 1 gives a 4-color PCF field, etc. B and θBE give the magnitude and angle of the dc magnetic field, with B expected in units of $\hbar\Gamma/\mu_B g_s$ and θBE in degrees. Ω, expected in units of Γ, gives an overall Rabi frequency amplitude, such that the Rabi frequency amplitude on each transition is given by $\Omega \times Omegaeg_{ij}$. d, in units of Γ, sets the bichromatic detuning. θ sets the global BCF phase at $t = 0$, and χ sets the relative phase between the counterpropagating BCF beat trains at $z = 0$; both are specified in degrees. δL sets the detuning of the BCF carrier frequency from the frequency spacing between the ground- and excited-state manifold centers of mass.

The velocity parameters *xkvmin*, *xkvmax*, and *xkvsteps* give the velocity range over which to simulate the system and the number of velocity points within

that range. Velocities are expected in units of Γ/k.

The final parameter in a set is the time to allow for system equilibration before evaluating the force. Selecting a proper value for this parameter is a balance between excluding transient behavior and reducing total computation time. After the notebook is evaluated, the time-dependence of each of the elements of the density matrix at the last velocity point of the last parameter set is available. A test case with a long equilibration time can be used to view the time scale of the transient behavior and to select an appropriate equilibration time for larger computations.

A complete parameter set consists of $14 + M_g + M_e + 2M_gM_e + 2M_g^2 + 2M_e^2$ parameters, which in a 12+4 system such as CaF $B \leftrightarrow X$ $P_{11}(1.5)/{}^PQ_{12}(0.5)$ is 446 in total. All but 12 of these remain fixed for a given system. As an example, the input file which produces the $\delta = 30\,\Gamma$ force profile in Fig. 5.4 is:

1
0 12 4 0 0 0 0 0 0.32979 0.32979 0.32979 0.00354 0.00354 0.00354 0 0.33333 0.16667 0.05555 0 0 0.00177 0.00177 0 0.1649 0.1649 0 0.11111 0 0.16667 0.22221 0.16667 0 0.00177 0 0.00177 0.1649 0 0.1649 0.11111 0 0 0.05555 0.16667 0.33333 0 0.00177 0.00177 0 0.1649 0.1649 0.11111 0 0 0 0 7.751 7.751 7.751 7.751 7.751 3.823 3.823 3.823 -15.562 -15.562 -15.562 -3.536 0 0.5 0 -0.5 0.5 0 0.5 0 0 0.5 0 0.5 -0.5 0 0.5 0 0 0 0.5 0 0 -0.5 0 0 0.5 0 0 0 0 0 0 0.5 0 0.3536 0 0 0 0.5338 0 0 -0.3002 0 0 0 0.3536 0 0.433 0 0 0 0.3774 0 0 -0.2123 0 0 0 0.433 0 0.433 0 -0.2179 0 0.2179 0.1225 0 -0.1225 0 0 0 0.433 0 0.3536 0 -0.3774 0 0 0.2123 0 0 0 0 0 0.3536 0 0 0 -0.5338 0 0 0.3002 0 0.5338 0 -0.2179 0 0 0 -0.0698 0 0 0.3204 0 -0.2451 0 0.3774 0 -0.3774 0 -0.0698 0 -0.0698 0.3204 0 0.3204 0 0 0 0.2179 0 -0.5338 0 -0.0698 0 0 0.3204 0 0.2451 -0.3002 0 0.1225 0 0 0 0.3204 0 0 0.3198 0 -0.4358 0 -0.2123 0 0.2123 0 0.3204 0 0.3204 0.3198 0 0.3198 0 0 0 -0.1225 0 0.3002 0 0.3204 0 0 0.3198 0 0.4358 0 0 0 0 0 -0.2451 0 0.2451 -0.4358 0 0.4358 0 -0.5 0 0 0 0 0 0 0 0 0 0 0 0 -0.25 0 0 0 0.3774 0 0 -0.2123 0 0 0 0 0 0 0 0 0 0.4358 0 0 -0.2451 0 0 0 0 0 0.25 0 0 0 0.3774 0 0 -0.2123 0 0 0 0 0 0.5 0 0 0 0 0 0 0 0 0.3774 0 0 0 0.0698 0 0 -0.3204

0 0 0 0 0 0.4358 0 0 0 0 0 0 0 0 -0.2451 0 0 0 0.3774 0 0 0 -0.0698 0 0 0.3204 0 0 -0.2123 0 0 0 -0.3204 0 0 -0.3198 0 0 0 0 0 -0.2451 0 0 0 0 0 0 0 0 -0.4358 0 0 0 -0.2123 0 0 0 0.3204 0 0 0.3198 0 0 0 0 0 0 0 -0.2451 0 0 -0.4358 0 0 12.89 71.43 63.64 30 0 0 0 0 0 0 0.5743 0 0 -0.0595 0 0 0 0.4083 0 0 0 -0.0421 0 0 -0.4061 0 0 0 0 0 0.4714 0 0 0 0 0 0 0 0 0.3333 0 0 0 0.4083 0 0 0 0.0421 0 0 0.4061 0 45 45 -6.088 -40 40 200 100

In this input file, the states within each manifold are arranged in the order presented in Table 5.1. This makes, for example, the first ground state $J = 3/2$, $F = 2$, $M_F = -2$. For γ and *Omegaeg*, which have entries for each combination of ground and excited state, the order of entry is by excited state and then by ground state. As such, γ is entered as γ_{11}, γ_{12}, γ_{13}, etc., as can be seen by the first five elements of γ being zero (cf. Table 5.1).

An input file is selected within the Mathematica notebook as shown in Fig. A.1, and calculation is begun by selecting the "Evaluate Notebook" command. Three dynamic progress bars show the current progress in evaluating the total number of parameter sets, velocity points with a parameter set, and time points within a velocity point.

An output directory is automatically created in the same folder as the input file, containing a copy of the input file and .dat files containing the output for each parameter set. Each of these output files contains the labeled parameters used for the calculation and then a list of triplets for each velocity point: the velocity (in units of Γ/k), the time-averaged force at that velocity (in units of $\hbar k\Gamma/2$), and the time-averaged excited-state fraction at that velocity.

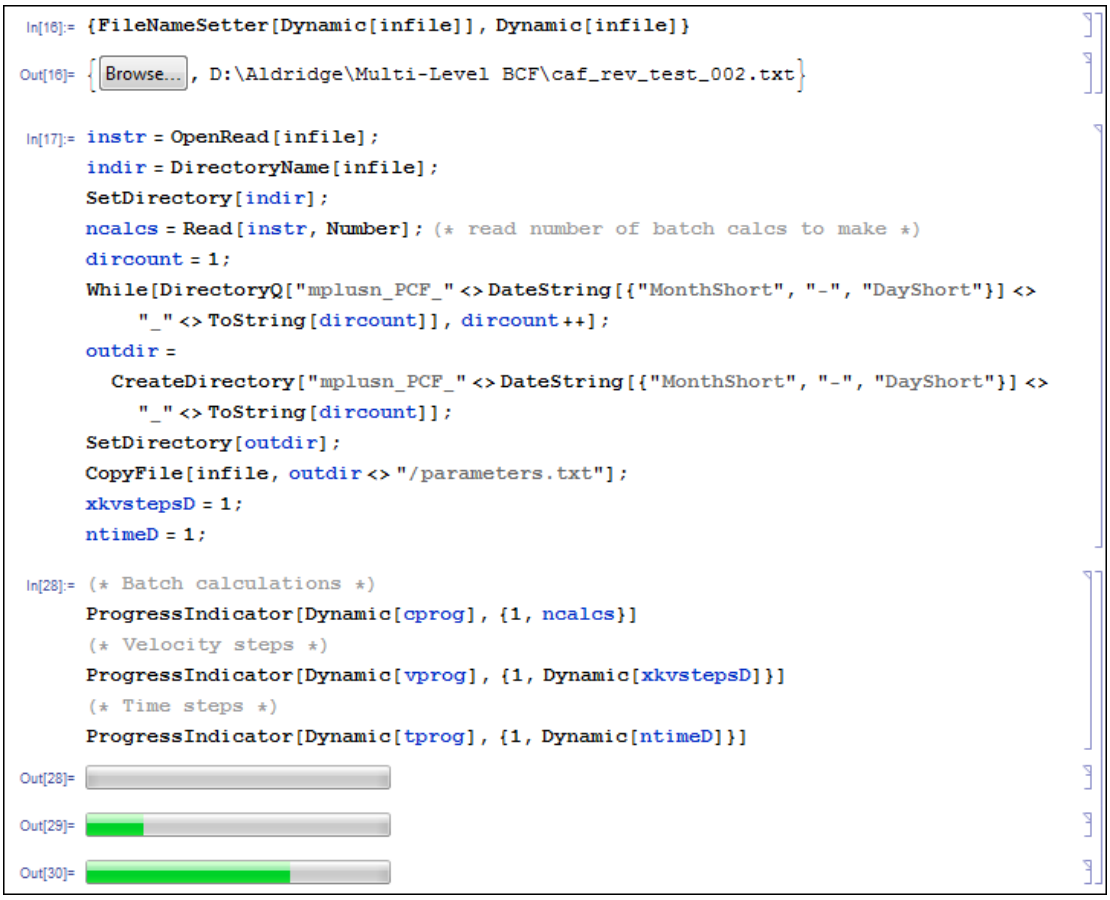

Fig. A.1: A screenshot of the multilevel BCF/PCF simulation Mathematica notebook in mid-evaluation. This portion of the notebook includes the the input file selection at the top, where the "Browse..." button opens a file explorer window to select an input file, and three progress bars at the bottom showing progress through the nested loops of the calculation.

Appendix B

Glossary of Symbols

b	Molecular constant
$\vec{B}$	Magnetic field
B_i	ith spherical tensor component of magnetic field
β	EOM modulation amplitude at frequency δ
c	Speed of light or molecular constant
C	Molecular constant
χ	Electric field phase offset
$\hat{d}$	Electric dipole operator
D	Aperture diameter
δ	Laser detuning, most often the bichromatic detuning of BCF
δ_{ij}	Kronecker delta
$\delta(x)$	Dirac delta function
Δ_{ij}	Single-frequency laser detuning from $\|i\rangle \leftrightarrow \|j\rangle$ transition
$\vec{E}$	Electric field
E_0	Single-beam electric field magnitude
E_{Dirac}	Dirac comb electric field
ϵ_0	Permittivity of free space
F	Total hyperfine angular momentum

F_{ARP}	Adiabatic rapid passage force magnitude
F_{BCF}	Bichromatic force magnitude
F_{rad}	Ideal two-level radiative force magnitude
g_ζ	g-factor of angular momentum ζ
γ	EOM modulation amplitude at frequency 3δ, or a molecular constant
γ_{ip}	Rate of decay from state $\|e_i\rangle$ to state $\|g_p\rangle$
γ_{sc}	Photon scattering rate
Γ_i	Total decay rate from excited state $\|e_i\rangle$
h	Planck's constant
$\hbar$	Reduced Planck's constant
H	Hamiltonian
H_0	Unperturbed Hamiltonian
H_B	Magnetic interaction Hamiltonian
H_{Floq}	Floquet Hamiltonian
i	$\sqrt{-1}$ or summation index
I	Irradiance, or current, or nuclear spin angular momentum
J	Angular momentum
J_k	kth Bessel function of the first kind
k	wavevector, or summation index, or Boltzmann constant
κ_{ij}	Relative dipole matrix element between states $\|i\rangle$ and $\|j\rangle$
ℓ	Bending mode angular momentum quantum number
L	Orbital angular momentum
λ	Wavelength
Λ	Orbital angular momentum projection
m	Mass

$\mathcal{M}$	Mach number
M_e	Excited state multiplicity
M_g	Ground state multiplicity
M_J	Projection of angular momentum J
M_F	Projection of angular momentum F
μ_0	Permeability of free space
μ_B	Bohr magneton
n	Summation index
$n_{\max}$	Series truncation limit for Dirac comb approximation
N	Total number of states, or rotational quantum number
ν	Direct frequency, or triatomic vibrational quantum number
$\mathcal{O}$	Big O, upper bound on the growth rate of a function
ω_i	Characteristic frequency of state $\|i\rangle$
ω_{eg}^L	Frequency of the laser that couples ground and excited manifolds
ω_{ed}^L	Frequency of the laser that couples a distant state and an excited manifold
ω_s	ARP force pulse repetition frequency
Ω	Λ+Σ
Ω_{ij}	Co-rotating Rabi frequency on $\|i\rangle \leftrightarrow \|j\rangle$ transition
Ω_{ij}^R	Rabi frequency on $\|i\rangle \leftrightarrow \|j\rangle$ transition
Ω_{MCR}	Repumping Rabi frequency
Ω^{tot}	Quadrature sum of all Rabi frequencies to a single excited state
Ω_{ij}^0	Rabi frequency amplitude on $\|i\rangle \leftrightarrow \|j\rangle$ transition
P	Laser power
P_e	Average excited state fraction
P_0	Backing pressure

ϕ	J-mixing angle
R	Magnetic coil radius
ρ	Density matrix
$\widetilde{\rho}$	Rotating density matrix
s	Saturation parameter
S	Electron spin angular momentum
Σ	Electron spin angular momentum projection
t	Time
T	Repetition period
T_{BCF}	Average BCF cycling time before loss
T_{MCR}	Average repump cycling time before loss
T_i^j	Spherical tensor
T_p	Translational temperature
T_0	Initial tempterature
θ_{BE}	Magnetic field skew angle
u	Bloch vector component
v	Velocity, or Bloch vector component, or vibrational quantum number
v_0	Effective zero velocity
w	Laser spot diameter or Bloch vector component
ζ	Summation stand-in for L or S

Bibliography

[1] D. Wineland and H. Dehmelt, Bull. Am. Phys. Soc. **20**, 637 (1975).

[2] D. Wineland and W. Itano, Phys. Rev. A **20**, 1521 (1979).

[3] T. Hänsch and A. Schawlow, Opt. Comm. **13**, 68 (1975).

[4] E. L. Raab, M. Prentiss, A. Cable, S. Chu, and D. E. Pritchard, Phys. Rev. Lett. **59**, 2631 (1987).

[5] J. Brown and A. Carrington, *Rotational Spectroscopy of Diatomic Molecules*, (Cambridge University Press, New York, 2003).

[6] M. Yeo, M.T. Hummon, A.L. Collopy, B. Yan, B. Hemmerling, E. Chae, J.M. Doyle, and J. Ye, Phys. Rev. Lett. **114**, 223003 (2015).

[7] V. Zhelyazkova, A. Cournol, T.E. Wall, A. Matsushima, J.J. Hudson, E.A. Hinds, M.R. Tarbutt, and B.E. Sauer, Phys. Rev. A **89**, 053416 (2014).

[8] B. Hemmerling, E. Chae, A. Ravi, L. Anderegg, N. Hutzler, G. Drayna, A. Collopy, J. Ye, W. Ketterle, and J. M. Doyle, arXiv:1603.02787 (2016).

[9] E. S. Shuman, J. F. Barry, D. R. Glenn, and D. DeMille, Phys. Rev. Lett. **103** 223001 (2009); also E. S. Shuman, J. F. Barry, and D. DeMille, Nature **467**, 820 (2010).

[10] J. F. Barry, E. S. Shuman, E. B. Norrgard and D. DeMille, Phys. Rev. Lett. **108**, 103002 (2012).

[11] M. T. Hummon, M. Yeo, B. K. Stuhl, A. L. Collopy, Y. Xia, and J. Ye, Phys. Rev. Lett. **110**, 143001 (2013).

[12] J. F. Barry, E. S. Shuman, and D. DeMille, Phys. Chem. Chem. Phys. **13**, 18936 (2011).

[13] J. F. Barry, D. J. McCarron, E. B. Norrgard, M. H. Steinecker, and D. DeMille, Nature 512, 286 (2014).

[14] D. J. McCarron, E. B. Norrgard, M. H. Steinecker, and D. DeMille, New J. Phys. **17**, 035014 (2015).

[15] M. A. Chieda, Ph.D. thesis, University of Connecticut, 2012.

[16] H. J. Metcalf and P. van der Straten, *Laser Cooling and Trapping*, Springer-Verlag, New York, 1999.

[17] W. Ertmer, R. Blatt, J. L. Hall, and M. Zhu, Phys. Rev. Lett. **54**, 996 (1985).

[18] R. N. Watts and C. E. Wieman, Opt. Lett. **11**, 291 (1986).

[19] B. Sheehy, S.-Q. Shang, R. Watts, S. Hatamian, and H. Metcalf, J. Opt. Soc. Am. B **6**, 2165 (1989).

[20] R. Schumann, C. Schubert, U. Eichmann, R. Jung, and G. von Oppen, Phys. Rev. A **59**, 2120 (1999).

[21] W. D. Phillips and H. Metcalf, Phys. Rev. Lett. **48**, 596 (1982).

[22] T. Lu, X. Miao, and H. Metcalf, Phys. Rev. A **71**, 061405(R) (2005).

[23] D. Stack, J. Elgin, P. M. Anisimov, and H. Metcalf, Phys. Rev. A **84**, 013420 (2011).

[24] X. Miao, E. Wertz, M. G. Cohen, and H. Metcalf, Phys. Rev. A **75**, 011402(R) (2007).

[25] A. P. Kazantsev and I. V. Krasnov, JETP Lett. **46**, 420 (1987).

[26] J. Javanainen, Phys. Rev. Lett. **64**, 519 (1990).

[27] T. T. Grove, B. C. Duncan, V. Sanchez-Villicana, and P. L. Gould, Phys. Rev. A **51**, R4325 (1995).

[28] J. Söding, R. Grimm, Yu. B. Ovchinnikov, Ph. Bouyer, and Ch. Salomon, Phys. Rev. Lett. **78**, 1420 (1997).

[29] V.S. Voitsekhovich, M. V. Danileiko, A. M. Negriiko, V. I. Romanenko, and L. P. Yatsenko, JETP Lett. **49**, 161 (1988).

[30] P. W. Milonni and J. H. Eberly, *Lasers*, John Wiley & Sons, New York, 1988.

[31] L. Yatsenko and H. Metcalf, Phys. Rev. A **70**, 063402 (2004).

[32] L. D. Landau, Phys. Z. Sowjetunion **2**, 46 (1932).

[33] C. Zener, Proc. R. Soc. A **137**, 696 (1932).

[34] H.-P. Breuer and F. Pertuccione, *The Theory of Open Quantum Systems*, Oxford University Press, Oxford, 2002.

[35] P. Ehrenfest, Z. Phys. **45**, 455 (1927).

[36] T. H. Einwohner, J. Wong and J. C. Garrison, Phys. Rev. A **14**, 1452 (1976).

[37] G. T. Purves, Ph.D. thesis, Durham University, 2006.

[38] M. R. Williams, F. Chi, M. T. Cashen, and H. Metcalf, Phys. Rev. A **60**, R1763 (1999).

[39] M. R. Williams, F. Chi, M. T. Cashen, and H. Metcalf, Phys. Rev. A **61**, 023408 (2000).

[40] T. C. Liebisch, E. Blanshan, E. A. Donley, and J. Kitching, Phys. Rev. A **85**, 013407 (2012).

[41] M. T. Cashen and H. Metcalf, Phys. Rev. A **63**, 025406 (2001).

[42] M. Cashen and H. Metcalf, J. Opt. Soc. Am. B **20**, 915 (2003).

[43] M. Partlow, X. Miao, J. Bochmann, M. Cashen, and H. Metcalf, Phys. Rev. Lett. **93**, 213004 (2004).

[44] M. A. Chieda and E. E. Eyler, Phys. Rev. A **86**, 053415 (2012).

[45] C. Corder, B. Arnold, and H. Metcalf, Phys. Rev. Lett. **114**, 043002 (2015).

[46] S. E. Galica, L. Aldridge, and E. E. Eyler, Phys. Rev. A **88**, 043418 (2013).

[47] A. Yariv, *Optical Electronics, Fourth Edition*, (Saunders College Publishing, Philadelphia, 1991).

[48] G.B. Arfken and H. J. Weber, *Mathematical Methods for Physicists*, (Elsevier Academic Press, Burlington, 2005).

[49] L. Aldridge, S .E. Galica, and E. E. Eyler, Phys. Rev. A **93**, 013419 (2016).

[50] S. Sen, T. K. Dey, M. R. Nath, and G. Gangopadhyah, J. Mod. Opt. **62**, 166 (2015).

[51] D. J. Berkeland and M. G. Boshier, Phys. Rev. A **65**, 033413 (2002).

[52] H. Lu, I. Kozyryev, B. Hemmerling, J. Piskorski, and J. M. Doyle, Phys. Rev. Lett. **112**, 113006 (2014).

[53] M. Dulick, P. F. Bernath, and R. W. Field, Can. J. Phys. **58**, 703 (1980).

[54] K. P. Huber and G. Herzberg, *Constants of Diatomic Molecules*, (Van Nostrand, New York, 1979).

[55] G. Herzberg and J. W. T. Spinks, *Molecular Spectra and Molecular Structure*, (Van Nostrand, Princeton, 1950), 2nd Ed., Vol. 2.

[56] S. F. Rice, H. Martin, and R. W. Field, J. Chem. Phys. **82**, 5023 (1985).

[57] W. J. Childs, G. L. Goodman, and L. S. Goodman, J. Mol. Spectrosc. **86**, 365 (1981).

[58] T. E. Wall, J. F. Kanem, J. J. Hudson, B. E. Sauer, D. Cho, M. G. Boshier, E. A. Hinds, and M. R. Tarbutt, Phys. Rev. A. **78**, 062509 (2008).

[59] P. J. Dagdigian, H. W. Cruse, and R. N. Zare, J. Chem. Phys. **60**, 2330 (1973).

[60] M. A. Chieda and E. E. Eyler, Phys. Rev. A **84**, 063401 (2011).

[61] I. Kozyryev, L. Baum, K. Matsuda, P. Olson, B. Hemmerling, and J. M. Doyle, New J. Phys. **17**, 045003 (2015).

[62] I. Kozyryev, L. Baum, K. Matsuda, B. Hemmerling, and J. M. Doyle, J. Phys. B: At. Mol. Opt. Phys. **49**, 134002 (2016).

[63] J. Nakagawa, R. F. Wormsbecher, and D. O. Harris, J. Mol. Spec. **97**, 37 (1983).

[64] T. Sharp and H. Rosenstock, J. Chem. Phys. **41**, 3453 (1964).

[65] I. Kozyryev, personal communication, January 26, 2016.

[66] J. F. Barry, Ph.D. thesis, Yale University, 2013.

[67] D. A. Fletcher, K. Y. Jung, C. T. Scurlock, and T. C. Steimle, J. Chem. Phys. **98**, 1837 (1993).

[68] B. E. Sauer, J. Wang, and E. A. Hinds, J. Chem. Phys. **105**, 7412 (1996).

[69] C. R. Brazier, P. F. Bernath, J. Mol. Spectrosc. **114**, 163 (1985).

[70] T. A. Miller, Science **223**, 545 (1984).

[71] D. M. Lubman, C. T. Rettner, and R. N. Zare, J. Chem. Phys. **86**, 1129 (1982).

[72] Y. Zhou, Ph.D. thesis, Massacusetts Institute of Technology, 2014.

[73] M. R. Tarbutt, J. J. Hudson, B. E. Sauer, E. A. Hinds, V. A. Ryzhov, V. L. Ryabov, and V. G. Ezhov, J. Phys. B: At. Mol. Opt. Phys. **35**, 5013 (2002).

[74] R. Campargue, J. Chem. Phys. **88**, 4466 (1984).

[75] R. W. Field, D. O. Harris, and T. Tanaka, J. Mol. Spectrosc. **57**, 107 (1975).

[76] J. Nakagawa, P. J. Domalle, T. C. Steimle, and D. O. Harris, J. Mol. Spec. **70**, 374 (1978).

[77] D. DeMille, J. F. Barry, E. R. Edwards, E. B. Norrgard, and M. H. Steinecker, Mol. Phys. **111**, 1805 (2013).

[78] D. DeMille, Phys. Rev. Lett. **88**, 067901 (2002).

[79] A. C. Vutha, W. C. Campbell, Y. V. Gurevich, N. R. Hutzler, M. Parsons, D. Patterson, E. Petrik, B. Spaun, J. M. Doyle, G. Gabrielse, and D. DeMille, J. Phys. B: At. Mol. Opt. Phys. **43**, 074007 (2010).

[80] J. Baron, W. C. Campbell, D. DeMille, J. M. Doyle, G. Gabrielse, Y. V. Gurevich, P. W. Hess, N. R. Hutzler, E. Kirilov, I. Kozyryev, B. R. O'Leary, C. D. Panda, M. F. Parsons, E. S. Petrik, B. Spaun, A. C. Vutha, and A. D. West, Science **343**, 269 (2014).

[81] E. Reinhold and W. Ubachs, Mol. Phys. **103**, 1329 (2005).

[82] R. Grimm, Y. B. Ovchinnikov, A. I. Sidorov, and V. S. Letokhov, Phys. Rev. Lett. **65**, 1415 (1990).

[83] *AtomicDensityMatrix*, http://rochesterscientific.com/ADM/, Rochester Scientific (retrieved Sep. 8, 2016). See also M. Auzinsh, D. Budker, and S. Rochester, *Optically Polarized Atoms*, (Oxford University Press, Oxford, 2010), Appendix E.